Additive Manufacturing of Copper Electrodes and Bus Work for Resistance Welding

By

Brooke Renee Dyer

Submitted in Partial Fulfillment of the Requirements for the Degree of

Master of Science

in the

Mechanical Engineering Program

Youngstown State University

May 2017

Additive Manufacturing of Electrodes and Bus Work for Resistance Welding

Brooke Renee Dyer

I hereby release this thesis to the public. I understand that this thesis will be made available from the OhioLINK ETD Center and the Maag Library Circulation Desk for public access. I also authorize the University or other individuals to make copies of this thesis as needed for scholarly research.

Signature: _____

Brooke Renee Dyer, Student   Date

Approvals: _____

Dr. C. Virgil Solomon, Thesis Advisor   Date

_____

Dr. Hazel Marie, Committee Member   Date

_____

Dr. Jae Joong Ryu, Committee Member   Date

_____

Dr. Salvatore A. Sanders, Dean of Graduate Studies   Date

Abstract

Additive manufacturing is opening new opportunities to produce parts in many industries. This thesis explores the Additive Manufacturing (AM) of copper parts with a Renishaw 250AM for resistance welding machines. The Renishaw 250AM uses a 200W ytterbium fiber laser to create Selective Laser Melting (SLM) parts. AcuPowder 150A was selected out of three copper powders. A series of prints were completed and optimal parameters were chosen. AM copper tensile samples at different orientations and laser exposure times were created to test mechanical properties. Sintered SLM copper samples were also tested and were discovered to be stronger and more dense than non-sintered SLM parts. Electrode and electrode adapters for INV-.5 resistance spot welders were printed and the machining process was recorded. Six weld test groups were obtained by using a combination of conventional and AM electrodes and electrodes adapters were completed and weld schedules were developed. The mechanical properties of the welds were investigated with shear tensile tests and U tensile tests. Groups 1 and 2 were control groups with conventionally made secondary circuits with C110 and RWMA Class 2 electrodes. Groups 3 and 4 contained mixed AM and conventional part systems. Groups 5 and 6 were fully printed systems. Group 6 contained sintered electrodes. The ultimate weld force, current density, and electrode wear were recorded. Depending on the type of pull test, the mixed system welds corresponded within 5-7% of groups 1 and 2. The fully printed systems had more inconsistences due to the increase in electrical resistance based on the porosity and surface roughness of the SLM parts.

The numerical modeling of the heat transfer in a typical resistance spot welder electrode/ electrode adapter cooling water system was investigated using Solidworks Flow

Simulation. Two models using different internal geometries were compared to maximize the cooling rate of the electrode. The determined results showed that an internal 1 mm cooling pipe height had a greater cooling rate than a 3 mm cooling pipe height.

Acknowledgements

My deepest and most sincere gratitude goes to the following people who have made this thesis possible.

Thesis Advisor

Dr. C. Virgil Solomon

Committee Members

Dr. Hazel Marie

Dr. Jae Joong Ryu

Thesis Sponsor

Taylor Winfield Technologies

Additional Assistance

Taylor Winfield Faculty

American Makes Faculty

Dr. Stefan Moldovan

Students

Rodrigo Enriquez

Chris Barret

Michael Juhasz

Matt Caputo

Special Thanks

To my husband and my parents, for always supporting me in all my endeavors, and for encouraging me to apply and complete my Master's degree.

To my grandparents, for always believing in me.

Table of Contents

Table of Figures

List of Tables

Nomenclature

Variable	Description	Units
VED	Volumetric energy density	kJ*mm^{-3}
P	Laser power	kW
v	Laser scan speed	Mm/s
h	Scan row spacing	mm
d	Layer thickness	mm
H	Heat generated	Watts
I	Current	Amps
R	Electrical resistance	ohms
c_r	Cooling rate	~
T_{max}	Maximum temperature of the electrode	K
T_i	Initial temperature of the electrode	K
A_x	Cross-sectional area of pipe at position "x"	mm^2
V_x	Flow velocity at position "x"	m/s
ρ	Density of fluid	Kg/m^3
RWMA	Resistance Welding Machine Association	
SFS	Solidworks Simulation Flow	
INV-1/2	Taylor Winfield Resistance Welder	
XEDS	X-Ray Energy Dispersive Spectroscopy	
AM	Additive Manufacturing	
SEM	Scanning Electron Microscope	
SLM	Selective Laser Melting	

1.0 Introduction

Additive manufacturing (AM) is a branch of technologies that builds parts from three dimensional models by adding material one layer at a time. Over the past thirty years, additive manufacturing has dramatically changed the processes of manufacturing components. This branch of mechanical engineering can create parts on demand without using the typical standard wastes that are found in the industry. Such wastes include cutting fluid, cutting tools, tooling jigs, and coolants. Additive manufacturing creates parts with minimal material waste and has recently started creating finished products for the industry. At the time of this writing, additive manufacturing is advancing from plastics to various metals. Due to this evolution, additive manufactured parts are now created with similar material properties when compared with their conventionally manufactured parts.[1]

In an expanding commercial market, industrial companies seek to produce higher quality machines at a faster rate of time than their competitors. Components of the equipment need to be readily available to assemble a fully functioning machine and still meet the customer's deadlines. Some companies have the benefit of possessing an inventory of spare parts for all existing machines if machine production ceases due to a damaged component. However, due to Lean Manufacturing, many companies are straying from the conventional methods of keeping inventory on-hand. For companies that manufacture many different types of equipment, it is impractical to have spare parts in stock to accommodate for every machine and customer need. This type of system works well for economic reasons, but leaves the manufacturer and customer at a disadvantage when spare parts are needed in a narrow window of time. For many manufacturers in the

steel industry, time is money and every day that a machine is out of production is a day of unrecoverable revenues. To fulfill this demand, the manufacturer may need to expedite or seek a different vendor to meet the needs of the customer. This can be a disadvantage to the manufacturer and the customer. By utilizing additive manufacturing, the manufacturer has the potential to produce the part at a fraction of the price in significantly less time than conventional methods. It is essential for companies to be able to study new technologies to aid in the machine build efficiencies to stay competitive.
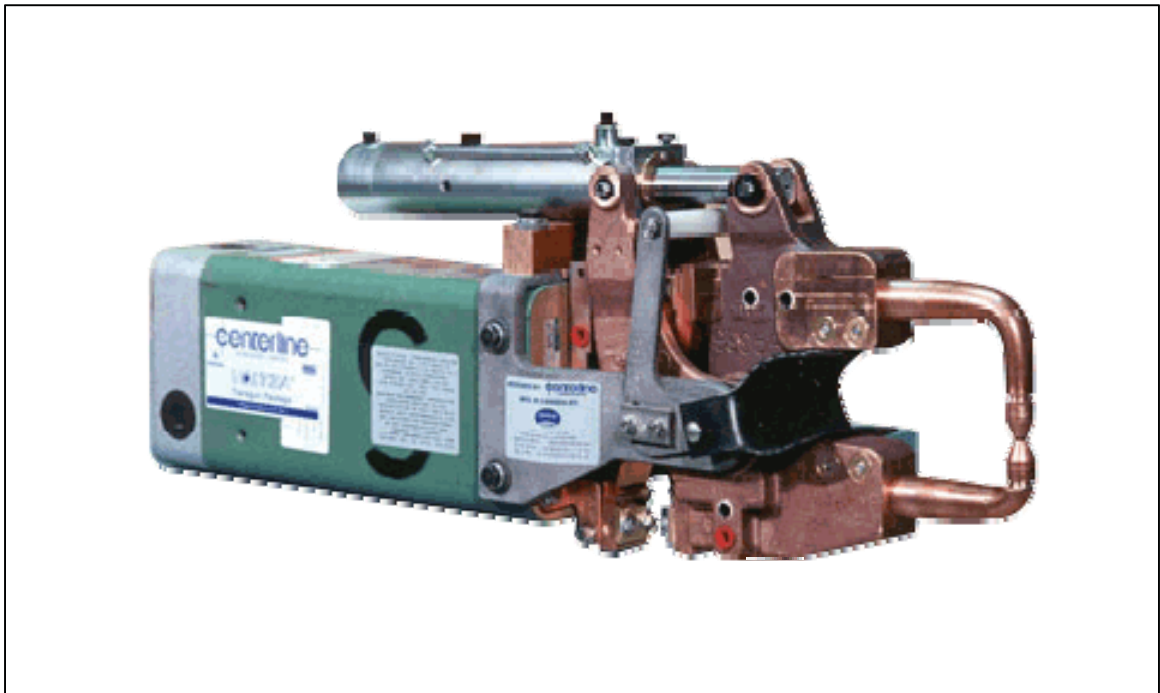
Figure 1: Transgun with Cast Copper Arms[2]

Transguns are unique pieces of portable resistance welding equipment that are used in the automotive industry to make welded joints around a car frame. Each transgun is custom designed for the series of welds it performs. Many of these components are made from casts, as shown in Figure 1. The copper components of a transgun usually need internal water paths to make acceptable weld joints and to increase the production life of the equipment. Obtaining cast copper products is a constraint in the resistance welding

industry because molds must be created for a part to be cast. If water cooling is necessary for the application, the water paths must be created by adding features to the cast mold or by adding machining processes after the cast is complete. Water paths can also be added by a tube brazing process after the cast is made. Also, to efficiently conduct electricity through the copper cast parts, the component must go through a machining process to refine the surface finishes to reduce electric flow resistance.

In this thesis, additive manufacturing will be utilized to create copper components for the resistance welding industry.

1.1 Taylor-Winfield Technologies & Resistance Welding

Taylor-Winfield Technologies is an industrial equipment manufacturer of resistance welding machines, induction heating power supplies, material handling, and automation solutions. Since the company's establishment, it has produced machines for the milling, automotive, aerospace, mining, pharmaceutical, and appliance industries. Taylor-Winfield is one of the original resistance welding machine manufacturers. Many of the resistance welding standards have been established by its employees or derived from its research laboratory.

Resistance welding is a process that joins metallic parts together through the heat generated from the electrical resistance of current flow. The basic resistance welding circuit consists of a transformer, bus work, electrodes, and the work pieces, as shown in Figure 2. The workpieces are the metallic components to be welded. The transformer converts the incoming standard high voltage low current electrical input to a low voltage, high current input. The bus work is the copper circuit that the electrical current flows

through after it leaves the transformer. The electrodes are part of the copper circuit that contacts the workpieces, this completes the electrical circuit. There are at least two electrodes that contact the workpieces, connecting both sides of the weld circuit.
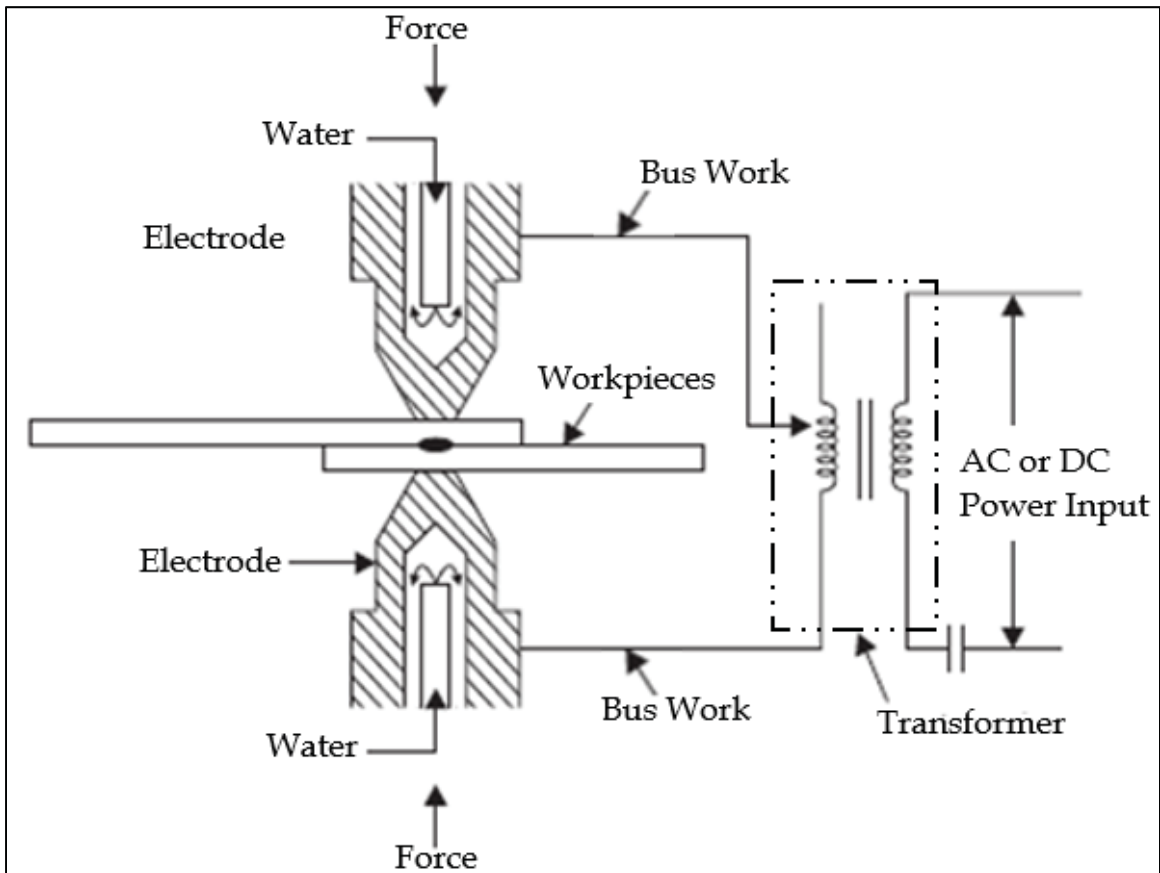
Figure 2: Basic Resistance Welding Circuit[3]

A simple example of the resistance welding process can be explained as follows: The workpieces are placed into the joining position. The upper and lower electrodes contact the workpieces and apply a force to the workpieces. An electrical current is then passed through the circuit. In a properly insulated and designed resistance welding circuit, the workpiece interface causes the most resistance in the circuit as the current passes through the parts. This resistance causes energy loss in the form of heat. Due to the high electrical current, the heat at the weld zone is generated so rapidly that only a minimal amount of heat is dissipated through conduction to the surrounding materials. With the

4

correct amount of current, time, and part clamp force, the heat generated will melt the part material at the interface and will form a weld nugget between the parts. Unlike other welding techniques, resistance welding uses a mechanical force to forge the workpieces together. The application of the forging force refines the grain structure of the joined workpieces and gives the welded area mechanical properties equal to if not superior than the parent material. Parent material is the term used to describe the material of the workpieces around the weld that are not affected by the weld process.

Resistance welding is known as the most widely used joining technique for sheet metal components. It is also known to be the most economical. This form of welding does not complicate the metallurgy of the metal by adding extraneous materials, such as filler rods and fluxes to form the weld. Most individual welds take only a few fractions of a second to complete. Resistance welding is a high-speed operation and can be facilitated using automation and robots.

To reduce the electrical resistance in the weld circuit further away from the workpieces, a large amount of copper is used in the bus work. Although copper is very conductive, there is still heat generated from electrical resistance. The electrodes experience both the bulk material's electrical resistance heat and the heat transferred to it through conduction from the workpieces. If the electrodes become hot enough, the electrode-to-workpiece contact surface will deform and cause a change in electrical current distribution. The change in electrical current distribution can cause a decrease in the heat created at the workpiece's interface. Less created heat could produce a small weld nugget or no weld nugget at all, resulting in a bad weld. Therefore, keeping the electrode's proper geometry

is crucial to producing acceptable welds. To prevent the damaging heat, the bus work

and the electrodes have water cooling pathways.[3]

In a manufacturing aspect, adding water cooling circuits into the bus work and electrodes

complicates the geometry of the parts. Water pathways can be added through machining

processes, brazing water tubes into the parts, or by adding water tubes into castings.

Each process has different advantages and disadvantages depending on the application.

The addition of water paths add cost to creating a functional part by the additional

processes, further material, and the time to get the finished parts.

1.2 Metal Additive Manufacturing Technologies

1.2.1 Metal Additive Manufacturing Technologies Overview

Metal additive manufacturing is the process of adding raw material, usually in powder

form, layer by layer to produce the parts desired. The process is controlled by a computer

and typically utilizes a binder glue or a laser as a material consolidator. This thesis will

focus on the laser additive manufacturing machines. A computer aided design is created

and loaded into a slicer program. The slicer program mathematically slices the model

into parameterized layers based on the raw material specifications, as shown in Figure 3.

The computer controlled laser will bond the layers of the raw material into the desired

object. Additive manufacturing can produce parts with complex geometries that

conventional machines cannot duplicate[4] or can only manufacture at a very high cost.
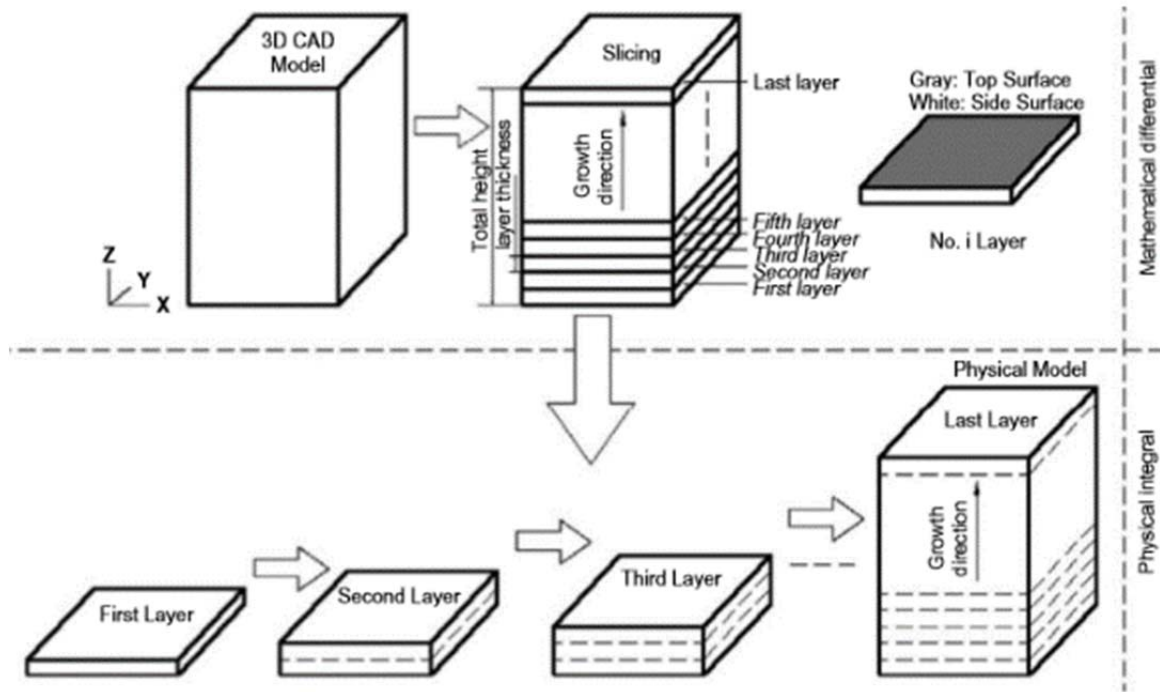
Figure 3: Additive Manufacturing Mathematical Differential to Physical Integral[5]

Although considered versatile, the additive manufacturing of metals is a complex process. The mechanical properties of the object created, such as hardness, modulus of elasticity, density, and residual stress, are strongly dependent on the properties of the raw material and the process parameters selected for the build, such as laser power, speed and spot size, layer thickness, and scan line spacing. Three of the most versatile processes of metal additive manufacturing are laser sintering, laser melting, and laser metal deposition.[4]

1.2.2 Laser Sintering

Laser sintering is an additive manufacturing process used for single component powder, pre-alloyed metal powders and multicomponent metal powders. The multicomponent powder usually consists of a high melting point metal powder used as a structural component and a low melting point powder used as a binder. Small amounts of powder additives such as fluxing agents and deoxidizers can be added to optimize the post

process part. A laser sintering apparatus consists of a computer to control the automated processes, an automated powder layering component, and an automated laser. Most laser sintering machines have inert gas building chambers to reduce the oxygen during the laser sintering process. Most machines also contain powder bed heaters to prevent warping and delamination and to lower the temperature heat gradient during the sintering process. A substrate is attached to a leveled and fixed building platform. The layering apparatus spreads an even layer of powder no larger than 100 μm thick onto the substrate. The laser then scans the layer profile of the part provided by the mathematically computed slice from the slicer software. The laser cycle is usually between .5 to 25 ms. During the cycle, the binder powder melts completely and rearranges around the still solid structural powder from the capillary and wetting effect. The layer will structurally rearrange itself and then solidify. CO_2, neodymium-doped yttrium aluminum garnet, fiber, and disc lasers can be used in laser sintering. The type of laser is chosen by powder properties and the desired properties of the post process part. The laser wavelength determines laser absorptivity. The input laser energy density determines the powder densification. Common anomalies of the laser sintering process are insufficient densification, incomplete material rearrangement, and heterogeneous microstructures. Each of these anomalies negatively affects the mechanical properties of the part. These anomalies make post-processes necessary to optimize the part's properties. A few processes used are furnace heat treatment and secondary infiltration.[4]

1.2.3 Laser Melting

Laser melting is a similar process in comparison to laser sintering in both processes and apparatuses. The only difference is the complete melting of the powder layer and higher

energy laser input. With the complete melting and solidification of the powder layer, the density of the part can be increased to 99.5% of the parent material without any post treatment. The mechanical properties of laser melted parts are also closer to the parent material than laser sintered parts. Fully melting the powder layer also allows pure metals, including nonferrous metals, to be processed. Laser melting of metals utilizes thinner layers of powder and higher laser energy than laser sintering. The thin layers of powder require a longer duration of build time. The laser melting process also has its inherent problems. A fully melted layer pool increases the instability of the shape and increases the shrinkage and residual stresses during the solidification process. The residual stresses and shrinking can cause delamination and distortion of the processed part.[4]

1.2.4 Laser Metal Deposition

Laser metal deposition directly feeds metal powder to a nozzle that is attached to the laser. The powder is only placed where needed and melted in place. Like laser melting, this system also works in thin layers. This method of metal additive manufacturing allows more complex parts to be created with more dimensional accuracy. Laser metal deposition can also be used to rebuild worn or damaged components and to add wear and corrosion resistant coatings. Multiple materials can be deposited in a single part as it is created. The most critical parameter in laser metal deposition is the size of the melt pool. Like laser melting additive manufacturing, residual stresses created during the process are an obstacle encountered when creating a production part.[4]

1.2.5 Additive Manufacturing Process and Material-Laser Beam Interaction

The radiation energy of the laser beam directly contacts the powder. Some of the energy is absorbed, while the rest of the energy is reflected. Powder absorptance is the ratio

between absorbed radiation by the powder and total (or incident) radiation exposed to the powder. Absorptance determines the acceptable laser energy operating range and it is time and process dependent. Materials with large absorptance need less laser energy to create an acceptance melt pool. In powders, the optical penetration of radiation is larger than the bulk material. Absorptance decreases as the laser beam wavelength increases for metals and carbides. The absorptance of oxides increases as the wavelength increases. Absorptance can change while being exposed to the laser beam energy, through particle rearrangement, and phase change. Another change to absorption is oxidation melt. Powders with oxide coatings need a larger wavelength to melt the oxide layer. The same laser wavelength used to melt the oxide may decrease the absorptance of the pure metal underneath causing only a partial melt of the powder particles.[4]

Wettability and viscosity are melt pool characteristics that aid in the determination of the strength of the solid-state bond between layers. Wettability is a liquid's tendency to spread and adhere to a solid surface. This is necessary for the layers of the melt pool to bond to previous cooling layers. Oxide coatings on the powder particles and melt pool significantly decrease the wettability of the melt pool and cause defects in the part such as delamination of the layers and balling. Balling is the formation of spherical inclusions as the melt pool cools to reduce the free energy at the melt pool surface.[6] Oxidation of the melt pool is decreased by filling the build chamber with high purity inert gas and adding flux agents into the powder mix. The best practices state that using "clean", or oxide free powders significantly reduce the problems caused from reduced wettability.

Viscosity is a liquid's resistance to flow. During the additive manufacturing process the viscosity should be high enough to prevent the defect of balling and low enough to allow

the melt pool to spread across the lower layer of the part before cooling and solidifying. Increasing the working temperature of the powder will decrease the viscosity of the melt pool. Power bed heaters and preheating scans of the laser are used to increase the viscosity of the melt pool.[4]

1.2.6 Additive Manufactured Part Properties

The balling effect is an inherit issue when processing metals in a loose powder bed. The laser moves in overlapping rows when processing layers. As the laser passes over the loose powder bed, a cylindrical melt pool is formed. As it cools, the row breaks and forms sphere-like shapes. Depending on the time lapse, interlocking rows may form weak to no bond between rows of the same process layer. Shrinkage of the melt pool due to high laser scanning speeds causes "shrinkage induced balling". High laser power and low laser scan speeds will cause "splash balling". Processing parts on a cold powder bed will lead to "initial scan line balling".[4] Balling causes the part to have a heterogeneous composition. This means that layers of a part delaminate from each other and voids increase in the part. To reduce the effect of balling, ramp up and ramp down of laser energy is suggested. Ramping up preheats the powder. The peak of the laser power will transform the powder into a melt pool. The ramp down decreases the viscosity of the melt pool and prolongs the liquid state. This causes the newly created melt pool to flow and create stronger bonds before solidifying. This laser power function also decreases surface roughness.

The grain of the microstructure is unrefined due to the rapid formation and solidification of the melt pool. The grain develops and grows in the direction of the maximum temperature of the melt pool. The grain size in an additive manufactured part varies from

11

layer to layer. The bottom layer grains are smaller than top layer grains. Heat quickly leaves the melt pool of the first layer due to the cool powder bed's conduction. The heat accumulation in the powder bed and previous processed layers allows the consequent layers of the part more time for grain growth during solidification. Further, the scanning laser will reheat and possibly re-liquefy the previous layers resulting in continued grain growth.

A fundamental additive manufactured part property is densification level. Densification determines the mechanical properties. Densification is mainly dependent on the laser energy density and the laser scan rate. The depth of the layer and scan row spacing also affect the densification of the part. Higher density in a part is created by increasing the laser's energy density. Too much laser energy density causes cracks and voids to form due to the low viscosity of the melt pool (balling) and increases in residual stresses. To establish the optimum densification parameters, the volumetric energy density (*VED*) must be defined.[4]

$$VED = \frac{P}{vhd} \tag{1-1}$$

Where P is laser power, v is scan speed, h is hatch spacing, and d is layer thickness. Additive manufactured parts fundamentally contain residual stresses. The top and bottom of the processed part have tension residual stresses while the middle contains compressive residual stresses. Residual stresses are caused by additive manufacturing parameters, part material, and the geometric height of the part. Residual stresses are sometimes created due to the rapid melting and solidification of the melt pool. The residual stress of rapid cooling can cause stress cracks and delamination between the part

layers. These cracks and delaminations severely reduce the strength, ductility, and dimensional accuracy of the processed part. Preheating the substrate and powder bed reduces the temperature gradient which reduces the residual stresses. Residual stresses are greater in the perpendicular direction of the laser scan line.   It is recommended to use shorter raster lines to reduce the residual stress induced by laser scanning. Materials with smaller thermal expansion rates tend to have lower values of residual stress.[4]

The hardness and wear performance of additive manufactured parts are dependent on the densification of the processed part. A high-density part with minimal residual stresses and anomalies has a hardness that surpasses the hardness of a conventionally made part. The wear properties of additive manufactured parts are also comparable to the conventionally made parts.[4]

1.2.7 Pure Metal Additive Manufacturing

The process of additive manufacturing on pure metals has proven difficult. Pure metals are naturally weak compared to metal alloys. Pure metals have limited mechanical properties. The limited mechanical properties reduce the additive manufacturing machine's ability to produce acceptable parts. Any slight change in machine parameters can greatly affect the additive manufactured part properties.   Pure metals are predominately susceptible to oxidation and corrosion.[4] Oxidation and corrosion of pure metals can cause little to no pool melting due to the increase of the melting point temperature of the unwanted powder coating.

1.3 Additive Manufacturing of Copper & Copper Alloys

This section presents a science and engineering literature review for the additive manufacturing of copper and copper alloys experiments and development. Copper is a

unique material to be used in additive manufacturing. Copper has excellent thermal conductivity and electrical conductivity, and is relatively inexpensive. These characteristics place copper in high demand for many markets and applications.[7] Physical properties of the copper are presented in Table 1.

Table 1: Properties of Copper[8]

	Metric Units
Melting Point	1083° C
Density	$8.94 \frac{g}{cm^3}$ @ 20°C
Coef. Thermal Expansion	17.0 x 10^6/C (20-100°C)
Thermal Conductivity	$385 \frac{w}{mK}$ @ 20°C
Electrical Resistivity	1.71 μΩ*cm @ 20°C
Electrical Conductivity	0.586 μΩ -cm @ 20°C
Specific Heat	$.385 \frac{J}{gK}$
Modulus of Elasticity (Tension)	117,000 MPa
Modulus of Rigidity	44,000 MPa

Zhu et al^9 reported that the direct laser sintering of copper has fixed material and environment conditions. The process parameters of laser scan speed, laser power, scan spacing, layer thickness, and pre-heating temperature determine the microstructure of the processed part by controlling the temperature distribution, heat flow, and cooling rate of the powder bed. In their experiment, Zhu et al^9 used a 60:40 ratio of 99% dendrite copper powder averaging 40μm, to SCuP binder powder that ranged between 5 to 20μm. They utilized a 10.6μm, 100W, continuous wave CO_2 laser with varying scan speeds and scan spacing. Their results indicated that a decrease in scan speeds and scan spacing led to denser parts.

Tang et al^{10} utilized a 200W, continuous wave CO_2 laser to experiment with loose powder's density effect on the process part's density, optimized parameters of laser

14

power, scan speed, and scan spacing for high density sintered parts. It was observed that a higher loose powder density produced a higher density on the processed parts. Dimensional accuracy increases with decreased laser power, and increased scan speed and spacing. Layer thickness has no effect on dimensional accuracy. Final density increases with increased laser power and decreased scan speed and spacing. Surface roughness decreases with increased laser power and decrease in scan spacing. Tensile strength increases with increased laser powder, layer thickness, and scan speed, and decreased scan spacing. These findings are shown in Table 2.

Table 2: Tang et al Printing Parameters Optimization[10]

Optimized Parameters	Variable Parameters			
	Laser Power	Scan Speed	Scan Spacing	Layer Thickness
Increasing Dimensional Accuracy	Decrease	Increase	Decrease	No Influence
Increasing Final Density	Increase	Decrease	Increase	N/A
Decreasing Surface Finish	Increase	N/A	Decrease	N/A
Increasing Tensile Strength	Increase	Increase	Decrease	Increase

The optimum parameters found are shown in the Table 3.

Table 3: Tang *et al's* Observed Optimum Printing Parameters[10]

	Parameter value
Laser Power (W)	190
Scan Speed (mm/s)	190
Scan Spacing (μm)	200
Layer Thickness (μm)	75

Yang *et al*[5] discussed the top surface quality of laser sintered copper and parameters that affect it, Figure 4. The typical defects are balling, warping, bad densification, and oxidation. They described that substrate plate flatness and cleanliness were crucial for top surface quality to prevent weak bonding between the initial layers and the substrate.

They also suggest utilizing gas atomized powder because of the shape and low oxygen content which results in a better part.
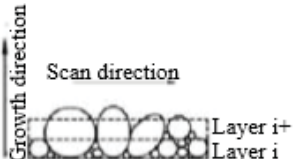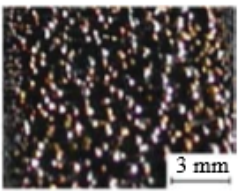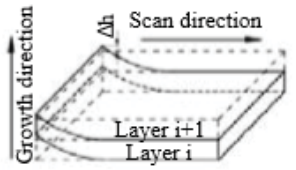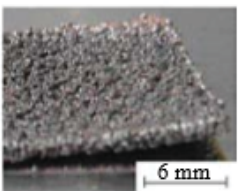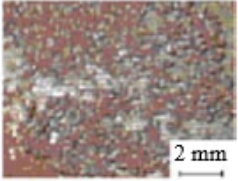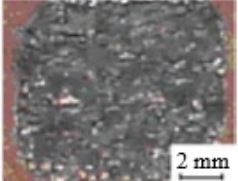
Type	Term	Description	Schematic	As-DMLFed photo
Flatness	Balling	There are a large number of sphere particles with different diameter in the current layer, and the height of maximal particles exceeds the layer thickness		
	Warpage	The solidified part curls seriously, which appears more easily in the edge or corner. When deformation exceeds layer thickness, DMLF process will be forced to terminate		
Compactness	Bad densification	It seems that the flatness of top surface is very good. However, metal powders are very slightly melted and arrayed with poor bonding strength		
Cleanliness	Oxidation	Local or entire oxidized area with black color exists in laser scanned area, which reduces seriously the stability of process and strength of metal parts		

Figure 4: Typical Surface Defects of Printed Parts made from Copper Based Powders using Laser Sintering, after Yang *et al*[11]

Becker and Wissenbach[12] discussed the way that low laser absorption and the high conductivity of copper powder (alloy Hovadur K220) caused the melt pool to ball and become unstable and discontinuous during scanning in the laser melting process. Most of the energy from the laser was either reflected off the powder or was quickly transferred away from the melt pool which caused cavities and reduced the density of the processed part. A high-density laser is needed to alleviate the ball effect. Instead of the normal 200W laser, they utilized a 1030 μm, 1000W Yb-YAG laser with a constant energy

output and obtained copper parts at almost 100% density. Becker and Wissenbach[12] also stated that a successful laser melting copper part can only be processed with a laser power above 300W.

In continuing Becker and Wissenbach[12] studies, Zhang *et al*[13] experimented with the formation parameters and their effect on the finished laser melting parts. A gas atomized copper alloy, C18400, with a mean diameter of 12µm was processed using various laser powers between 200W to 1000W. Laser power below 200W with a scan speed larger than 600mm/s created samples that had insufficient bonding to the substrate and created warpage and balling. Optimal forming parameters reflected laser powers between 200W to 400W and a scan speed above 100mm/s. At the high inputs the energy contacting the copper powder was so substantial that the powder overheated. Severe oxidation and evaporation was observed at high scanning speeds. Oxidation on the finished part was observed to be as high as 19.71 weight %. The melting point of copper oxide is higher than the melting point of copper. The oxide is present on the surface of the powder particles and creates a physical barrier to prevent wetting and increases the viscosity of the melt pool. Oxides will also gather along the grain boundary and will cause weak points.

Lykov *et al*[14] explained that most selective laser melting machines contain only a 200W laser. This paper showed that a 200W laser can be used to create acceptable parts. Using spherical pure copper powder at a mean diameter of 32.52µm, the finished part achieved a density of 88.1%. The part also displayed a satisfactory surface finish without dimensional inaccuracies. They mentioned that the CO_2 laser had a beam diameter of

35μm, which increased the power density. The laser melted part strength was 149MPa vs 221-379 MPa of wrought copper.

1.4 Processes to Obtain Copper Powder
1.4.1 Atomization

The atomization process commences by liquefying high purity copper in a melting furnace. Once completely liquefied, the molten copper is transferred to a holding furnace, Figure 5. The holding furnace utilizes induction heaters to maintain homogeneity and to provide a means for continuous movement of the molten metal. The second furnace also ensures that an uninterrupted atomization process occurs. A constant controlled stream of molten melt is released from the furnace. As metal flows through the orifice, it intersects with a high velocity jet of gas or liquid.[15] The jet contacts the particulates of the metal and quickly solidifies the particles. The particles are then processed through various meshes to control the size of the particles in the batch. Unable to pass through the mesh, oversized particles are sent back to the melting furnace to start the process over.
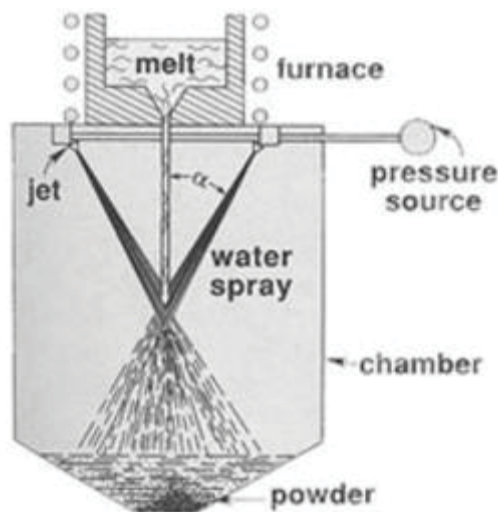
Figure 5: Atomization Process[16]

The shape and size of the metal particles are dependent on the medium used in the jet, the pressure of the jet stream, and the flow rates of both the jet stream and the molten metal. Water, air, and nitrogen are common mediums that are used in the jet stream.[17] The oxidation level of the atomization process will change the apparent density, shape of the particle, and the purity of the particle. To obtain pure copper powder, the atomization process is conducted in an atmosphere with little to no oxygen or in an inert gas environment. The atomization of powder is known for its spherical and irregular shape, show in Figure 6.
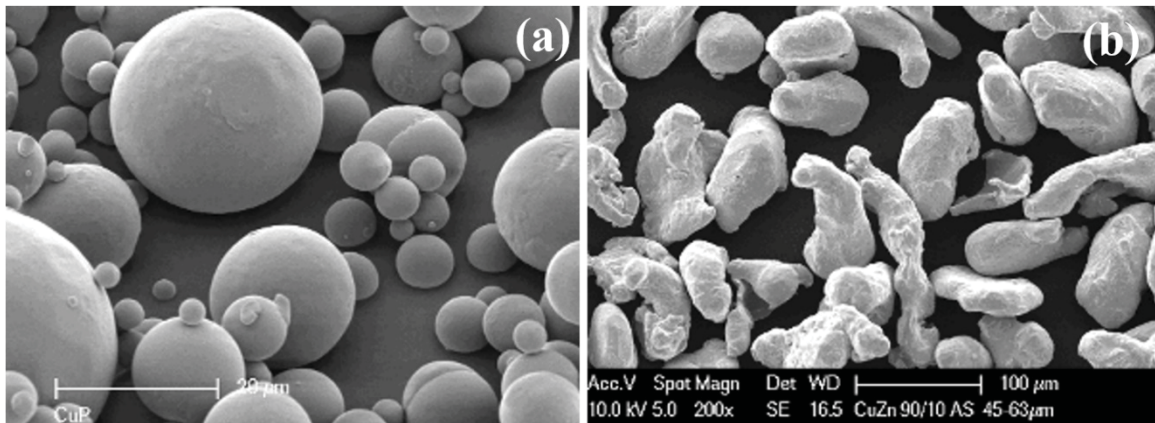
Figure 6: Spherical (a) and Irregular, (b) Air Atomized Powder[18]

1.4.2 Electrolysis

Electrolysis powder formation is also known as electrodeposition. An electrolytically refined copper anode and an antimonial lead cathode are placed in a dissolved metal salt solution called an electrolyte bath, Figure 7. An electric current is then applied to the anode. The anode metal slowly dissolves into the solution and collects on the cathode. After the deposition is complete, the copper on the cathode is collected and washed to remove the electrolyte solution. The powder that is created is brittle and reactive. To counteract these effects, the powder is annealed. Next, the powder is fed into high

velocity mills to break up the powder. The powder is then processed through various

meshes to control the size of the batch.[19]
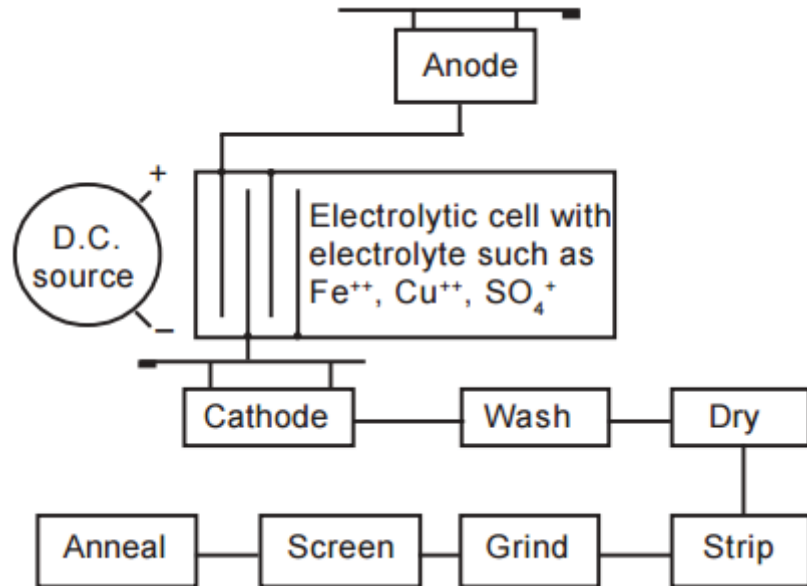
Figure 7: Powder Creation through Electrolysis Diagram[19]

Electrolytic copper powder is dendritic in shape, Figure 8. The apparent density and

other powder properties are typically controlled by the post electrolysis process.

Concentrations of sulfuric acid and copper sulfate in the electrolyte, as well as the current

density, can change the properties of the powder. Electrolytic powder is also known to

be of a high purity.[17]
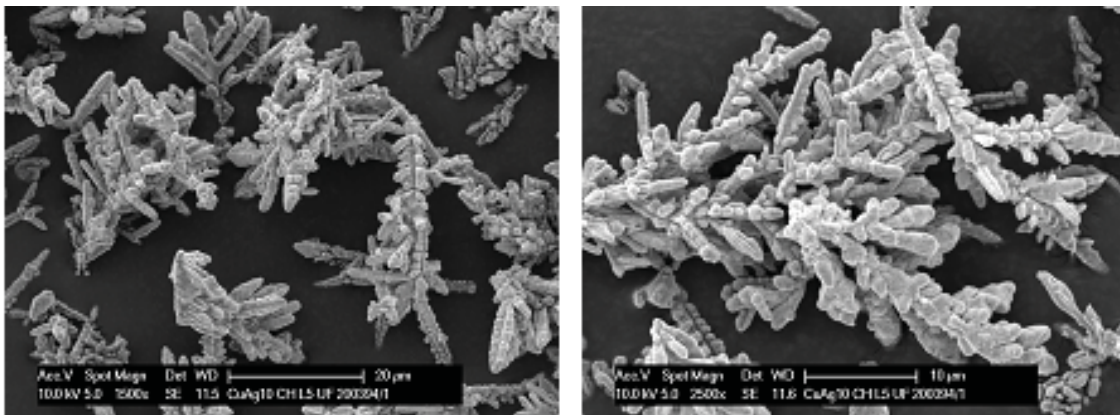
Figure 8: Dendritic Copper Powder without Post Processing[20]

Table 4 shows the properties for Cu powders produced by gas atomization and electrolysis.

Table 4: Properties of Copper Powder Produced by Various Methods[17]

	Atomized	Electrolytic
Copper, %	99-99.5	99-99.5
Weight Loss in H2, %	0.1-0.75	0.1-0.75
Acid Insoluble, %	0.5-0.1 max	0.03 max
Apparent Density, g/cm3	2-4	1.5-4
Flow, sec/50 g	20-35	30-40
Green Strength, MPa	nil-17.2	2.8-41.3
-325 mesh, %	25-80	5-90

1.5 Purpose for Thesis

Taylor-Winfield Technologies is exploring innovative ways to produce copper parts for their resistance welding electrical circuit that will reduce the cost and lead time of the copper parts. Additive manufactured copper parts may be a way to reduce lead time and may aid in the ease of producing water pathways in copper parts that are often difficult to manufacture because of complex geometry.   This thesis focusses on the additive manufacturing of copper parts for resistance welders using selective laser melting technology. The optimum printing parameters will be investigated as well as the mechanical properties of the additive manufactured parts. As a final verification, the additive manufactured parts produced in the thesis will be utilized in a resistance welder where results can be recorded. Numerical modeling of the heat transfer in typical resistance spot welder electrode/electrode adapter cooling water system will also be performed in order to increase the cooling system efficiency.

1.6 Objectives of Work

The objectives of the work were as follows:

- **Selected a Copper Powder for the Experiments:** The starting material should preferably be a powder that is identical to the copper alloys that are used in resistant welding circuits. The powder described above was not available, therefore pure copper was used. From the literary research, the powder should be spherical in shape with a mean diameter between 20-50µm.

- **Optimized the Printing Parameters for Processing the Selective Laser Melted Part:** The powder and the 200W laser printer were selected. The printing parameters such as part support type, exposure time, and laser scan speed were optimized. A visual inspection of the processed parts was performed to check for warpage, oxidation, and voids. Tensile tests were also performed on the processed parts at varying parameters to compare the ultimate strength with that of bulk copper properties. Some tensile tests specimens were sintered at 825°C for 24 hours and compared to non-sintered specimen mechanical properties.

- **Printed Resistance Welder Parts:** Upon obtaining optimized parameters, welder parts were printed. The geometry of the processed parts was examined. Parts with water paths were printed to test for water resistance.

- **Tested the Printed Parts Behavior in an Electrical Resistance Welder:** The printed parts were assembled on a resistance welder. A series of welds were created and tested with standard test procedures. The results were compared with welds created from conventional welder parts.

- **Numerical modeling:** The numerical modeling of the heat transfer in a typical resistance spot welder electrode/ electrode adapter cooling water system was investigated using Solidworks Flow Simulation. Two models using different internal geometry were compared to maximize the cooling rate of the electrode. The characteristics that were compared are:

  - Maximum temperature of the electrode over time

  - Maximum temperature of the water outlet over time

  - Heat flux of the system over time

A grid space and time step convergence were be completed to verify the results of the numerical analysis converged.

2.0 Experimental and Numerical Approach

2.1 Powder Selection

Powder selection is critical for laser printing of acceptable metal parts. For bus work and electrode purposes, Class 2 copper is commonly utilized. The chemical composition of Class 2 copper is presented in Table 5.

Table 5: Class 2 Copper Alloy Chemical Composition[21]

Material	Percent Weight (%)
Copper, Cu	Balance
Chromium, Cr	< 1.5
Zirconium, Z	< 0.25
Iron-Oxide, FeO_2	< 0.1
Silicone, Si	< 0.1
Lead, Pb	< 0.05

Unfortunately, Class 2 copper powder is currently not commercially available for additive manufacturing. At our (Taylor-Winfield Technologies) request one manufacturer, Sandvik AB, Denmark, experimented with trying to atomize Class 2 copper powder. The results of these experiments were inconclusive. Sandvik experienced issues with maintaining a homogenized alloyed atomized powder, and they couldn't provide the requested Class 2 copper metal powder.

Three gas atomized powders from ACuPowder International, LLC. were used instead. The copper powders used in this work, as well as their properties are listed in the Table 6 and Table 7.

Table 6: ACuPowder Copper Specifications (1 of 2)[22]

Powder Name, Manufacturer	Shape	Method of Production	Composition	Apparent Density (g/cc)
155A	Spherical	Air Gas Atomization	98.5% Cu	4.5-5.5
500A	Spherical	Air Gas Atomization	98.5% Cu	4.5-5.5
630	Spherical	Inert Gas Atomization (Nitrogen, N)	99.6% Cu	4.5-5.5

Table 7: ACuPowder Copper Specifications (2 of 2)[23]

Powder Name	Average Particle Size (µm)	Screen Analysis – Mesh Percent (%)		
		+200	+325	-325
155A	44.0	0.5 max	Balance	95.0 min
500A	28.0	0.5 max	Balance	99.0 min
630	37.5	n/a	n/a	n/a

Investigation and verification of the powder sizes, shapes, and chemical composition was performed by using the JEOL JSM7600-F Scanning Electron Microscope (SEM) equipped with EDAX Octane Plus X-ray Energy Dispersive Spectrometer (XEDS), Figure 9.

Figure 9: (a) JEOL JSM7600-F Scanning Electron Microscope, (b) XEDS detector indicated by arrow in (a).

Copper Powder 155A was selected to be utilized for the project.

2.2 Equipment utilized in the Printing Process

Three pieces of equipment were used during the additive manufacturing process. The three piece of equipment are:

- *Renishaw 250AM selective laser melting machine*: Utilized to create the 3-D printed parts.

- *2015 AGIE AC Progress VP2 EDM*: Utilized to cut printed parts from build plate.

- *Cen-Trump CNC mill*: Utilized to clean and resurface build plate for another build.

The Renishaw 250AM selective laser melting machine, Figure 10, performed the additive manufacturing of the copper parts from the selected powder. This machine was located at America Makes in Youngstown, Ohio. The Renishaw is a 240V 60Hz single phase powered machine with powder bed fusion technology that can handle powder sizes between 20μm to 100μm.   The working pressure of the machine is 101kPa. The 250mm x 250mm x 300mm build chamber is purged of oxygen (<2500ppm) and backfilled with argon before a build is started. An SPI model D laser (a component of the Renishaw machine) is used to create the builds.   The SPI laser is a 200W, continuous wave ytterbium fiber laser with a wavelength of 1070 nm and a beam size of 70 μm.[24]

Figure 10: Renishaw AM250 Laser Melting Machine[24]

Three-dimensional models were created using SolidWorks 2016 (SP1). The models were then imported as STL files into the mathematical differential program call MTT AutoFab (version 1.6). Using the FTP off the slicer program, the files where transferred to the Renishaw 250AM.

The Renishaw 250AM requires a machine specific build plate measuring 19mm tall x 248 x 248mm, Figure 11. For the project, the build plate is manufactured out of 316L stainless steel.
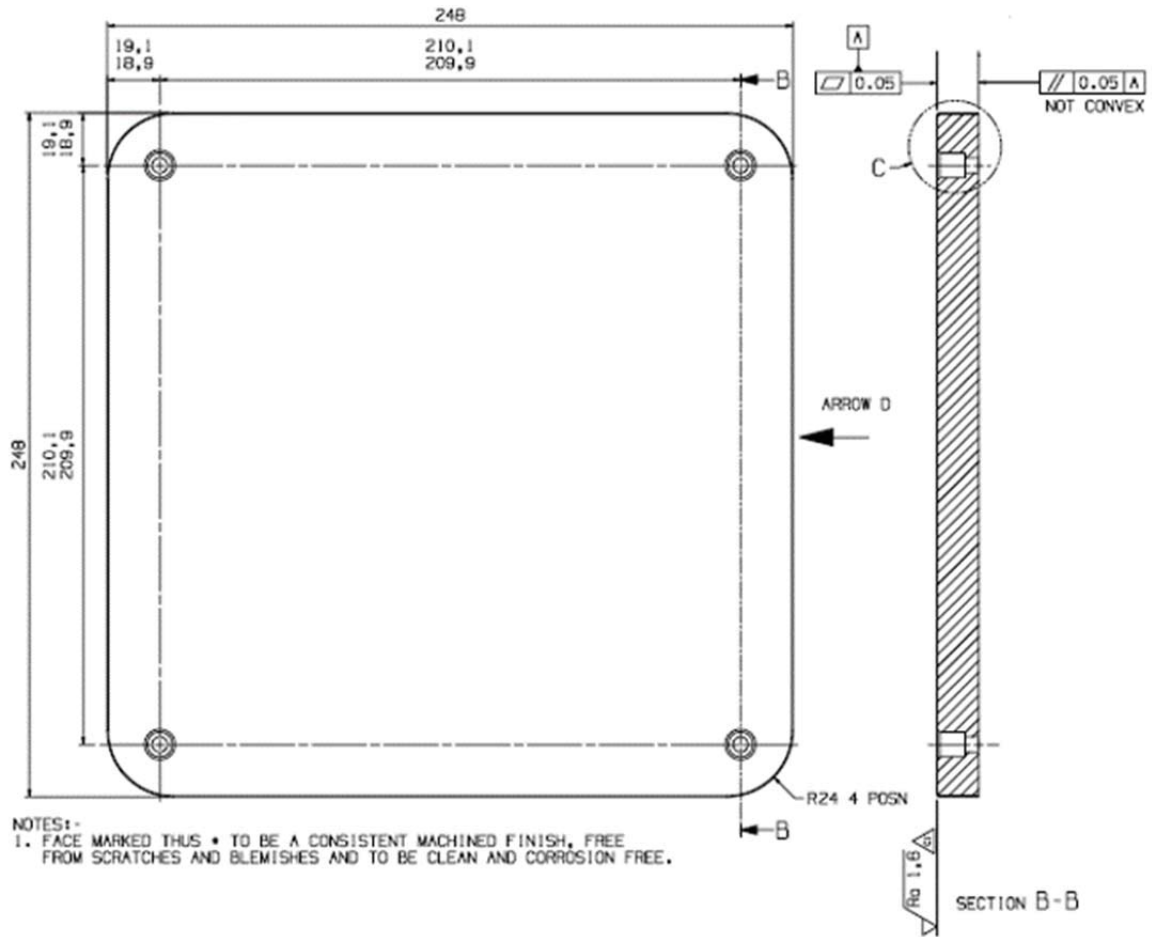
Figure 11: Renishaw 250AM Build Plate

To obtain optimal printing parameters, multiple coupon builds with varying parameters were completed. Tensile test specimens are created to test mechanical properties of the printed powder at varying build orientations and print parameters. The tensile test specimens shape dimensions were created in accordance of the ASTM standard E8 for powder metals, Figure 12.
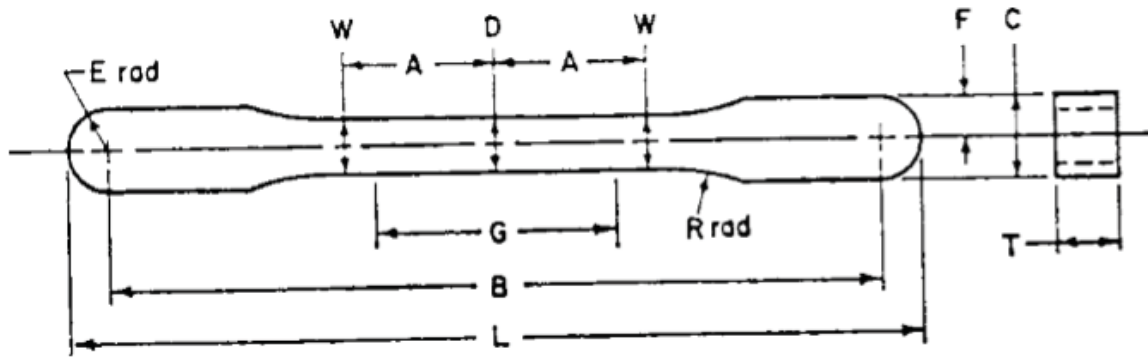
Pressing Area = 645 mm² [1.00 in.²]

Dimensions, mm [in.]	
G—Gage length	25.4 ± 0.08 [1.000 ± 0.003]
D—Width at center	5.72 ± 0.03 [0.225 ± 0.001]
W—Width at end of reduced section	5.97 ± 0.03 [0.235 ± 0.001]
T—Compact to this thickness	3.56 to 6.35 [0.140 to 0.250]
R—Radius of fillet	25.4 [1]
A—Half-length of reduced section	15.9 [0.625]
B—Grip length	80.95 ± 0.03 [3.187 ± 0.001]
L—Overall length	89.64 ± 0.03 [3.529 ± 0.001]
C—Width of grip section	8.71 ± 0.03 [0.343 ± 0.001]
F—Half-width of grip section	4.34 ± 0.03 [0.171 ± 0.001]
E—End radius	4.34 ± 0.03 [0.171 ± 0.001]

Figure 12: Tensile Test Specimen[25]

2.3 Additive Manufactured Part Mechanical Property Testing

2.3.1 Tensile Test Equipment

Additive manufactured tensile test specimens were created to gather the ultimate strength,

stress strain curves, and modulus of elasticity of the chosen parameters and orientations.

The tensile test machine utilized in the project was an Instron Model 5500R attached to a

4206 model base, Figure 13(a). The Instron had a 150 kN load cell. The geometrical size

of the 150 kN load cell is 10" long and 4.5" diameter. For the printed tensile test, standard

Instron grippers were used, Figure 13(b).
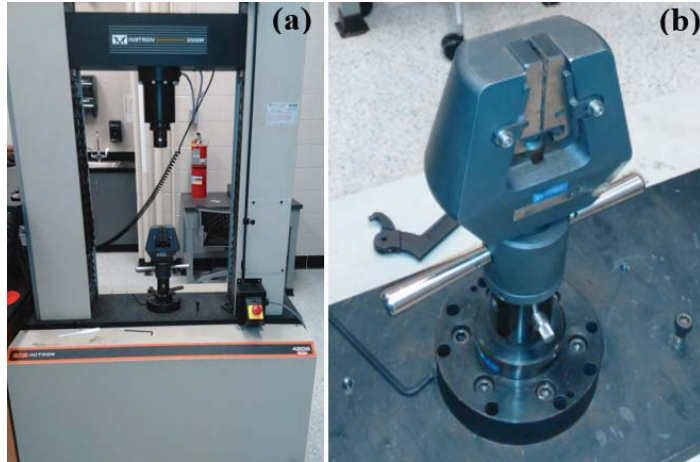
Figure 13: (a) Instron Tensile Tester, (b) Instron Standard Grippers

To measure strain, Omega quarter bridge strain gages were bonded in the middle of the specimen, as shown in Figure 14(a) and Figure 14(b). The measurements were automatically recorded through the P3 Strain Indicator and Recorder shown in Figure 15.
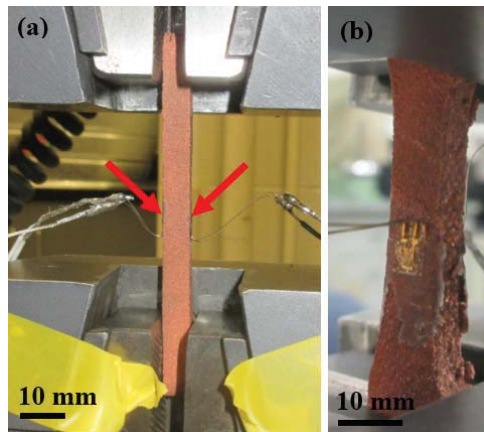
Figure 14: Test Specimen Setup (a) Strain Gauge Positions, Shown with Red Arrows; (b) Close-up of Strain Gauge

Figure 15: P3 Strain Indicator and Recorder

2.3.3 Additive Manufactured Part Leak Testing

Water circuits are a significant component of a secondary system in a weld circuit. As the temperature of the copper gets higher, the bulk resistance of the copper increases. This causes more restrictions in the necessary current flow and can cause a bad weld. Water cooling the copper ensures that any resistive heating is transferred away from the system. Additive manufactured copper is less dense than bulk copper. This test was completed to record if printed copper can contain water without leaking.

For this experiment, a copper block was printed. The leak test experiment was to plug one end of the block and place a hose fitting on the other end. The block had 3.8 liters per minute of water at 0.34 MPa applied. This condition was maintained until the block was verified as leak proof or started to leak.

2.4 Welding Experimentation
2.4.1 Welding Experiment Equipment

The welding experiment was completed on a Taylor-Winfield INV- ½ resistance spot welder, as shown in Figure 16. The weld cylinder was a 38.1 mm bore cylinder with a 38.1 mm stroke. At 0.55 MPa, the maximum weld force produced was 667 N. The weld capability of the machine was powered by a Portage #SF940048 air cooled 500 KVA AC transformer. The 480 V, 3 phase transformer was connected to the machine with #2 weld cables that were 457.2 mm long. The electrodes were 6.35 mm diameter and were made of RWMA Class 2 copper. The electrode holders were made of C110 and are shown in Figure 17.
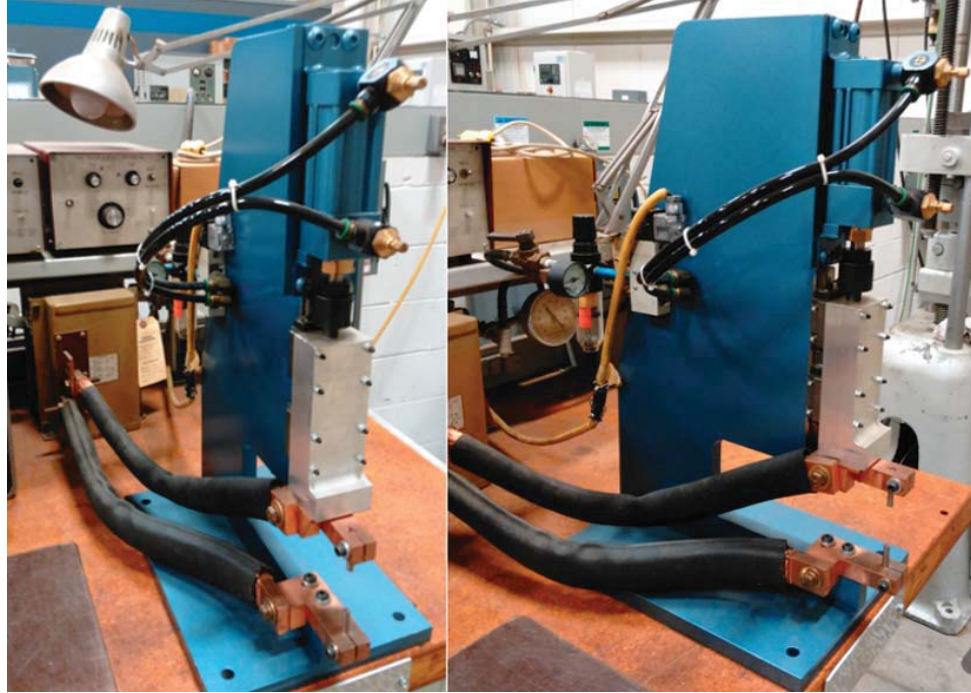
Figure 16: T-W Welder and Transformer
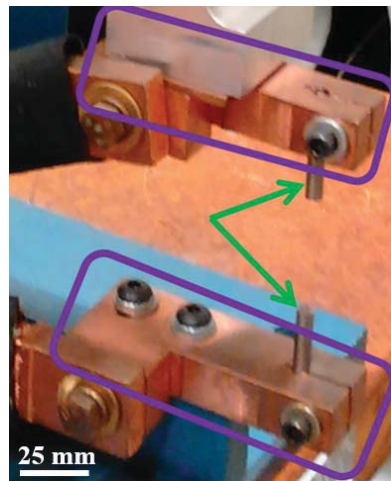
Figure 17: Welder Electrode Holders Shown with Purple Rectangles; and Electrodes Shown with a Green Arrow

2.4.2 Weld Quality Testing

Weld quality is determined by many factors. The factors that were applied to this study were the ultimate strength of the weld (in shear and tension), the modes of failure, the diameter of the spot weld, and the weld ductility. The modes of failure were ductile versus brittle, and the shear of the weld versus the tear of the parent material. A good quality weld is ductile in nature and tears at the parent material. Shearing of the weld

indicates a weak weld joint. The weld ductility is determined by the ratio between the tensile test ultimate strength to shear-tension ultimate strength.

The RWMA Standard tension-shear test is a quality test that applies tension to a single spot weld on a lapping joint, Figure 18. The load is applied to the destruction of the part. The ultimate strength and failure mode is recorded. In this experiment, the material was cut to the width, W, of 15.9 mm and the length, L, of 76.2 mm. The spot weld was centered within the specimen's width within 1.5 mm and 7.9 mm from the overlapped joint.[3]
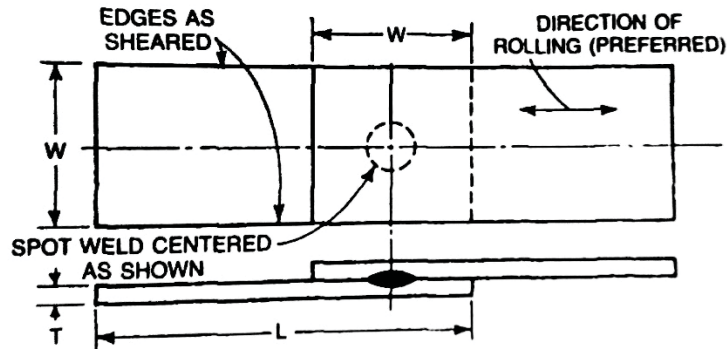
Figure 18: Single Spot Shear Specimen[3]

The RWMA Standard U-tension test is completed to measure notch sensitivity. Two "U" shaped specimens are welded together with a single spot weld, Figure 19. Spacer blocks are attached to the specimen and are pulled to the destruction of the part. The ultimate tensile strength, diameter of the weld, and the mode of failure are recorded.
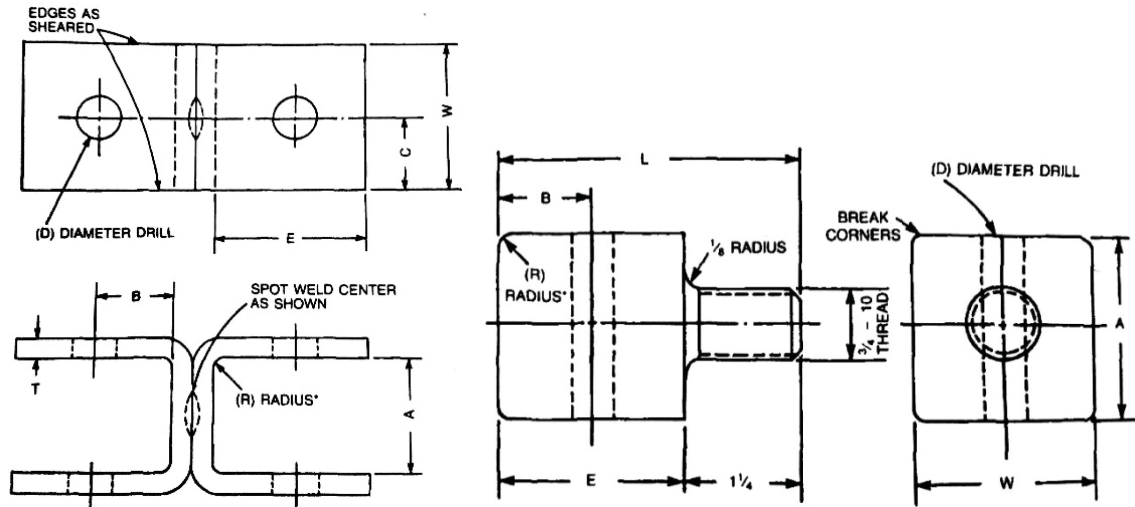
Figure 19: U-Tension Test Specimen and Spacer Block[3]

Table 8: U-Tension Test Specimen and Spacer Block Dimensions[3]

Dimensions (mm)	W	A	B	C	D	E	R	L
Specimen	25.4	25.4	12.6	12.6	7.9	25.4	7.9	N/A
Spacer Block	25.4	25.4	12.6	12.6	8.73	25.4	7.9	57.15

2.4.3 Welding Test Groups

Six welding test groups were completed on the INV- ½ machine:

1. **Test Group 1** – The spot welded tensile test specimens were welded utilizing electrodes and electrode adapters that were created by conventional fabrication methods. The electrodes were fabricated from C110 copper. C110 copper is 99.9% pure copper and is comparable to the material composition of the additive manufactured powder selected for this thesis. The weld schedule was established for group 1 and was utilized for Test Groups 2 & 3.

2. **Test Group 2** – The spot welded tensile test specimens were welded utilizing electrodes and electrode adapters created by conventional fabrication methods. Per the typical industrial configuration, the electrodes were to be fabricated from RWMA Class 2 copper.

34

3. **Test Group 3** – The spot welded tensile test specimens were welded utilizing the conventionally fabricated RWMA Class 2 copper and the electrode adapters were created by additive manufacturing methods.

4. **Test Group 4** – The same physical configuration of Test Group 3 was utilized. However, the weld control percent power was increased to achieve the same current density as seen in Test Groups 1 and 2. Current density is the amount of current passed through the weld circuit during the weld divided by the surface area of the electrodes. If the electrodes are dissimilar in size, the smaller electrode is used in the calculation of current density.

5. **Test Group 5** - The spot welded tensile test specimens were welded utilizing electrodes and electrode adapters created by additive manufacturing methods.

6. **Test Group 6** - The spot welded tensile test specimens were welded utilizing electrodes and electrode adapters that were created by additive manufacturing methods. The additive manufactured electrodes were sintered at 825°C for 24 hours.

From each test group, 10 specimens were welded. During each weld, the weld current was measured and recorded by a Miyachi Weld Checker, Model MM-326B, shown in Figure 20. After each weld was performed, the upper and lower electrode tip diameters were recorded. Ten specimens were created for the shear-tension test. The other 10 specimens were created for the U-tension test. The data collected from Test Group 1 and Group 2 represents the control group of data. The data from Group 1 and Group 2 was compared to evaluate the effects of changing from RWMA Class 2 alloyed copper to a purer form of copper on the weld strength and nugget size. Test Group 3 and 4 evaluated

the weld quality of a mixed secondary circuit. Test Groups 5 and 6 evaluated the weld quality of a complete additive manufactured secondary circuit and compared the weld performance of additive manufactured electrodes, both pre-sintered and post-sintered.

Figure 20: Miyachi Weld Checker

2.4.4 Weld Specimens

The weld specimens were Precision Brand Branded shim stock. The material of the shim stock is full hard, cold rolled, low carbon 1008-1010 steel. The thickness was 32 gauge (.254mm ±.01905mm). The material was flat and was free of burrs, grease, scale, and other foreign coatings. The specimen size was dependent on the type of weld quality testing to be completed. Two weld quality tests performed were the tension shear test specimen and the U-tension tensile test. Both tension tests utilize the Instron machine shown in Figure 13(a). The tension shear test specimen used the same grippers as the AM tensile test. The set-up is shown in Figure 21. The U-tension tensile test used custom grippers combining the Resistance Welding Manufacturing Alliance (RWMA) standard spacer block in Figure 19 with an adapter to the Instron machine tooling, shown in Figure 22.

Figure 21: Shear Tensile Test on Instron
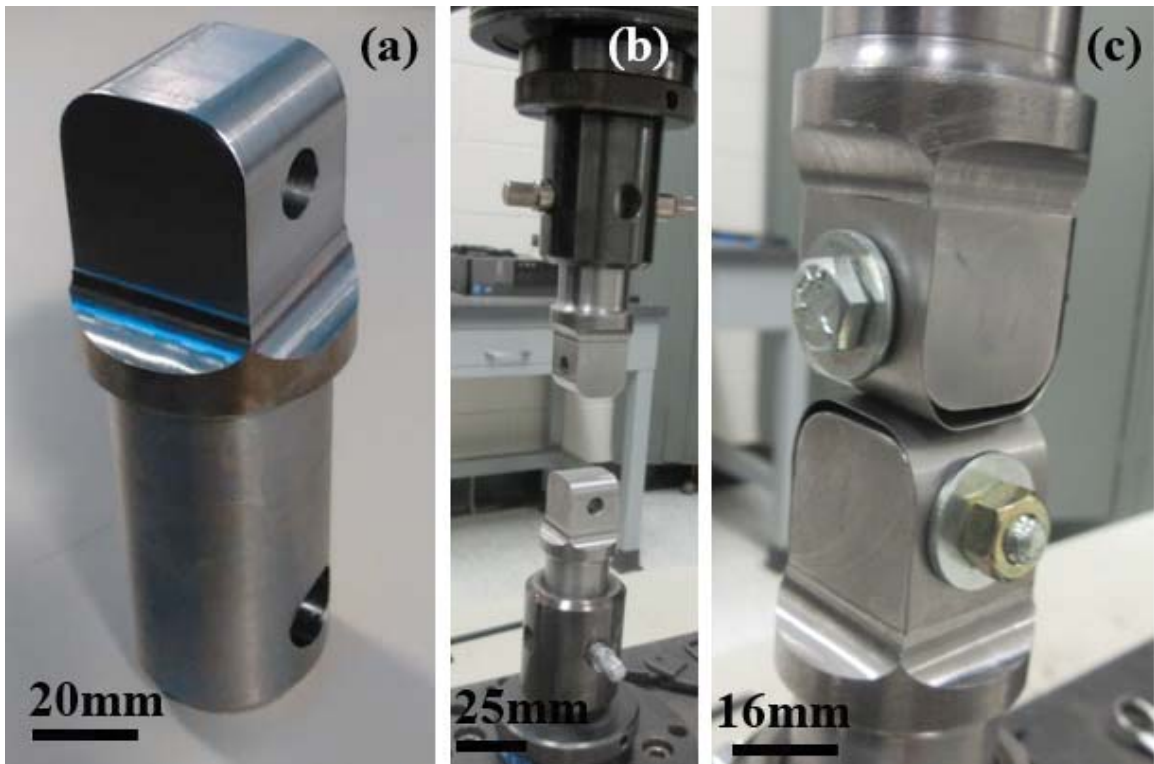
Figure 22: U-Tension Tensile (a) Specimen Holder, (b) Tooling in Instron (c) Specimen on Tooling

2.4.5 Additive Manufactured Electrodes and Electrode Adapters

Using the optimized parameters, the resistance welder parts of the upper electrode holder, lower electrode holder, and electrodes were printed. Due to the quality of the printed parts, extra stock was added to the electrodes and electrodes holders. The printed parts were then machined to the final dimensions. The electrode holders were machined on a Bridgeport Mill, serial number J308818. The electrode was machined on a Bridgeport E-Z Path Lathe, serial number 002-081566-225. These parts were fastened to the welder and used for the welding tests.

2.5 Numerical Modeling

Numerical modeling of the electrode/electrode adapter body heat transfer was created on a Dell Precision T5610 solid state, 24 core processor using SolidWorks Premium 2016 x64 Edition SP 5.0. The simulation analysis was performed on the same computer using the SolidWorks Flow Simulation SP 5.0 Build 3591 software (referred to as SFS for the rest of the document). For incompressible flows or flows with a MAC number less than three (3), SFS uses time-implicit approximations of continuity and convection/diffusion equations with an operator splitting technique to resolve pressure-velocity decoupling. SFS uses the SIMPLE Algorithm (Semi-Implicit Method for Pressure Linked Equations) presented by Patankar[26].

3.0 Results and Discussion

3.1 SEM Investigation of Copper Powders Used in AM

Samples for SEM analysis were prepared as follows. A small scoop of each powder was placed on a glass slide. Double sided conductive carbon tape was applied to three aluminum SEM stubs. Each piece of conductive tape was pressed into one of the copper powders. Loose powder on the conductive tape was removed with compressed air. The aluminum stubs were placed into the JEOL holders, Figure 23, and the holders were inserted in the SEM's sample chamber. One observation noted during the loading of the powder was that the 630 powder was electrostatically charged and proved difficult to work with. When scooped from the bag, the charged powder would cling to the bag, jump off the scoop, and would reattach to the plastic bag.
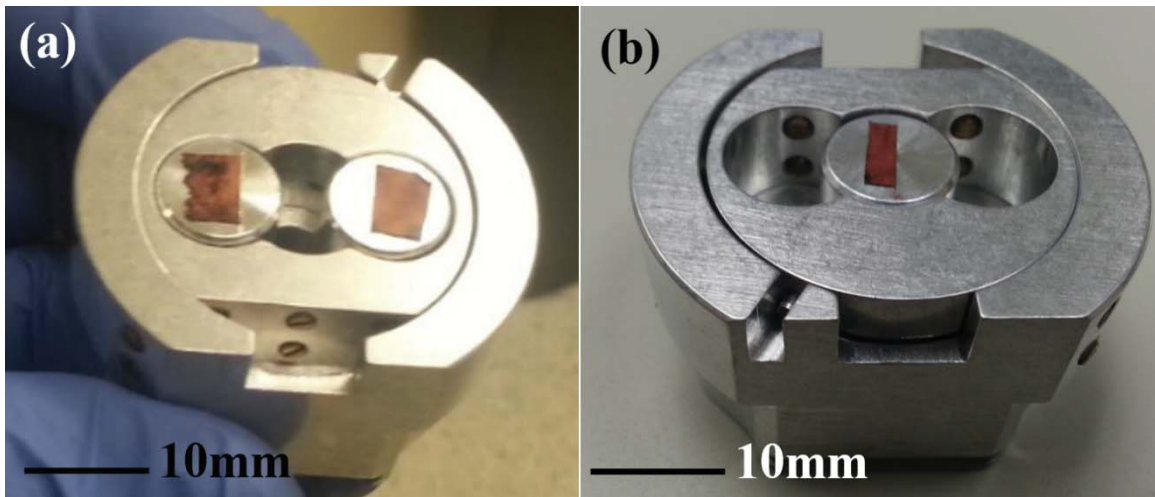
Figure 23: SEM holders with (a) Copper Powders 155A (Left Position) and 500A (Right Position), (b) 630 Powder

The backscatter electron (BSE) micrographs shows the purchased powders have uniform chemical composition, Figure 24. This was confirmed by chemical analysis using XEDS technique. The XEDS spectrum in Figure 25 shows the 155A powder is mostly Cu, with small amount of oxygen being detected. It is assumed the oxygen is due to a copper oxide

layer formed at the surface of the powders, during the powders explosion to air.   Powder

155A was confirmed as a spherical powder, Figure 26(a). The size of the powder ranged

from 8 µm to 40 µm in diameter.   Powder 500A was also observed to be spherical in

shape, Figure 26(b). However, more irregular particle shapes were observed in the 500A

sample. Powder 630 was observed to have spherical shaped particles but also had many

irregular particles as well, Figure 26(c).
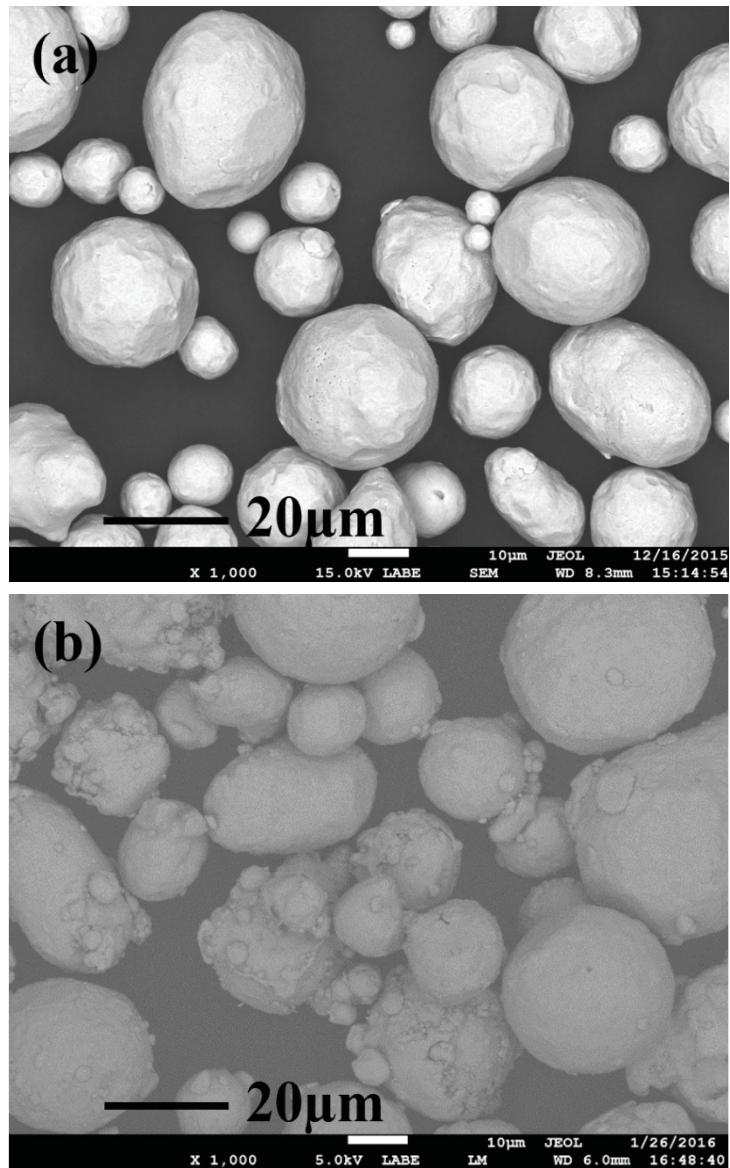
Figure 24: Backscatter electron (BSE) micrographs of (a) 500A, (b) 630 powders
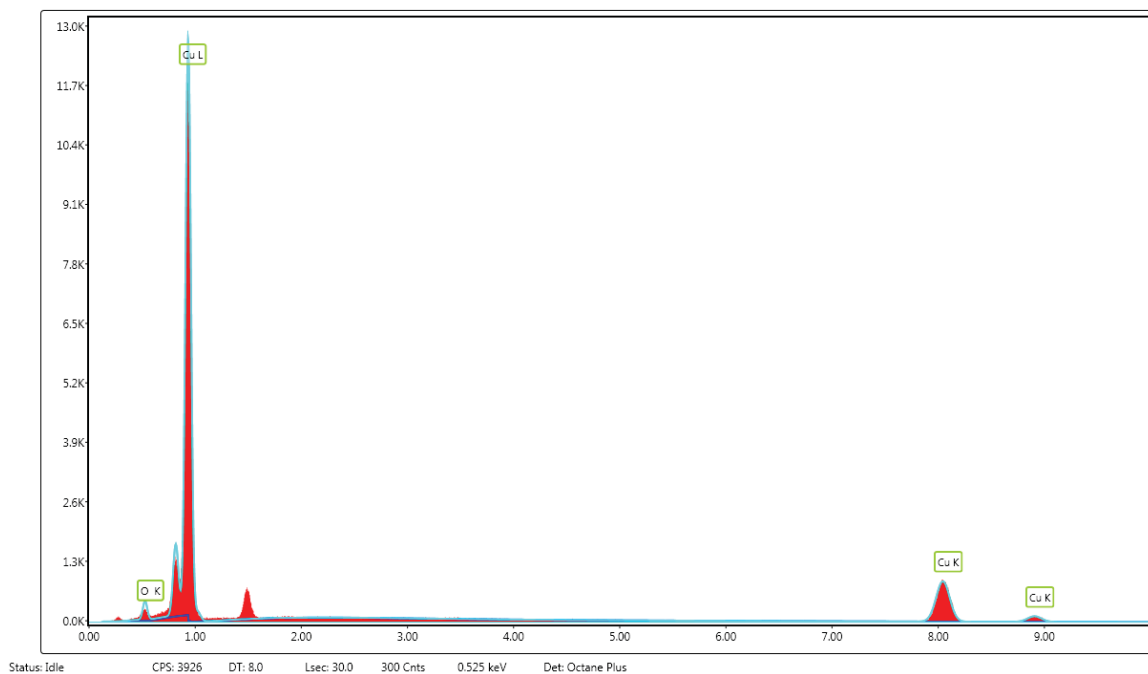
Figure 25: XEDS Spectra of 155A copper powder.

The quantitative chemical composition of the powders is presented in Table 9.

Table 9: ACuPowder Copper Specifications Observed the SEM and EDAX

Powder Name	Largest Particle Size (μm)	Chemical Analysis – Weight Percent (%)	
		Cu	O
155A	46.7	93.14	6.86
500A	47.0	95.32	4.68
630	40.0	97.90	2.10
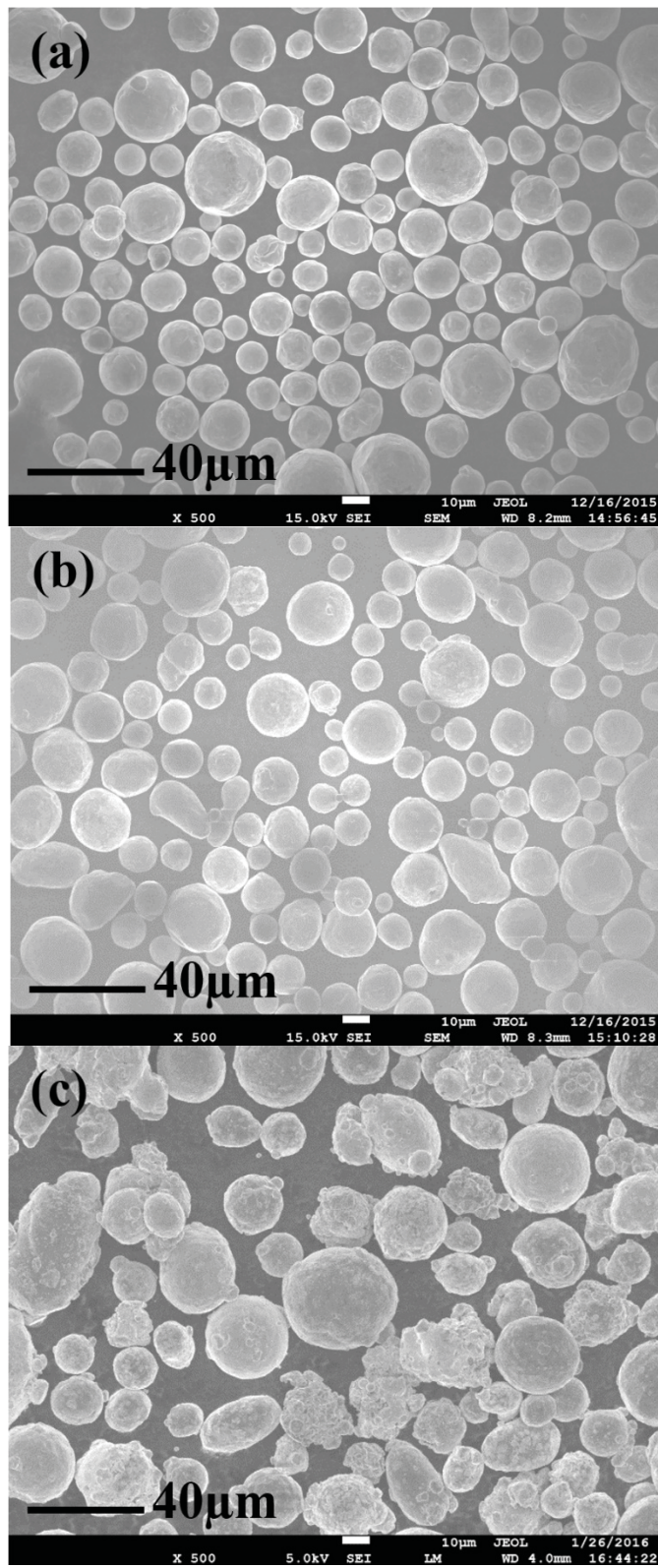
Figure 26: Secondary electron (SE) micrographs of copper powders: (a) 155A, (b) 500A, and (c) 630

The powder that was selected for the experiments was 155A. Although the powder appeared to contain a larger oxygen level compared with 500A and 630, the powder was selected due to both particles spherical shape (better particle flow during printing), as well as larger size spread (better packing density of the powder, resulting in higher density of the printed product). Although the purest and smallest of the copper powder, the charged properties of the 630 powder and its irregularities prevented the powder from properly flowing though the additive manufacturing process.

3.2 Optimization of Printing Parameters

Powder 155A was loaded into the Renishaw's powder hopper. The build plate was cleaned with isopropyl alcohol, leveled, and fixed inside of the machine. For Batch624, six coupons 22.5mm x 22.5mm x 5mm tall were designed for printing trials. The sketch of the base plate and the positions of the coupons used for finding the optimal parameters for copper powder printing are shown in Figure 27. The use of supports versus a solid substrate bond was tested in this batch along with various laser scanning speed parameters. The coupon base and border supports are shown in Figure 28.
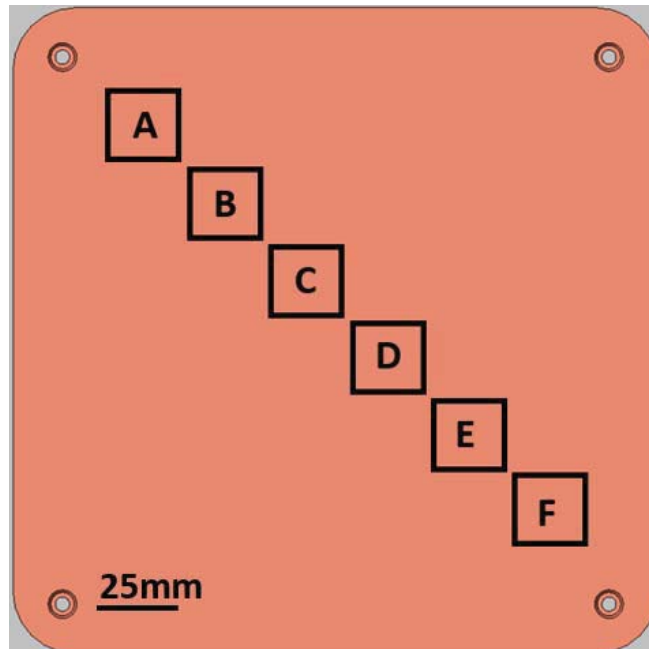
Figure 27: Batch624 Layout & Coupon Names
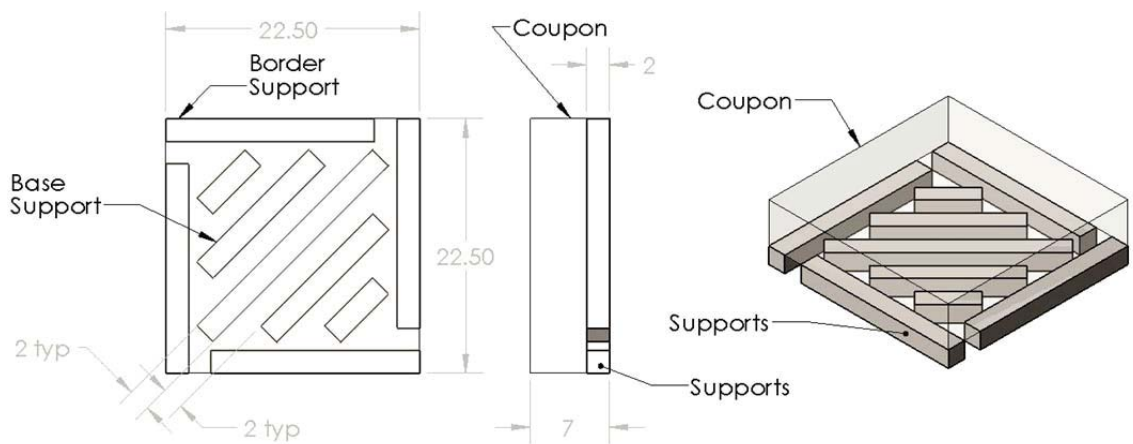
Figure 28: Coupon Support Structure

The parameters used for printing individual coupons are shown in Table 10.

Table 10: Batch624 Parameters

Parameter	A	B	C	D	E	F
Layer Thickness (µm)	45	45	45	45	45	45
Travel Speed (mm/s)	510	510	495	495	480	480
Power (W)	200	200	200	200	200	200
Focus Offset (mm)	0	0	0	0	0	0
Point Distance (µm)	25	25	25	25	25	25
Exposure Time (µs)	100	100	100	100	100	100
Support	Yes	No	Yes	No	Yes	No

Figure 29 shows the appearance of the A to F coupons after printing.

44
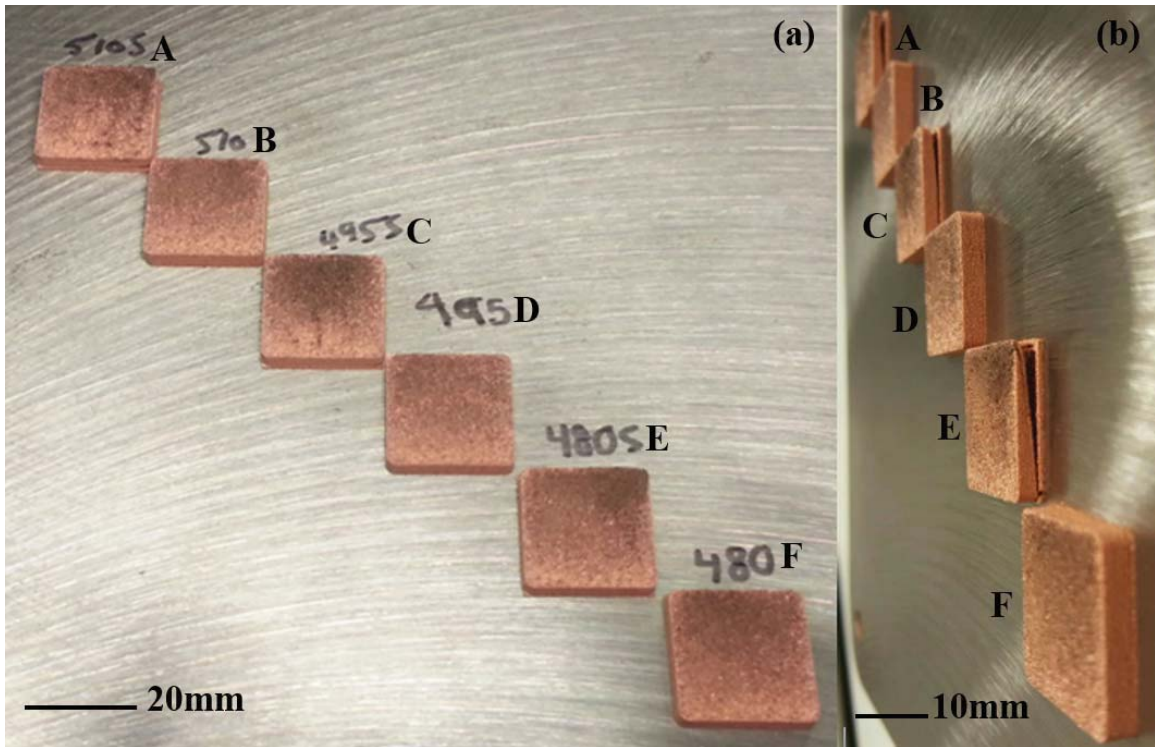
Figure 29: (a) Batch624 Finished Top View, (b) Right View.

Batch624 was terminated early due to the delamination of the coupon from the supports on samples A, C, and E. Out of all the coupons, B had the highest density, displayed the most dimensional accuracy, and exhibited the best surface finish. Bonding the copper to the substrate produced a stronger bond and therefore was used for all subsequent builds.

Batch625, Figure 30, used coupons that were the same size as Batch624. With a scanning speed of 500 mm/s, the exposure time was varied from 70 µs to 130 µs. The printing parameters for Batch625 are presented in Table 11.
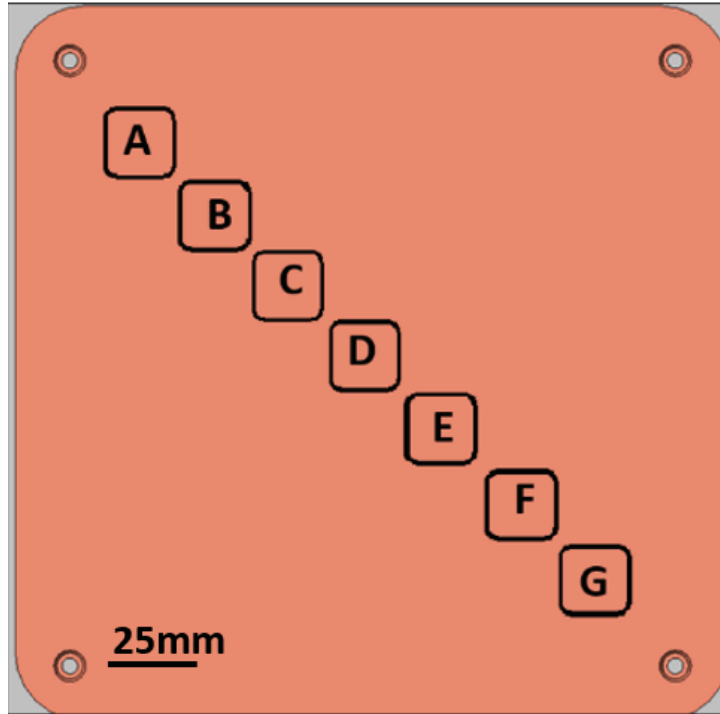
Figure 30: Batch625 Layout & Coupon Names

Table 11: Batch625 Parameters

Parameter	A	B	C	D	E	F	G
Layer Thickness (µm)	45	45	45	45	45	45	45
Travel Speed (mm/s)	500	500	500	500	500	500	500
Power (W)	200	200	200	200	200	200	200
Focus Offset (mm)	0	0	0	0	0	0	0
Point Distance (µm)	25	25	25	25	25	25	25
Exposure Time (µs)	70	80	90	100	110	120	130
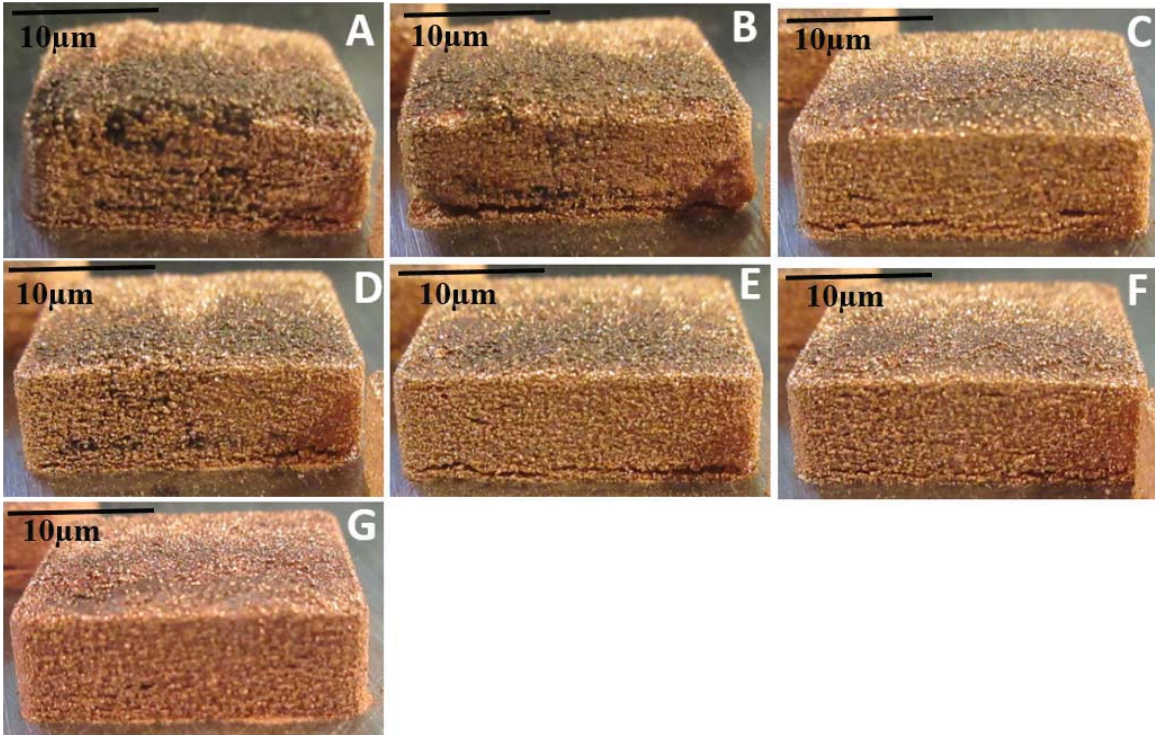
Figure 31: Batch625 Results; (A) 70µs, (B) 80µs, (C) 90µs, (D) 100µs, (E) 110 µs, (F) 120µs, and (G) 130µs

Figure 31 displays Batch625's printing results. Coupons A through F experienced delamination from the build plate. Coupons A and B displayed severe delamination from the build plate and warping. Coupon B showed less warping and balling than A. Coupons E and F only showed slight delamination from the build plate. Coupons E through G displayed little to no warpage or balling. Coupon A displayed the most severe warpage, delamination, and balling. Coupon G showed no visual warping, balling, or delamination. Coupon A's surface roughness was measured to be around 1000 µm Ra. Ra is mean roughness or the arithmetic average of all the peaks and valleys of a surface and commonly used in engineering industry. Coupon G's surface roughness was measured to be around 500 µm Ra. As the time of exposure lengthened, the coupon's dimensional accuracy, surface finish, and density improved. Due to oxidation, all coupons contained dark areas.

Table 12 reviews all parameters used in preliminary printing and the highlights the optimal printing parameters found through visual inspection, without mechanical testing.

Table 12: Preliminary Printing Parameters

Printing Parameter Scenarios	Printing Parameter Variables					
	Layer Thickness (µm)	Travel Speed (mm/s)	Power (W)	Focus Offset (mm)	Point Distance (µm)	Exposure Time (µs)
1	45	525	200	0	25	100
2	45	510	200	0	25	100
3	45	495	200	0	25	100
4	45	480	200	0	25	100
5	45	465	200	0	25	100
6	45	435	200	0	25	100
7	45	405	200	0	25	100
8	45	375	200	0	25	100
9	45	500	200	0	25	70
10	45	500	200	0	25	80
11	45	500	200	0	25	90
12	45	500	200	0	25	100
13	45	500	200	0	25	110
14	45	500	200	0	25	120
15 & Best	**45**	**500**	**200**	**0**	**25**	**130**

3.3 Mechanical Properties of Additive Manufactured Tension Test Specimens

Batch812 was a set of tensile test specimens that were printed flat with varying laser exposure time, Figure 32(a). Batch627, Figure 32(b), contained tensile test specimens that were printed with the optimal printing parameters found in section 3.2. Batch715 consisted of two sintered tensile test specimens that were printed flat against the substrate. These specimens were encapsulated in a vacuum quartz tube and sintered at 825°C for 24 hours. Batch715 was tested to analyze the effects that sintering had on the mechanical properties of the additive manufactured parts. Table 13 shows the printing parameters of Batch815, Batch627, and Batch715.

Table 13: Batch815 and Batch627 Printing Parameters

Printing Parameter Scenarios	Printing Parameter Variables					
	Layer Thickness (μm)	Travel Speed (mm/s)	Power (W)	Focus Offset (mm)	Point Distance (μm)	Exposure Time (μs)
Batch815	45	500	200	0	25	120
	45	500	200	0	25	110
	45	500	200	0	25	100
	45	500	200	0	25	90
	45	500	200	0	25	80
Batch627	45	500	200	0	25	130
Batch715	45	500	200	0	25	130

Five of Batch627 specimens were flat against the substrate, while other five specimens were edge-built against the substrate. This batch was created to test if print orientation made a difference in strength and integrity.
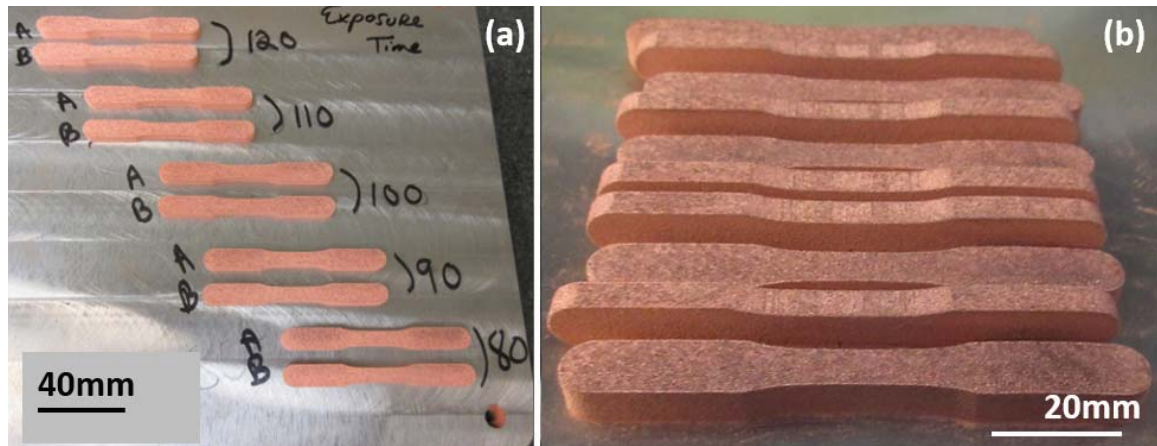
Figure 32: (a) Finished Prints, Batch815; (b) Batch627

The tensile test specimens were tensile tested on the Instron in the configuration shown in Figure 33 at a rate of 1 mm/min. The specimens were pulled until fracture occured.
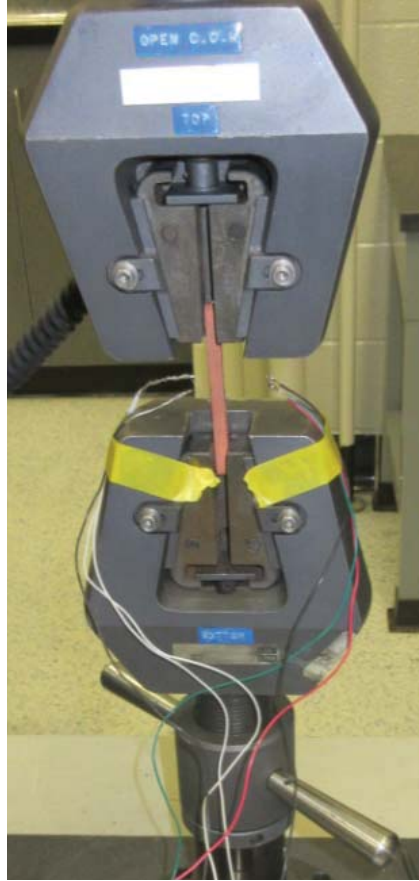
Figure 33: Tensile Test Setup

The maximum strength and the modulus elasticity found by the tensile tests are shown in

Table 14, Table 15, and Table 16.

Table 14: Batch617 Mechanical Properties

Sample No. (Printed Flat Against Substrate)	Maximum Strength (N/m^2)	Modulus of Elasticity (N/m^2)	Sample No. (Edge-Built Against Substrate)	Maximum Strength (N/m^2)	Modulus of Elasticity (N/m^2)
B627-1	1.822E+07	1.006E+10	**B627-1S**	2.336E+07	2.078E+10
B627-2	2.669E+07	1.908E+10	**B627-2S**	2.110E+07	2.269E+10
B627-3	2.194E+07	2.687E+10	**B627-3S**	2.461E+07	2.058E+10
B627-4	2.782E+07	2.080E+10	**B627-4S**	1.998E+07	1.837E+10
B627-5	2.977E+07	2.018E+10	**B627-5S**	2.162E+07	2.050E+10
AVERAGE	**2.489E+07**	**1.940E+10**		**2.213E+07**	**2.059E+10**
STD DEV.	**4.714E+06**	**6.035E+09**		**1.844E+06**	**1.531E+09**

Table 15: Batch815 Mechanical Properties

Sample No.	Maximum Strength (N/m^2)	Modulus of Elasticity (N/m^2)	Sample No.	Maximum Strength (N/m^2)	Modulus of Elasticity (N/m^2)
B815A-80	1.770E+07	1.519E+10	B815A-110	` 1.646E+07	2.199E+10
B815B-80	1.323E+07	1.653E+10	B815B-110	1.555E+07	1.551E+10
AVERAGE	1.547E+07	1.586E+10		1.600E+07	1.875E+10
STD DEV.	3.158E+06	9.442E+08		6.427E+05	4.583E+09
B815A-90	1.830E+07	2.143E+10	B815A-120	1.797E+07	1.122E+10
B815B-90	2.069E+07	1.702E+10	B815B-120	1.595E+07	1.434E+10
AVERAGE	1.950E+07	1.923E+10		1.696E+07	1.278E+10
STD DEV.	1.694E+06	3.114E+09		1.435E+06	2.208E+09
B815A-100	1.075E+07	1.403E+10			
B815B-100	1.452E+07	1.489E+10			
AVERAGE	1.264E+07	1.446E+10			
STD DEV.	2.667E+06	6.043E+08			

Note: The last number of sample's label represents the laser exposure time parameter of the sample. For example, B815A-**80** has an exposure time of **80μs**.

Table 16: Sintered Batch715 Mechanical Properties

Sample No.	Maximum Strength (N/m^2)	Modulus of Elasticity (N/m^2)
B715-3	2.611E+07	6.874E+10
B715-5	2.438E+07	3.932E+10
AVERAGE	2.524E+07	5.403E+10
STD DEV.	1.229E+06	2.080E+10

As seen in Table 14, the maximum strength of the samples printed flat against the substrate was larger than the samples printed edge-built against substrate. The flat printed parts were created with a smaller number of layers than the edge-built parts. Having fewer printed layers reduces the grain growth due to reheating. Grain boundaries within a material prevent plastic deformation from spreading due to the varying grain slip system orientation between the grains. Therefore, smaller grains caused the printed parts to have a higher maximum strength and fracture resistance.[27] The modulus of elasticity was higher for the edge-built against substrate specimens. The smaller cross section per printed layer also reduced the length of the laser raster lines. Shorter raster lines reduced

the residual stress of the part and increased the modulus of elasticity.[4]　　Figure 34 and

Figure 35 show the stress strain curves of Batch627.　The edge-built specimens had a

more uniform stress strain curve. The smaller print cross-section caused less warping and

delamination during the build process.[4] Reducing these negative effects of warping and

delamination caused the printed part to have more consistent mechanical properties.
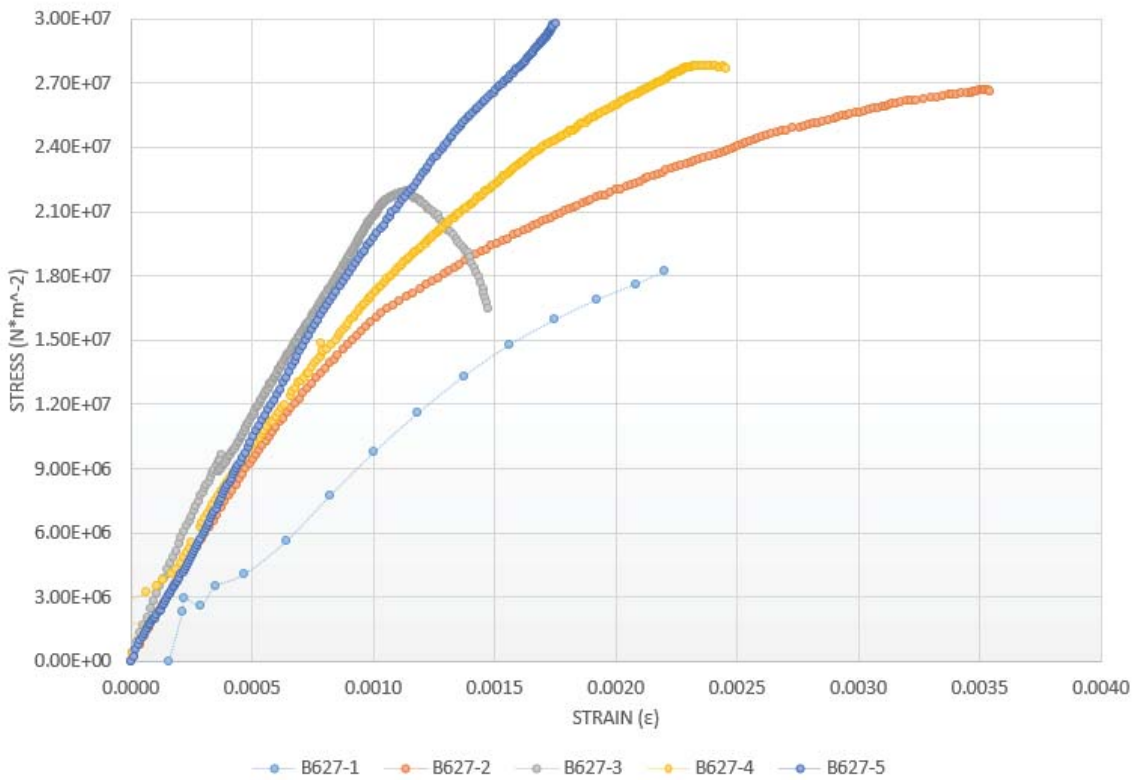
Figure 34: Batch627 Flat Orientation Stress-Strain Curve
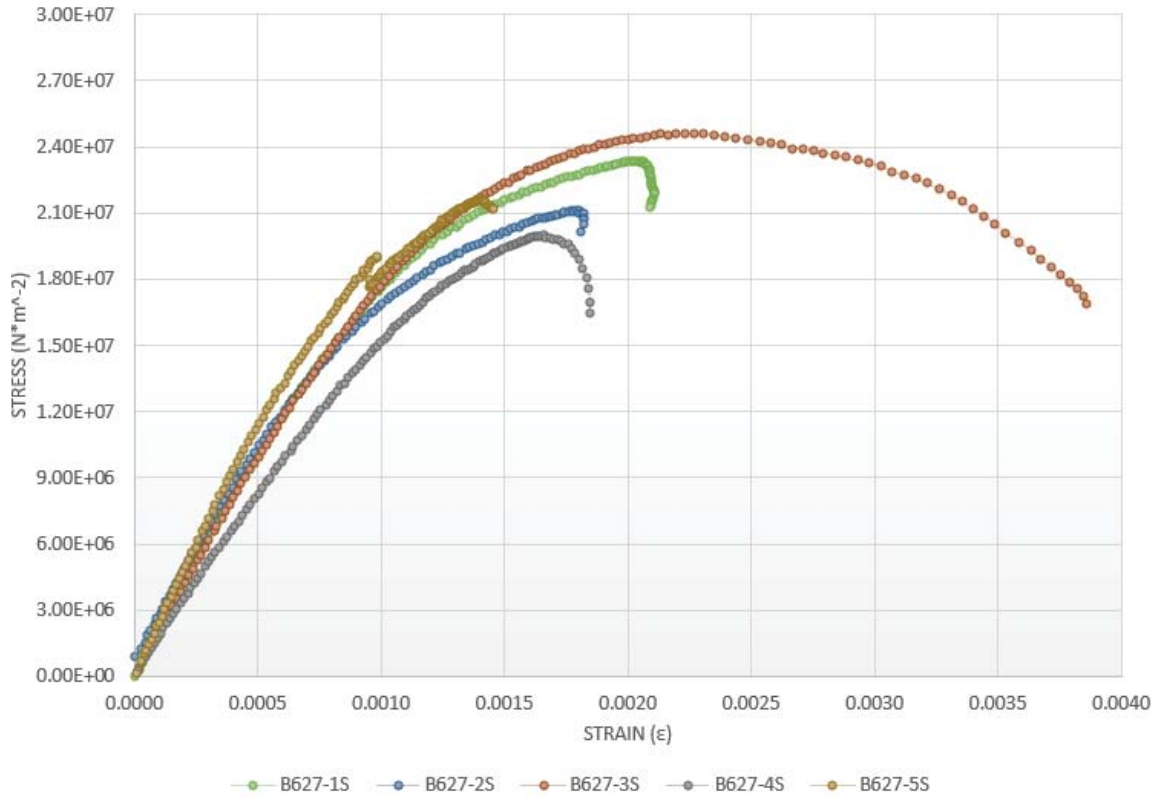
Figure 35: Batch627 Edge-Built Orientation Stress-Strain Curve

As seen in Table 15, the laser exposure time of 90 µs had the largest strength and modulus of elasticity when compared to all the other exposure times. With all other parameters remaining constant, the 90µs specimens displayed the optimum laser exposure time. The slower laser exposure time (such as 80 µs) can cause balling, smaller melt pools, and weaker bonds between the layers.[4] The larger exposure times (100-120 µs) increased the laser density which caused higher residual stress cracks. Higher residual stress cracks can lead to delamination.[4] Longer exposure times reduced scan speeds and were shown to reduce strength.[9] Figure 36 shows the stress strain curves of all the different exposure times. Only a small number of specimens were used for this test. For more accurate analysis, more specimens at each exposure level need to be printed and tested.
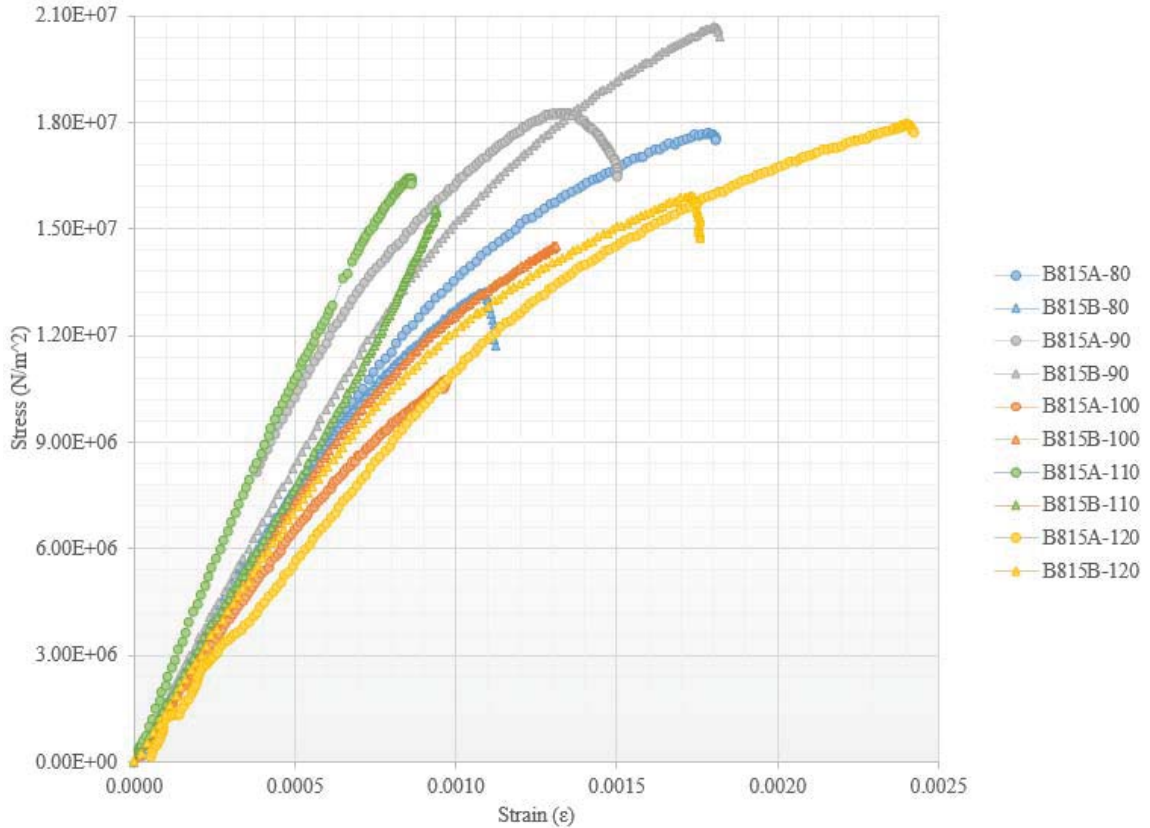
Figure 36: B815 Exposure Time Variation Stress Strain Curve

Table 16 displays the results from the sintered tensile tests. The sintered parts in both their maximum strength and modulus of elasticity exceed all the other specimens. The superiority in mechanical properties was due to the sintering process. During the sintering process, the contact surface between particles within the printed part increased. The increased contact surface caused the bond between the particles to increase. As the sintering process continued, particles fully coalesced into new, larger particles. The sintered parts shrunk and became denser.[28] Holding the printed specimens at high temperatures for extended periods of time reduced the number of voids, cracks, and residual stresses within the part. Figure 37 shows the stress strain curves of the sintered parts. Figure 38 shows the stress strain curve comparison of all the printed specimens.
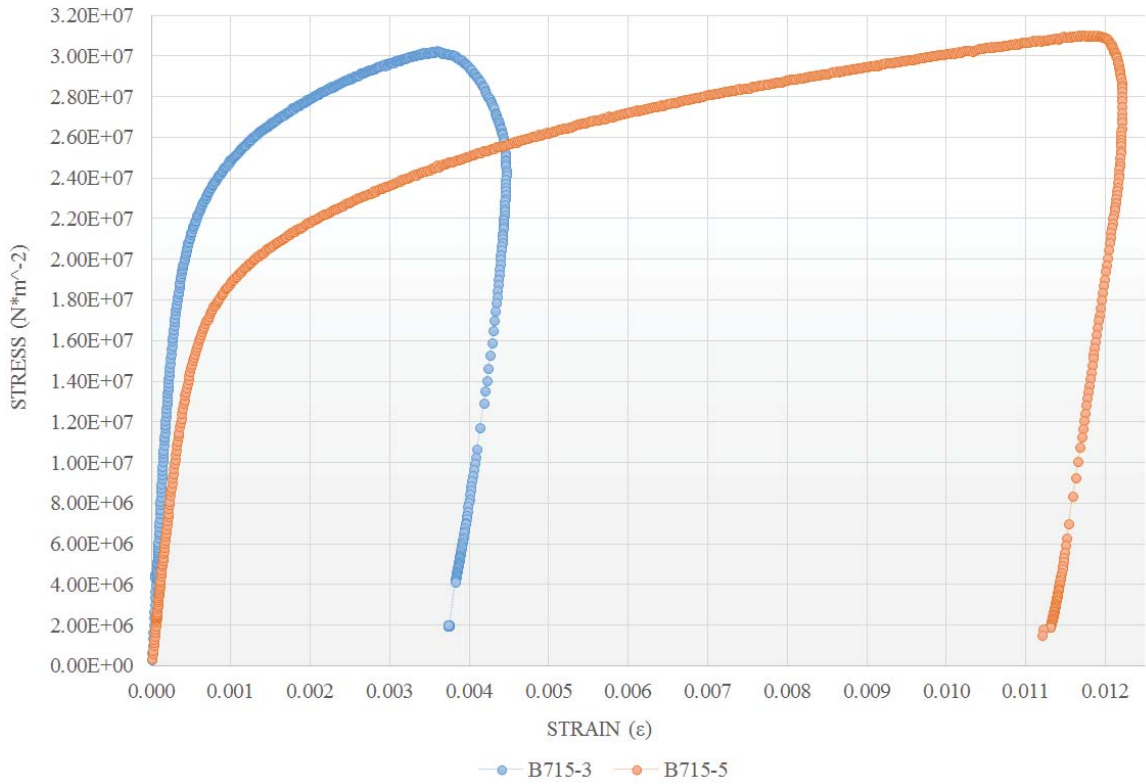
Figure 37: Batch715 Stress Strain Curve
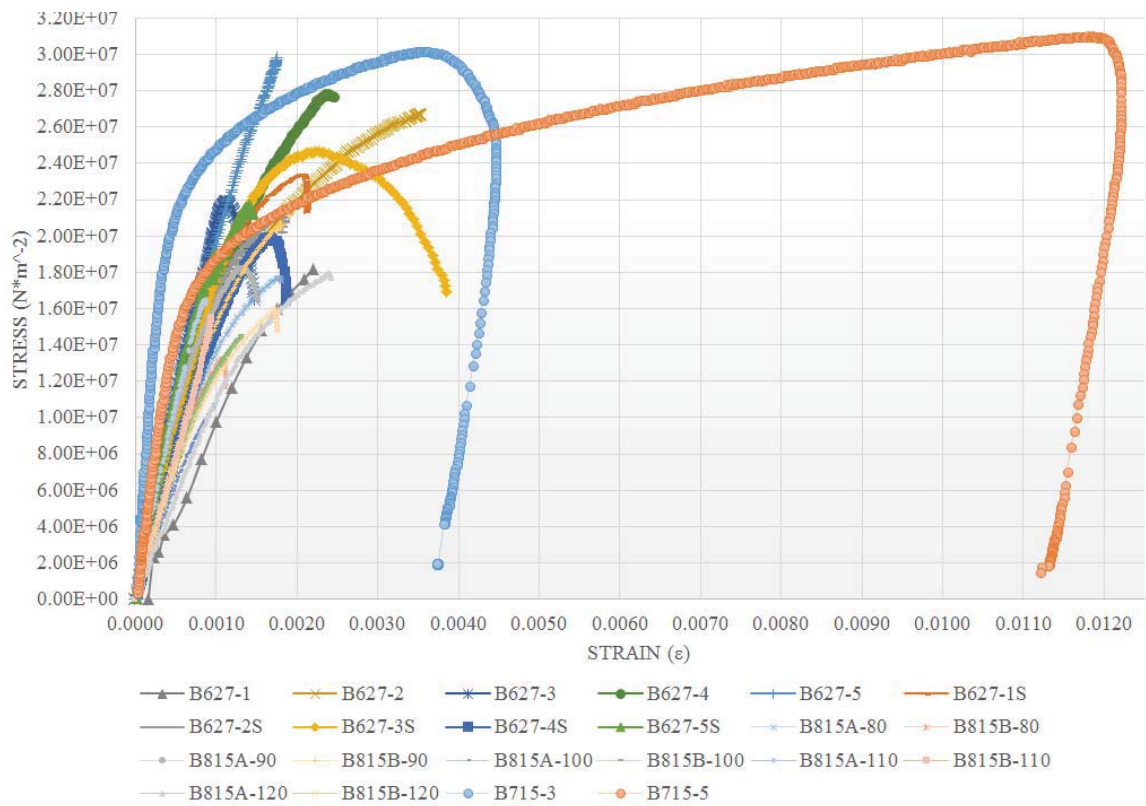
Figure 38: Stress Strain Curve Comparisons - All Specimens

Table 17 shows a comparison of all the specimen group average modulus of elasticities compared to bulk copper. Sintered B715 shows the closest results at a 54% difference from bulk copper modulus of elasticity. This difference is due to the lower densification of the additive manufactured parts. Table 18 shows a comparison of all the specimen group maximum tensile strength compared to bulk copper. Sintered B715 and the Batch627 printed flat orientation shows the closest results at a 88% difference from bulk copper tensile strength.

Table 17: Modulus of Elasticity Compared

Specimen Type	Modulus of Elasticity (N/m^2)	Different from Bulk Copper (N/m^2)	% Difference
Bulk Copper[8]	1.170E+11	0.000E+00	0%
B627, Printed Flat	1.940E+10	9.760E+10	83%
B627, Printed Edge-Built	2.059E+10	9.641E+10	82%
B815-80	1.586E+10	1.011E+11	86%
B815-90	1.923E+10	9.777E+10	84%
B815-100	1.446E+10	1.025E+11	88%
B815-110	1.875E+10	9.825E+10	84%
B815-120	1.278E+10	1.042E+11	89%
B715, Sintered	5.403E+10	6.297E+10	54%

Table 18: Maximum Strength Compared

Specimen Type	Maximum Strength (N/m^2)	Different from Bulk Copper (N/m^2)	% Difference
Bulk Copper (Annealed) [29]	2.100E+08	0.000E+00	0%
B627, Printed Flat	2.489E+07	1.851E+08	88%
B627, Printed Edge-Built	2.213E+07	1.879E+08	89%
B815-80	1.547E+07	1.945E+08	93%
B815-90	1.950E+07	1.905E+08	91%
B815-100	1.264E+07	1.974E+08	94%
B815-110	1.600E+07	1.940E+08	92%
B815-120	1.696E+07	1.930E+08	92%
B715, Sintered	2.524E+07	1.848E+08	88%

The density of the six additive manufactured copper parts was calculated by dividing the volume of the part by the cylinder of the part. Three of the parts were sintered, and three were not sintered. The diameter and length of the cylinders was measured and the volume was calculated. The AM cylinders were then weighted on a scale. The density of the non-sintered AM parts was found to be 66.5% of the density of bulk copper. The density of the sintered additive manufactured copper parts was increased to 68.9% of the density of bulk copper.

3.4 Leak Test of Additive Manufactured Water Blocks

Figure 39(a) shows the AM water block produced for the welding machine. The block print dimensions were 25.4 mm x 25.4 mm x 38.1 mm. A 5.6 mm diameter hole was printed through the block. Due to the print quality, the ends were machined flat. The 1/8 inch National Pipe Thread (NPT) ports were drilled into the surfaces centered on the holes. Figure 39(b) shows the final machined water block. The printed water block was cut using a carbide bit. During the machining process, the part was flooded with Master Chemical TRIM SOL® coolant. The water block was milled at 800 rpm and a 25.4 mm/min feed rate. When drilling the hole, the drill feed was 650 rpm.
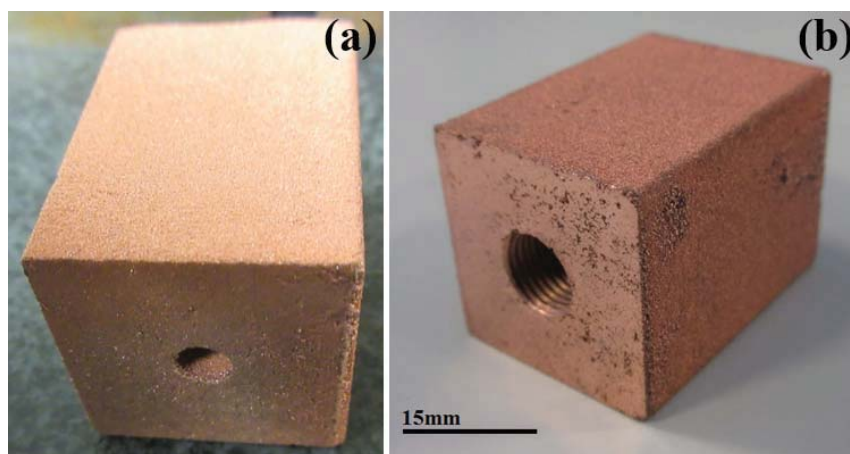
Figure 39: Printed Copper Block (a) Prior to Machining, (b) After Machining

Figure 40 shows the final test setup for leak test.
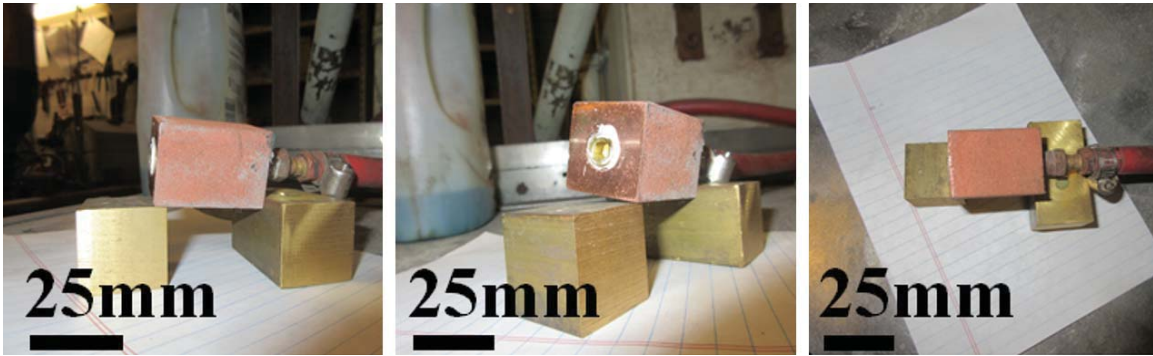
Figure 40: Leak Test Setup

The printed water block failed the leak test. After an exposure to the water of 4.5 seconds, water started to emerge from the sides of the block close to the plug, Figure 41 (a). At 4.6 seconds, the water emerged from the block's plugged face, Figure 41(b). At 4.7 seconds, Water emerged from the top of the block, Figure 41(c). By 5 and 6 seconds, the water was flowing out of all the printed water block surfaces, Figure 41(d) and (e).
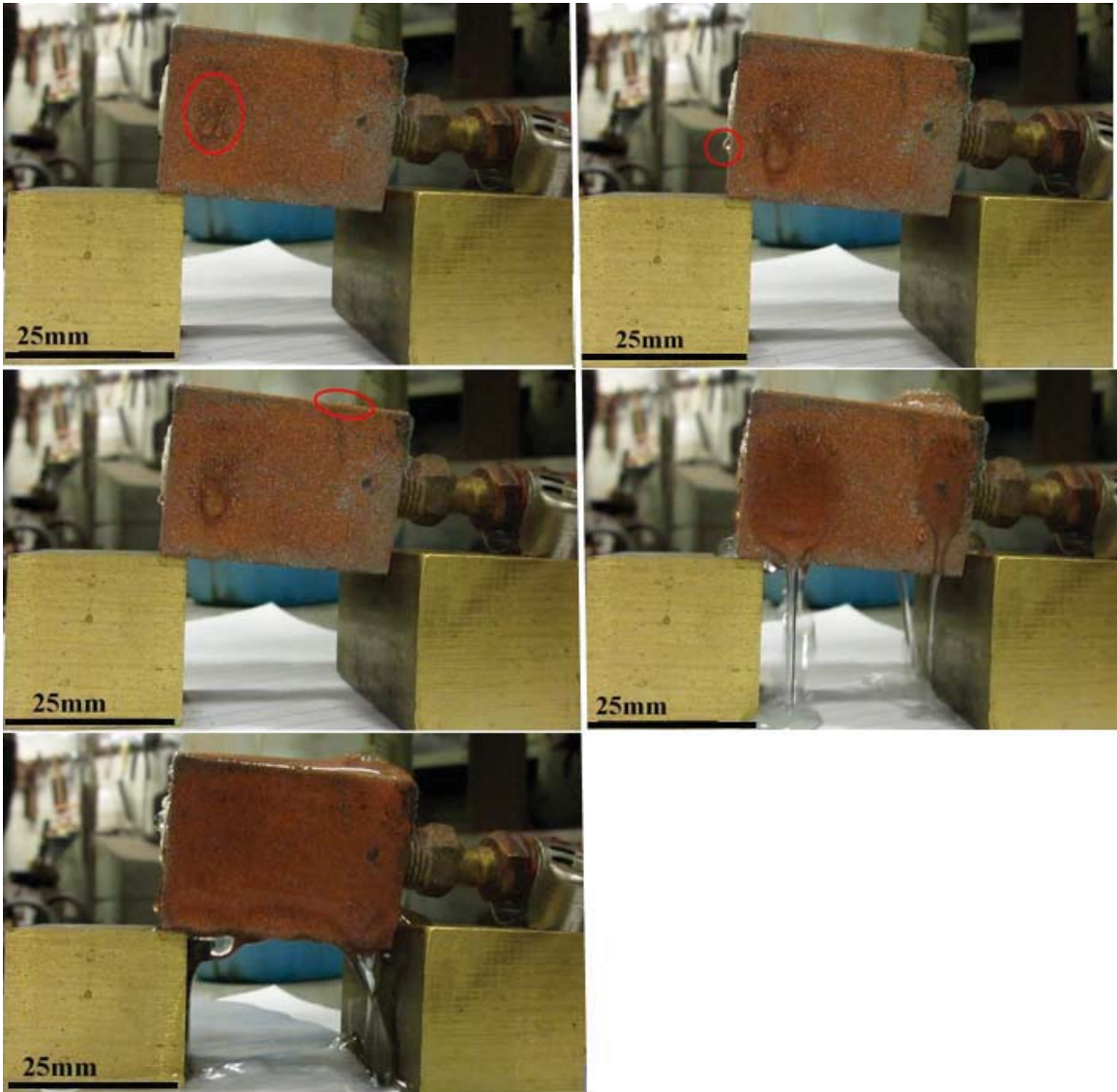
Figure 41: Water Test; (a) 4.5 s, (b) 4.6 s, (c) 4.7 s, (d) 5.0 s, and (e) 6.0 s

3.5 Electrical Resistance Welding Test

3.5.1 Additive Manufactured Electrodes and Electrode Adapters

Due to the high surface roughness of additive manufactured welder parts, machining was done in order to improve the surface finish of the electrode weld contact surfaces. The upper and lower electrode holders were printed without precise features, Figure 42(a) and Figure 43(a). These features were then machined into the parts prior to the weld tests, Figure 42(b) and Figure 43(b). The printed electrodes and electrode adapters were cut using carbide bits. During the machining process, the parts were flooded with Master Chemical TRIM SOL® coolant. The electrode adapters were milled at 900 rpm and a 25.4 mm/min feed rate. When drilling the hole, the drill feed was 900 rpm. Due to the softness of copper, stainless steel heli-coils were inserted into the part to prevent the threads from stripping.
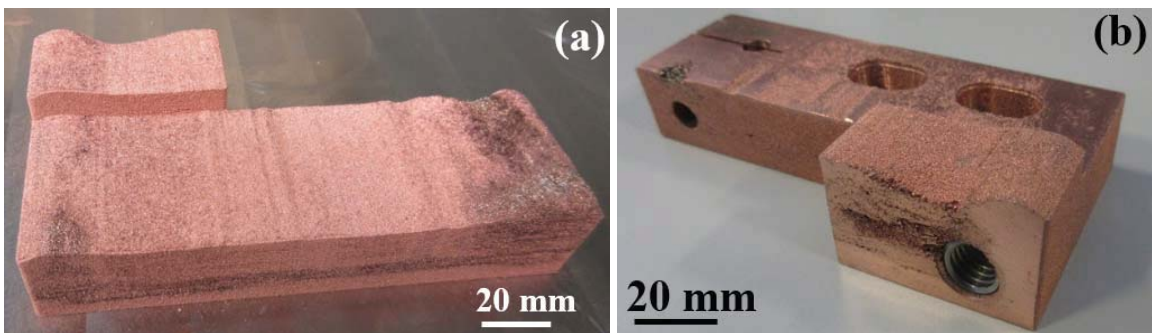
Figure 42: (a) Printed Upper Electrode Holder Prior to Machining, (b) After Machining
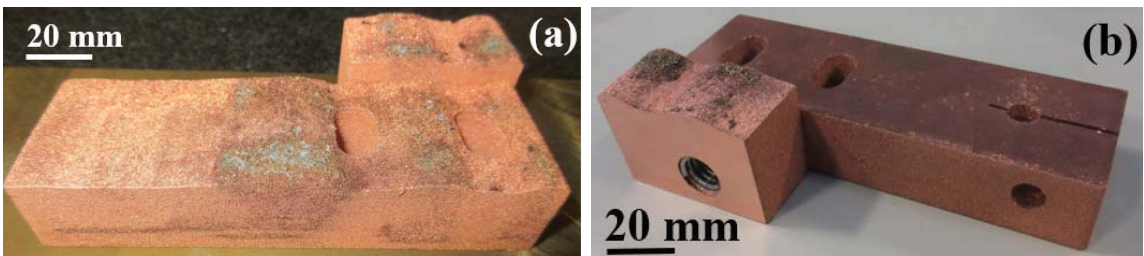
Figure 43: (a) Printed Lower Electrode Holder Prior to Machining, (b) After Machining

The cylindrical electrodes were printed with a diameter of 9.53 mm, Figure 44.
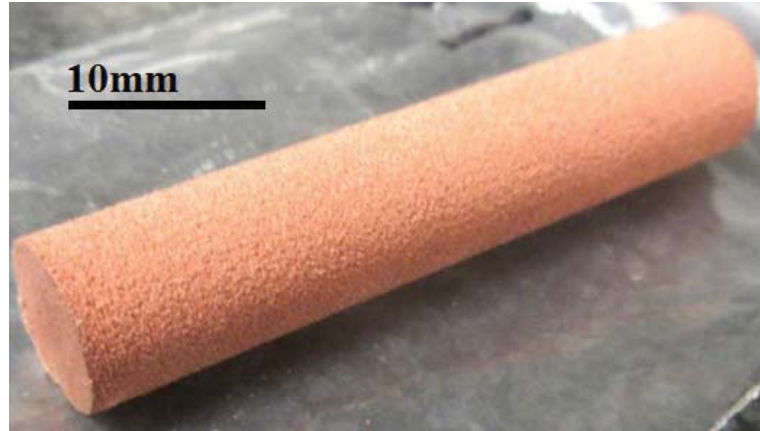
Figure 44: Printed Electrode Prior to Machining

The surface roughness of the printed electrodes pre-machining was 12.5 µm Ra. The necessary surface roughness for the welding circuit is 1.6 µm or less. The printed electrodes were machined in a lathe to the 1.6µm surface roughness. Due to the nature of the printed parts, iterations of machining parameters were completed to create an electrode with an acceptable surface finish and an additional end taper without bending or breaking off, as shown in Table 19. Between the 6th and 7th iteration, the electrode design was modified to reduce machining needed.

Table 19: Electrode Machining Iterations

		Cutter material	Cutter Radius (mm)	Lathe Rotation (RPM)	Cutter feed rate (mm/rev)	Coolant Duration	Result
Machining Iterations	1	Carbide	.762	1050	.508	None	Shattered at cutter contact
	2	Carbide	.762	1050	.508	Intermittent	Shattered at cutter contact
	3	Tool steel	.762	1050	.508	Continuous	Shattered after cutting 3.2mm off diameter
	4	Carbide	.762	530	.508	Continuous	Machined but bent
	5	Carbide	.762	530	.254	Continuous	Machined but bent
	6	Carbide	.381	530	.254	Continuous	Machined but bent
	7	Carbide	.381	530	.254	Continuous	Functional electrode with dimension modification

The final electrode design is as shown in Figure 45.
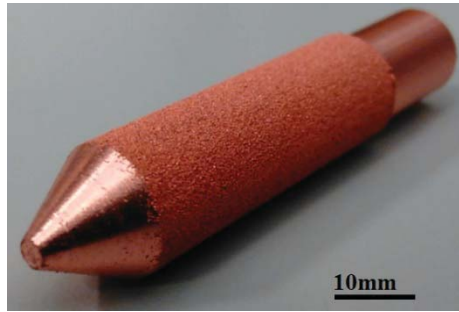
Figure 45: Post-Machined Finished Electrode

The additive manufactured parts were then assembled on the machine as shown in Figure 46. Jet-Lube SS-30 pure copper anti-seize lubricant was applied between the additive manufactured parts to avoid electrical arcs and sticking.

Figure 46: Printed Electrodes and Electrode Adapter on Welder

3.5.2 Weld Schedule Development

A weld schedule is a complete set of parameters that achieve a consistent, acceptable weld. A typical spot weld process is broken down into three time segments which are *squeeze time*, *weld time*, and *hold time*, shown in Figure 47. *Squeeze time* is the time from the moment the weld force is applied until the weld force stabilizes. A stable weld force

aides in the weld consistency. *Weld time* is the time that current is passed through the electrodes and workpieces. During this time, heat is generated and causes the interface of the workpieces to become molten and form the weld nugget. *Hold time* is the delay in releasing the weld force after the flow of current has ended. When the current is terminated, the heat generation is also terminated. However, molten metal may still exist. The hold time gives the molten weld nugget time to cool prior to releasing the weld force.
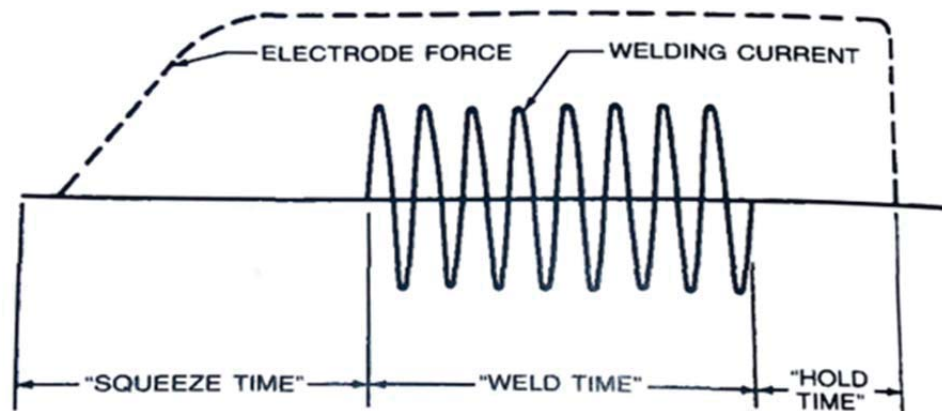
Figure 47: Resistance Spot Weld Cycle[3]

Another parameter of the weld schedule is the transformer wiring. Many transformers that are used in a resistance welding application have variable weld circuits that change the turn ratio within the transformer by turning a multiple position switch, also known as a "tap" switch. The tap switch allows different amounts of current to flow on the secondary circuit (weld circuit) depending on the "tap" selected. The Portage transformer used for this thesis was hardwired in the "L" or low tap with a tap switch from 1L to 8L. Tap 8L is the highest power output that the transformer can achieve.

Percent power is another weld schedule parameter that is determined by the weld control. For an AC (alternating current) transformer, current is output in sine waves. A weld

contact within the weld control dictates how much of the current from the sine wave is used, in percentages.

To set up the weld schedule for this project, the electrodes were aligned and were verified to have uniform contact. A typical weld schedule for low carbon steel with a thickness of .25 mm was selected based on tables located in the RWMA handbook. From this schedule, the parameters were refined for each individual weld system. In all resistance welding processes, there is a weld schedule operating range in which an acceptable weld can be created. If an operating range is too low, a weld nugget is unable to be created and the workpieces do not bond together. If an operating range is too high, it is possible that the weld can have expulsion. Expulsion is the process in which the molten nugget is propelled out from between the work pieces. This leaves voids and a partial weld nugget behind. There is also the chance that a weld nugget is not developed. Typically, the best weld schedule to utilize is one in the upper limits of the operating range. This allows the system to slightly deteriorate (i.e. electrodes mushrooming, workpieces becoming slightly dirty, or workpieces become slightly thicker than specifications) before a weld becomes unacceptable. To refine the welding process, sample workpieces were used to make a weld. The percent current power and transformer power level was slowly increased until a weld was created with some expulsion. The percent power was then lowered about 10%. At this point, a peel test was performed. A peel test is a commonly used as an acceptable weld test that requires very little equipment. A spot weld was made and one of the workpieces was clamped into a vise and was bent. The other piece was pulled with pliers until the destruction of the work pieces occurred, as shown in Figure 48. Once pulled apart, the weld button (weld nugget) was measured and the shape was observed.

The shape of the weld button should be round and should be similar in size when compared to the electrode tip.
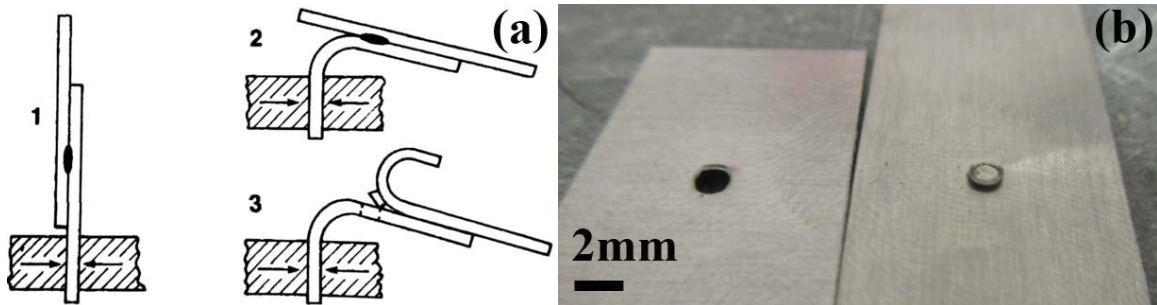
Figure 48: (a) Peel Test[3], (b) Peel Test with Acceptable Weld used in this Thesis

Irregular shaped weld buttons and "stuck" welds can be detected by a peel test. An irregular shaped weld is a weld that is any shape other than round. Irregular welds are usually caused by either electrode wear, misaligned electrodes, and/or insufficient weld energy. A "stuck" weld is a weak bond that is formed between the two workpieces with no weld nugget development. The bond is created by the localized fusion of the workpiece contact points and can be separated with light loads.[30] A stuck weld is caused by insufficient heat generation at the workpiece interface. Figure 49 shows an irregular and "stuck" weld.
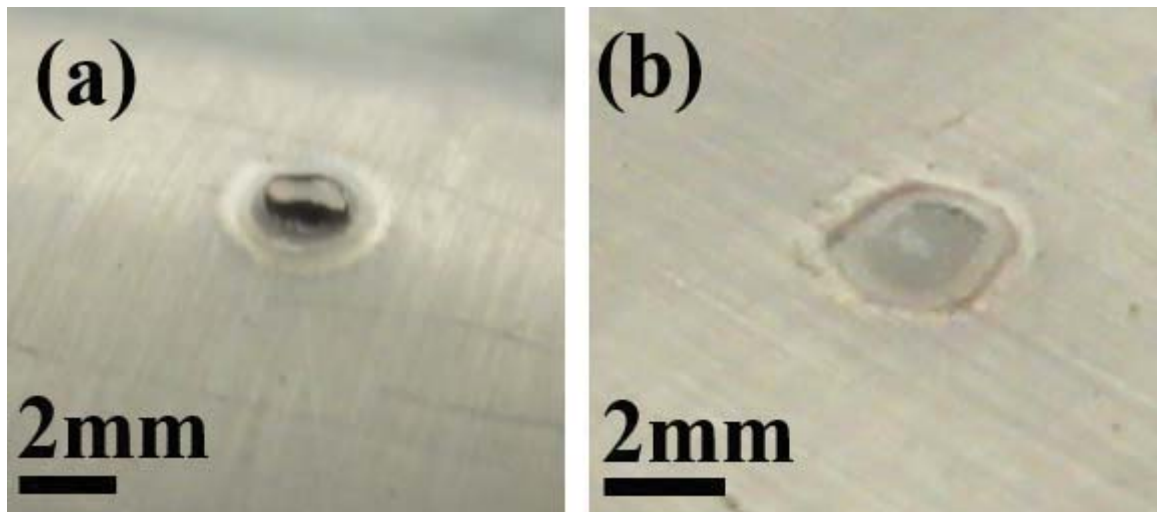
Figure 49: (a) Irregular Weld (from Group 5), (b) "Stuck" Weld (from Group 5)

Table 20 shows the developed weld schedules for each of the tests groups.

Table 20: Test Group Weld Schedules

Test Group	Weld Force (N)	Squeeze Time (cycles)	Weld Time (cycles)	Hold Time (cycles)	Transformer Tap	Percent Power
1	333.6	90	2	25	2L	75%
2	333.6	90	2	25	2L	75%
3	333.6	90	2	25	2L	75%
4	333.6	90	2	25	2L	90%
5	333.6	90	2	25	7L	80%
6	333.6	90	2	25	5L	80%

The weld schedule developed for Group 1 (conventional adapters with C110 electrodes) was used for Group 2 (conventional adapters with RWMA Class 2 electrodes) and Group 3 (additive manufactured adapters with RWMA Class 2 electrodes) to compare the group differences without adding a weld schedule change. A new weld schedule was created for Group 4 (additive manufactured adapters with RWMA Class 2 electrodes) to perform in the upper limit of the operating range. To achieve this, the percent power had to be increased from 75% to 90%. By going to 90%, Group 4 had the same current density that was observed in Groups 1 and 2. This increase of power was due to the increase in the electrical resistance of the AM adapter. It was discovered that more power was required to push the current through the secondary circuit with the additive manufactured parts. The increase in power was dissipated through heat generation throughout the secondary circuit. This increase of power grew exponentially in Groups 5 (additive manufactured adapters and electrodes) and 6 (additive manufactured adapters and electrodes, electrodes are sintered). Group 5 utilized tap 7L to perform the weld. At tap 7L, the transformer was outputting almost peak power to achieve the weld. In a production perspective, operating the transformer at peak capacity will cause the life of transformer to decrease. Group 6 utilized tap 5L. The lower tap was achieved due to the densification of the

sintered AM electrode which decreased the voids within the part. By reducing the number of voids, the material's bulk resistance was reduced. This reduces the power that is needed to push the current through the weld circuit.

3.5.3 Electrode Tip Wear

For this thesis, 120 welds were performed, 20 per weld group. After each weld group, the electrodes were redressed for the next weld group. After sets of ten welds, the electrode tips were redressed. As the welds were completed, all the electrode types, except for the RWMA Class 2 electrodes, showed signs of "mushrooming". Mushrooming is the process by which the electrode tip loses its shape and the surface contact area that interfaces with the workpiece increases. The mushrooming of the electrode's tip drastically affects the weld quality due to the reduced weld pressure and current density that is experienced because of this deformation. Although the force that is applied to the electrode is constant, the force is spread over a larger surface area, decreasing the pressure. As a result, the resistance at the electrode to workpiece area increased. This heated the electrode and caused it to mushroom further. Mushrooming decreases current density and gives the current a larger area to flow through the workpiece, resulting in a smaller weld nugget, as shown in Figure 50.
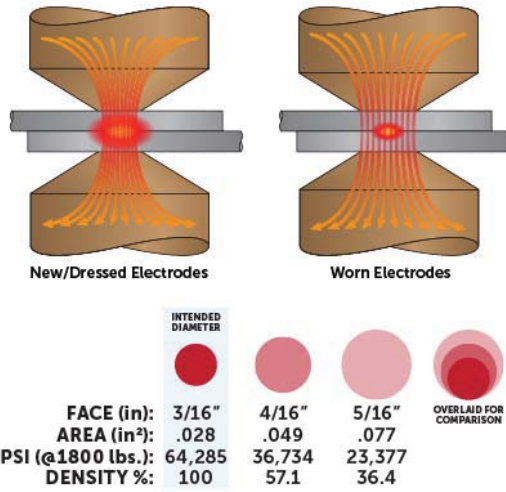
Figure 50: Current Density Deterioration from Electrode Wear Diagram[30]

Figure 51 and Table 21 shows the deterioration of the electrode tips and their effect on current density. As expected, the C110 electrodes and the AM electrodes (both sintered and non-sintered) displayed a similar slope to the electrode face deterioration.
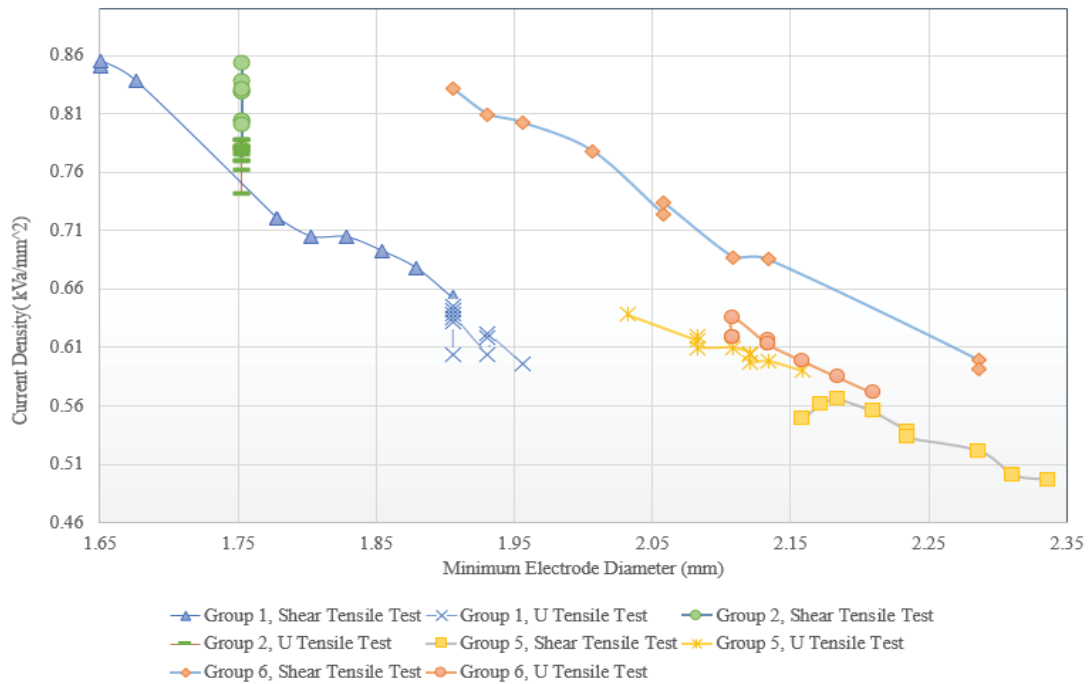
Figure 51: Electrode Tip Wear vs Current Density

Figure 51 shows the current density of all groups 1, 2, 5 and 6. Group 2 shows the highest current density of all the groups. This is because Group 2 has RWMA Class 2

electrodes that show no wear of the electrode tips and all parts of the weld circuit are conventionally fabricated. Groups 3 and 4 also utilized the Class 2 electrodes and show similar results to group 2 and therefore not shown in Figure 51. Group 5 current density drops lower than group 2 because of the additional heat generation in the additive manufacture electrode adapter reducing the current passed. By increasing the current power, group 6 current density increased from group 5. This proves the additional resistance from the porosity of the adapter causes the increased resistance.

Table 21: Current Density of All Samples

SAMPLE	CURRENT DENSITY (kVa/mm^2)					
	GROUP 1	GROUP 2	GROUP 3	GROUP 4	GROUP 5	GROUP 6
1	0.850	0.829	0.676	0.808	0.549	0.832
2	0.855	0.854	0.680	0.800	0.562	0.810
3	0.838	0.837	0.672	0.659	0.566	0.802
4	0.721	0.829	0.684	0.808	0.555	0.778
5	0.721	0.831	0.680	0.812	0.555	0.725
6	0.705	0.804	0.676	0.800	0.538	0.734
7	0.704	0.779	0.676	0.804	0.533	0.688
8	0.693	0.804	0.680	0.808	0.521	0.685
9	0.678	0.779	0.663	0.788	0.500	0.599
10	0.653	0.800	0.680	0.779	0.497	0.592
11	0.603	0.763	0.651	0.725	0.638	0.619
12	0.635	0.783	0.651	0.759	0.616	0.619
13	0.642	0.779	0.638	0.734	0.619	0.619
14	0.632	0.771	0.634	0.759	0.610	0.636
15	0.646	0.742	0.626	0.713	0.610	0.613
16	0.639	0.775	0.618	0.750	0.606	0.615
17	0.605	0.771	0.622	0.754	0.603	0.613
18	0.618	0.783	0.630	0.750	0.597	0.598
19	0.622	0.788	0.634	0.754	0.599	0.584
20	0.596	0.788	0.634	0.721	0.590	0.571
AVERAGE	0.683	0.795	0.655	0.764	0.573	0.667
Standard Deviation	0.081	0.029	0.024	0.041	0.041	0.084

For Groups 5 and 6, it was observed that a good amount of the additive manufactured electrodes bonded with the workpieces during the weld cycle. In mild cases, one electrode would form a weak bond to the workpiece before releasing. In severe cases, both electrodes formed a strong bond to the workpieces. Upon the weld cylinder retracting, the electrode tip would break off, as shown in Figure 52.
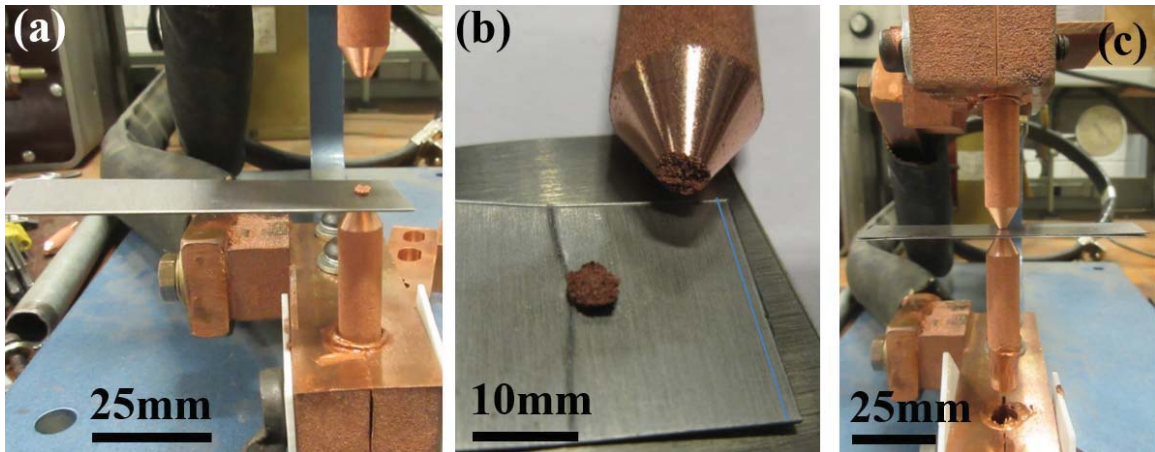
Figure 52: Damaged Electrode; (a) Bonded to Workpieces, (b) Closeup of Damaged Upper Electrode, and (c) Pulled Lower Electrode Out of Holder

This bonding was the result of porosity in the printed materials, which reduced the mechanical strength of the electrode. Figure 53 shows the normal resistance and temperature distribution in a typical spot welder. There is a minimal material bulk resistance (1 & 7), electrode to workpiece resistance (2 & 6), workpiece material bulk resistance (3 & 5), and the workpiece to workpiece resistance (4). The heat generated through the dissipated electrical power is calculated by:

$$H = I^2R \tag{3-1}$$

Where:

      H = heat generated

      I = current

      R = electrical resistance[3]
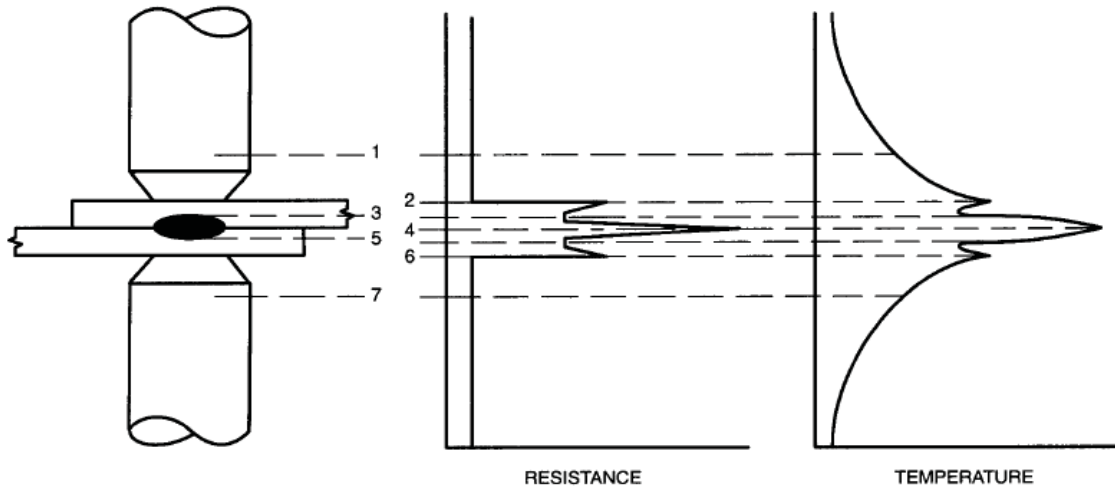
Figure 53: Resistance and Temperature Distribution between the Upper and Lower Electrodes[31]

In a balanced spot welding system, the workpiece to workpiece interface should have the largest resistance. This balance creates enough heat to form a molten weld nugget. After machining the electrodes, the inner pores are exposed to the surface. This increases the electrode to workpiece resistance. In the cases presented in Figure 52, the electrode to workpiece resistance was high enough to cause the printed copper electrode to melt and bond with the workpieces. This was a symptom of a poor-quality weld that was due to the resistant heat developing in areas other than between the two workpieces.[3]

3.5.4 Weld Mechanical Properties

Table 22 and Table 23 show the ultimate loads recorded at the pull tests.

Table 22: Ultimate Shear Tensile Force Compared from Shear Tensile Test

Sample Number	Ultimate Shear Tensile Force (N) *Stuck Weld – No Weld Nugget					
	Group 1	Group 2	Group 3	Group 4	Group 5	Group 6
1	994	1080	960	1077	1094	1236
2	1012	1081	961	1099	886*	1226
3	989	1053	972	1132	564*	750*
4	975	1026	963	1018	655*	963*
5	999	995	983	1064	619*	1210*
6	1036	1022	957	1109	611*	823*
7	995	1028	953	1047	696*	670*
8	1019	1040	973	1061	701*	812*
9	1039	1025	972	1079	749*	1073*
10	1022	1042	925	1080	606*	1103*
AVERAGE	1008	1039	962	1077	718	987
Standard Deviation	21	27	16	32	161	212

Table 23: Ultimate Tensile Force Compared from U Tensile Tests

Sample Number	Ultimate Tensile Force (N) *Stuck Weld – No Weld Nugget **Irregular Weld – Elongated or Significantly Smaller than the Electrode Tip					
	Group 1	Group 2	Group 3	Group 4	Group 5	Group 6
1	379	437	396	347	441	417
2	415	514	423	372	217**	342**
3	456	495	355	352	343**	265**
4	456	396	238	421	415	204**
5	386	344	315	474	356	184*
6	422	448	349	452	381	98*
7	394	496	346	393	403	51*
8	442	409	341	384	115*	42*
9	398	423	373	349	342	34*
10	430	325	373	314	337	89*
AVERAGE	418	429	351	386	335	173
Standard Deviation	28	63	50	50	98	134

As expected, control Groups 1 and 2 were similar in their averages. This proved that the difference from switching from C110 to RWMA Class 2 had very little effect on the properties of the weld itself. Group 3 did not perform as well as Groups 1 and 2. The ultimate force dropped 5% to 7% in the shear tensile tests and 16% to 18% in the pure

tensile test. The porosity of the adapter caused some heat to be generated in the adapter rather than between the workpieces. This reduced the strength of the weld. This was also verified with Group 4. A new weld schedule was attempted. With this new schedule, the extra power helped the heat generated at the weld to be equivalent to Groups 1 and 2. With Group 4, the extra power was still lost through heat generation within the adapter. As shown in the tables, most of the welds in Group 5 and 6 were either stuck welds with no weld nugget or irregular welds. The few acceptable welds in Groups 5 and 6 were comparable to the control Groups 1 and 2.

Table 24 shows all the weld diameters of the samples. Groups 5 and 6 experience irregular welds and "stuck" welds. This is due to the increase heat generation away from the workpiece interface causing only a small to no weld nugget to be formed.

Table 24: Weld Diameter of All Samples

SAMPLE	Weld Diameter (mm) *Stuck Weld – No Weld Nugget **Irregular Weld – Elongated or Significantly Smaller than the Electrode Tip					
	GROUP 1	GROUP 2	GROUP 3	GROUP 4	GROUP 5	GROUP 6
1	1.84	1.39	1.85	1.94	1.28	1.53
2	1.94	1.47	1.53	2.01	0.00*	1.72
3	1.80	1.34	1.91	1.85	0.00*	0.00*
4	2.02	1.48	1.79	2.03	0.00*	0.00*
5	2.00	1.53	1.55	2.09	0.00*	0.00*
6	1.91	1.32	1.73	1.94	0.00*	0.00*
7	1.88	1.68	1.88	2.05	0.00*	0.00*
8	1.87	1.50	1.63	1.99	0.00*	0.00*
9	1.69	1.53	1.87	2.10	0.00*	0.00*
10	1.93	1.99	1.65	2.00	0.00*	0.00*
11	1.65	1.32	1.42	1.51	1.30	1.60
12	1.66	1.41	1.30	1.75	0.48**	0.87**
13	1.57	1.43	1.37	1.61	0.64**	0.36**
14	1.57	1.44	1.19	1.68	1.13	0.37**
15	1.56	1.37	1.27	1.59	1.20	0.11
16	1.63	1.44	1.24	1.55	1.26	0.00*
17	1.62	1.43	1.22	1.61	1.13	0.00*
18	1.53	1.43	1.16	1.52	0.00*	0.00*
19	1.55	1.50	1.23	1.47	1.39	0.00*
20	1.54	1.61	1.33	1.47	1.39	0.00*
AVERAGE	1.74	1.48	1.51	1.79	0.56	0.33
Standard Deviation	0.17	0.15	0.26	0.23	0.61	0.60

Based on the tests, AM electrodes made in the present work proved to not be a viable option for production due to the inconsistency of the weld quality and ultimate force. By using a higher power laser to produce AM copper parts at almost 100% density will probably increase the consistency of the weld quality and the ultimate force. These conditions can improve the chances of utilizing AM in industry production.

3.6 Flow Simulation of Cooling Water Path Optimization in an Electrode/Electrode Adapter Body System

In resistance spot welding, one of the critical components of electrode life expectancy is optimizing the heat transfer coefficient of the electrode. Electrode and electrode adapters contain water flow paths that allow heat to transfer away from the electrode, keeping the electrode at a reasonable temperature. In this chapter, the internal geometry of the electrode/electrode adapter water flow path will be analyzed with the purpose of optimizing the electrode heat transfer.

Resistance spot welding is a welding process in which electrical current is applied to a circuit of electrodes and workpieces to be welded. The contact resistance is highest at the workpiece interfaces and causes Joule heat. The Joule heat melts the work piece interface and creates a weld nugget. Excess heat from the interfaces is also transferred into the electrodes. Figure 54 shows that heat is transferred by means of conduction, radiation, and convection.
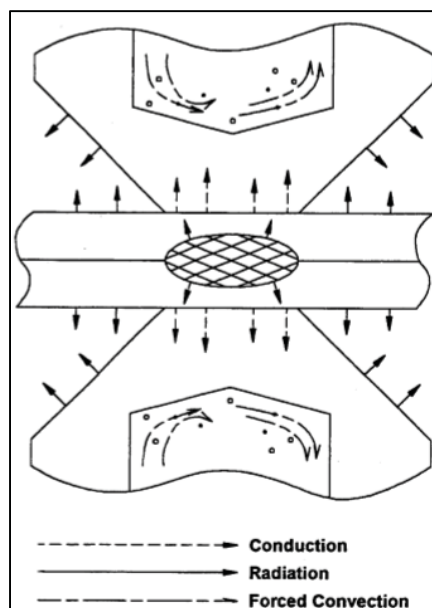

Figure 54: Heat Transfer in Resistance Welding[32]

As stated in Chapter 1.1, electrode geometry is crucial to producing acceptable welds. Electrodes that accrue enough heat will deform under the weld force and change the electrical current distribution. To extend the electrode life, cooling must be provided to transfer heat away from the electrode. A typical water cooling path of a resistance spot weld electrode and adapter is shown in Figure 55.
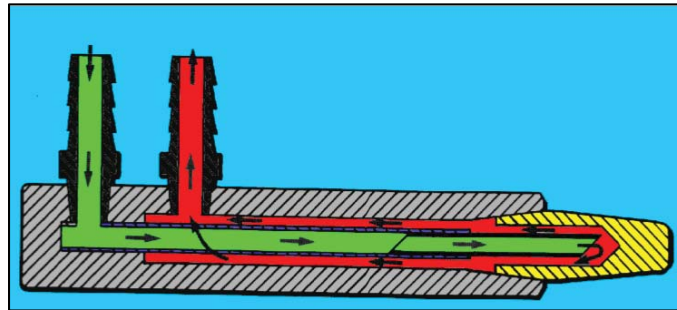
Figure 55: Typical Electrode and Electrode Adapter Cooling Path[32]

Lai *et al*[33] looked at optimizing a spherical shaped electrode cooling efficiency by optimizing the variable of the cooling path inside the electrode. Three parameters that were considered are the cooling pipe height, the velocity of the cooling water, and the diameter of the cooling pipe, as shown in Figure 56. The optimization was based on the cooling rate equation:

$$c_r = \frac{T_{max}}{T_i} \tag{3-2}$$

Where:

c_r = cooling rate

T_{max} = maximum temperature of the electrode

T_i = initial temperature of the electrode

Figure 56: Electrode Optimization Parameters

Lai *et al*[33] observed an optimization of parameters in their study of the electrode water

system, shown in Table 25. These parameters were calculated through Ansys Simulation

and the non-linear polynomial method and were proved accurate with experimentation.
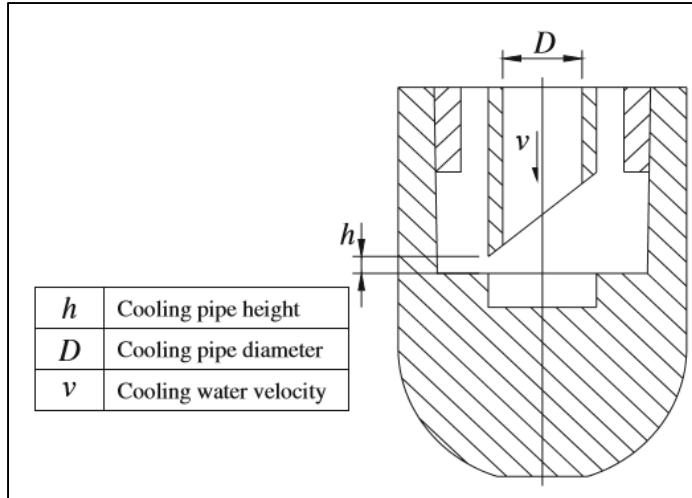
Table 25: Optimized Electrode Parameters

Optimized Cooling Parameter	Value
Cooling Pipe Diameter (mm)	4.32
Cooling Water Velocity (m/s)	14.34
Cooling Pipe Height (mm)	1.00
Cooling Rate	2.340276

The researchers used only a small portion of the cooling system geometry to find the

optimized values in their paper. They also assumed that the incoming flow was laminar.

In this analysis, a larger portion of the electrode cooling system's geometry has been

modeled and a turbulence incoming flow was assumed. The optimization results of the

expanded internal geometry and turbulence of the model will be compared to Lai *et al*[33].

Similar geometry to Lai *et al*[33] was used. The height of the cooling tube was studied at 1

mm and 3 mm.

For this analysis, the weld cycle in the model was 10 seconds long and consisted of one (1) second of welding and nine (9) seconds of rest. Lai *et al*[33] determined that the heat that was generated by the welding process that was transferred to the electrode was 5,000,000 W/m^2. The model simulation was transient simulation and ran for five (5) consecutive welds cycles.

Items that were monitored and compared to Lai *et al*[33] (where applicable):

- Maximum temperature of the electrode over time

- Maximum temperature of the water outlet over time

- Heat flux of the system over time

For the 1 mm cooling pipe height model only, a convergence of grid space and time step were completed to verify that the model converged to a single solution. The grid space convergence test was performed by applying a grid space and running the model. Two successively finer grids were then chosen and the model was run again. The models then needed to be compared. If the comparison showed less than a 2% difference, the grid space is said to converge. Time step convergence is a similar process. The percent difference for the time step and grid space is calculated two different ways. The time step convergence is calculated by:

$$Difference \%_{time} = \frac{|t_{bigger\ time\ step} - t_{smaller\ time\ step}|}{|t_{exact}|} \tag{3-3}$$

Where:

t = the time to reach a certain temperature or to reach steady state at a chosen time step.

t_{exact} = the exact time the calculation takes to reach a certain temperature or to reach steady state. When this is not known, the time of the smaller time step is used.

Percent difference for grid space is calculated by:

$$Difference \%_{grid} = \frac{|T_{bigger\ grid@position\ X} - T_{smaller\ grid@position\ X}|}{|T_{initial@X} - T_{final@X}|} \qquad (3\text{-}4)$$

Unlike time step percent difference, this percent difference is based on the change in temperature throughout the simulation and not the exact temperature. This is because inaccuracies can be found depending on the units that are used for calculations.

The model geometry was closely drawn to resemble the model in the reference paper of Lai *et al*[33]. The model encompasses more of the piping associated with a "real world" situation. The model is an internal flow model to evaluate the efficiency of the cooling presented at the different cooling pipe heights. The model introduces more flow factors not seen by Lai *et al*[33]. The goal of this analysis was to prove both the optimization that was found in Lai *et al*[33], as well as its accuracy when analyzing a larger part of the cooling system.

The geometry from Lai *et al*[33] is shown in Figure 57 and geometrical parameters are provided in Table 26. The Lai *et al*[33] model only focuses on the electrode and water path near the electrode.
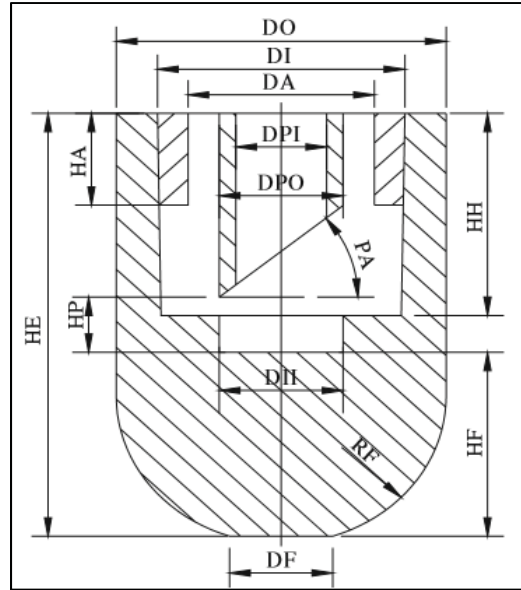
Figure 57: Lai *et al*[33] Dimensional Diagram of the Electrode

Table 26: Lai *et al*[33] Geometry Parameter Values

Parameter	Value	Parameter	Value
DPI	4.32 mm	HE	23 mm
DPO	6 mm	HF	10 mm
DI	12 mm	HP	3 mm
DO	16 mm	HH	11 mm
DII	6 mm	HA	5 mm
DF	5 mm	PA	30°
DA	9 mm	RF	16 mm

The analysis model geometry matches the Lai *et al*[33] model geometry in the lower region of the electrode. In this work, the model was expanded to the flow of the whole electrode adapter-electrode system shown in Figure 58. The inlet and outlet were 6.35 mm in diameter and were placed 25.4 mm away from the center of the cooling tube. The inlet and outlet tubes were 31.75 mm apart from each other and were 76.20 mm from the bottom of the cooling water cavity.
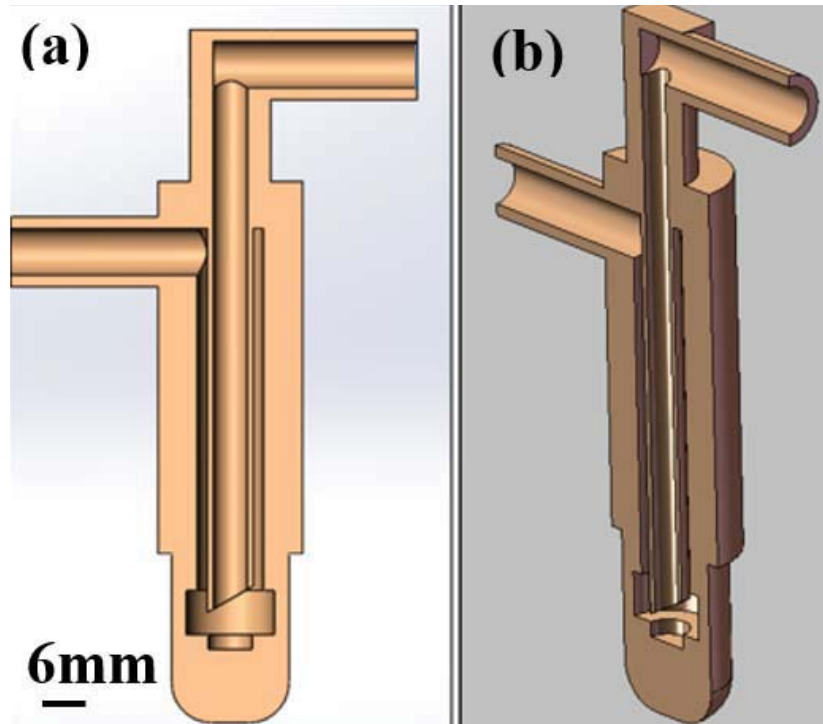
Figure 58: Model Cross-Section, (a) Front View, (b) Isometric View

Two versions of the geometry are presented. The cooling pipe diameter was set at a constant diameter of 4.32 mm. The cooling pipe height was varied at 1 mm and 3 mm as shown in Figure 59.
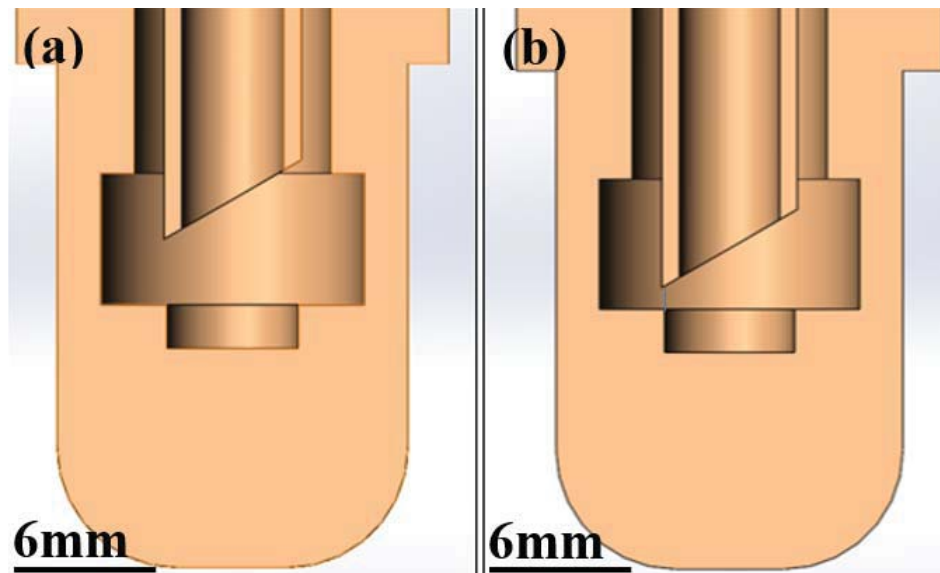

Figure 59: Electrode Models for Analysis with Varying Cooling Pipe Heights, (a) 3 mm, (b) 1 mm

The model was created out of one solid body. Being the same material, both the electrode and the electrode adapter were modeled as one part to simplify the analysis model. The hollow solid body represented the copper electrode and the electrode adapter. The internal chamber represented the cooling water path. To use the SFS internal flow analysis, the model's orifices were closed. The lid feature was utilized on the inlet and outlet orifices to close the model. These lid features were also used to apply boundary conditions for the simulation.

Next the project was saved. 'SI' units were selected for the simulation. This selection did not scale the model, but rather applied the SI units (m-kg-s-K) to the input values. The analysis type was selected as 'Internal'. The model's physical feature of 'heat conduction in solids' was turned 'on'. Time dependent analysis for a total analysis time of 60 seconds was indicated (5 weld cycles with an additional 9 seconds of cool down time). A transient type of analysis was chosen to more accurately simulate the real situation. Heat produced by the weld was a cyclical value and was not constant. Therefore, the heat flux as well as the water outlet and the maximum temperature changed with time.

A gravity value of -9.81 m/s^2 in the "Y" direction was entered. The default fluid was selected as water with a flow type of both laminar and turbulent characteristics. Cavitation was left at the default value of "off". The default solid was selected as copper. The default outer wall thermal condition was selected as 'adiabatic wall' with a roughness of 0 μm. Adiabatic wall was selected because the simulation was focusing only on the results from the internal flow of the system.

The initial conditions were selected. These are shown in Table 27.

Table 27: Initial Conditions from SFS

Thermodynamic parameters	Static Pressure: 101325.00 Pa
	Temperature: 300.00 K
Velocity parameters	Velocity vector
	Velocity in X direction: 0 m/s
	Velocity in Y direction: 0 m/s
	Velocity in Z direction: 0 m/s
Solid parameters	Default material: Copper
	Initial solid temperature: 300.00 K
	Radiation Transparency: Opaque
Turbulence parameters	Turbulence intensity 2%
	Turbulence length .00019886 m

SFS has a material library of both fluids and solids. Our fluid is water and the solid model

is copper. These properties vary with temperature and are presented below in Table 28

and Figure 60 through Figure 63.

Table 28: Constant Water Properties used by Lai *et al*[33]

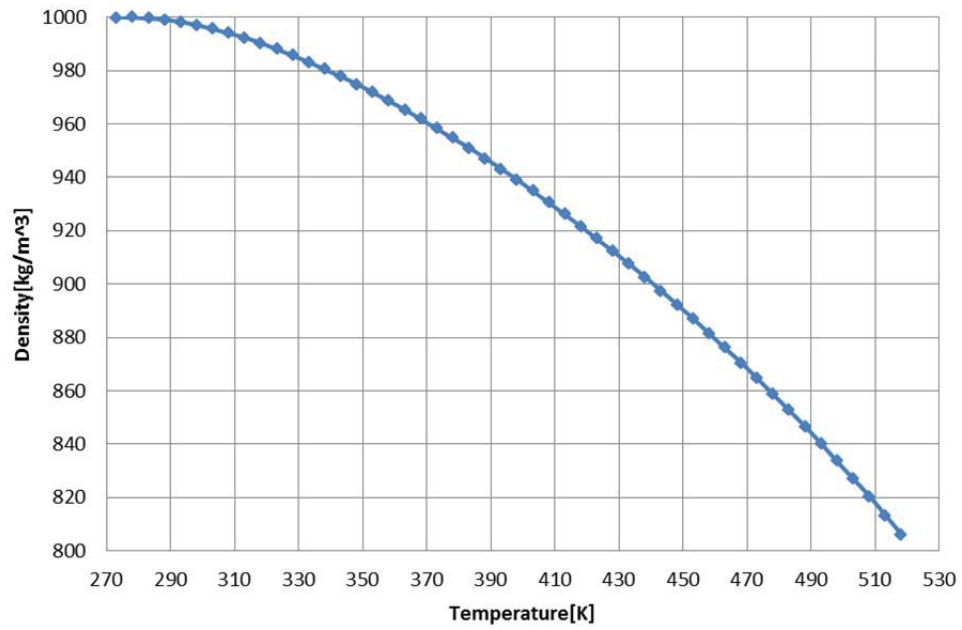| Parameter	Value
Water Density (kg/m^3)	988.3
Water Dynamic Viscosity (kg/m*s)	.001
Water Thermal Conductivity (W/m*K)	.5996
Water Specific Heat Capacity (J/kg*K)	4182
Copper Density (kg/m^3)	8960
Copper Conductivity Type	Isotropic
Melting Temperature (K)	1356.20

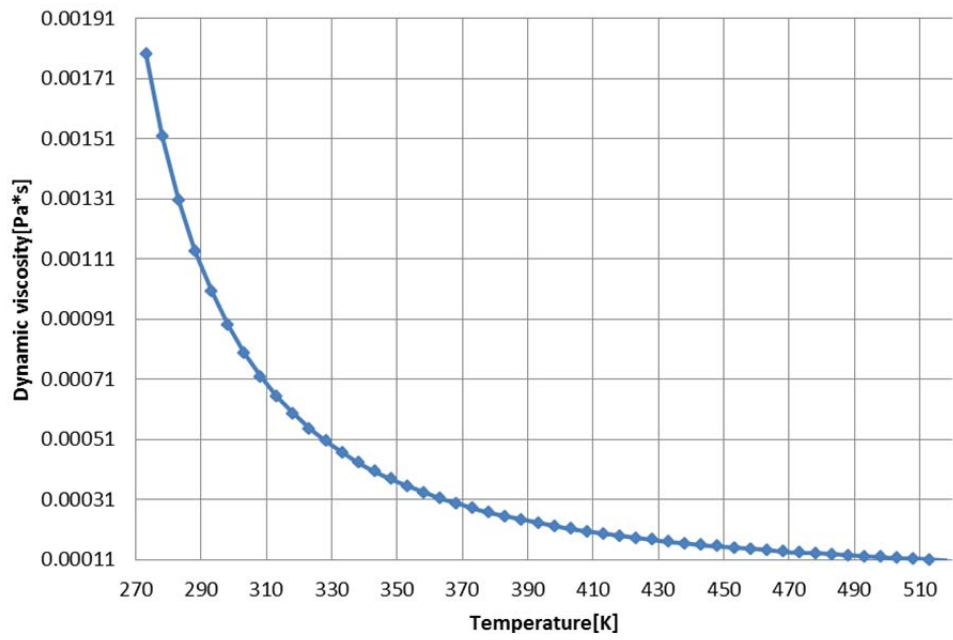Figure 60: Density of Water

Figure 61: Dynamic Viscosity of Water

Figure 62: Specific Heat of Copper

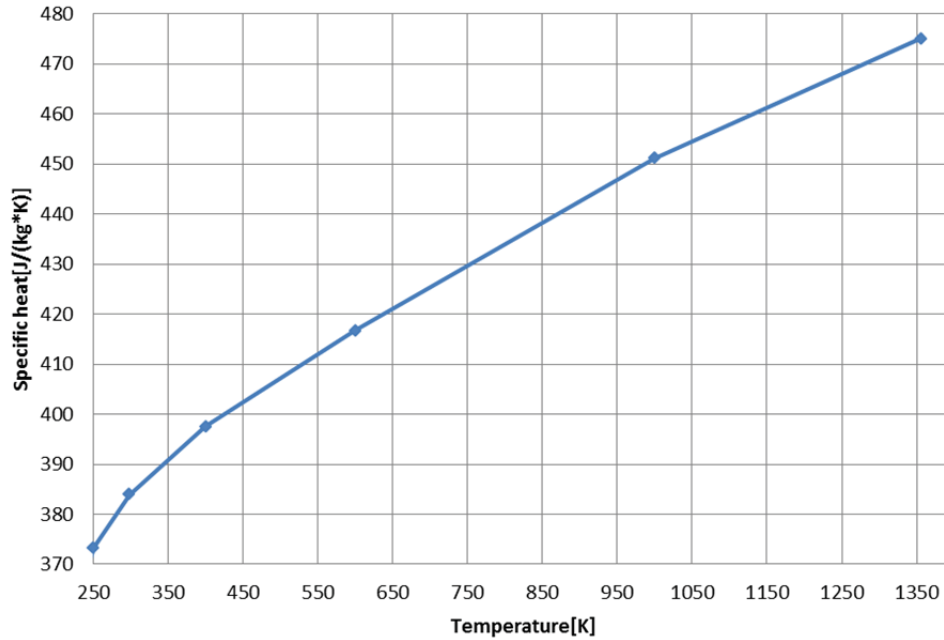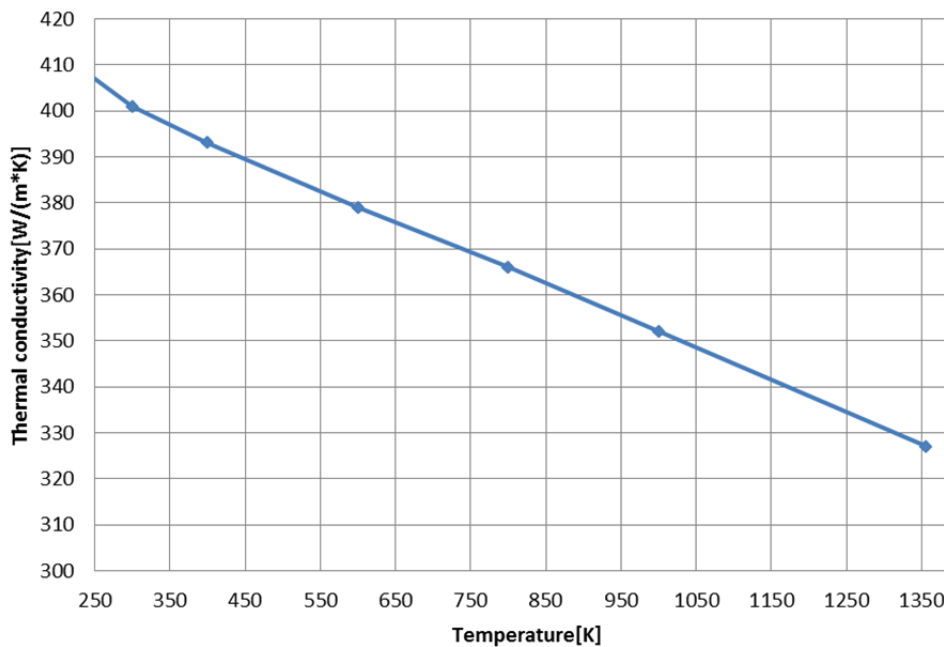Figure 63: Thermal Conductivity of Copper

The results and geometry resolution were chosen next. A result resolution of five (5) was chosen for all configurations. This made all calculated values converge to a 10^{-5} value before going to the next iteration of the simulation. A manual minimum gap size of 1.55 mm was chosen. This corresponded to the flow channel gap around the internal pipe. A

85

minimum wall thickness was entered as 0.821mm. This corresponded to the wall of the internal pipe. Both 'Advanced narrow channel refinement', and 'Optimize thin wall resolution' was selected. When the narrow channel refinement was selected, the solver automatically created a mesh with at least 10 cells across each channel. Due to the symmetry of the model and its boundary conditions, only half of the model was necessary to compute the whole domain. The computational domain in the "Z" direction was divided in half with a symmetry condition at the half way point, as shown in Figure 64.
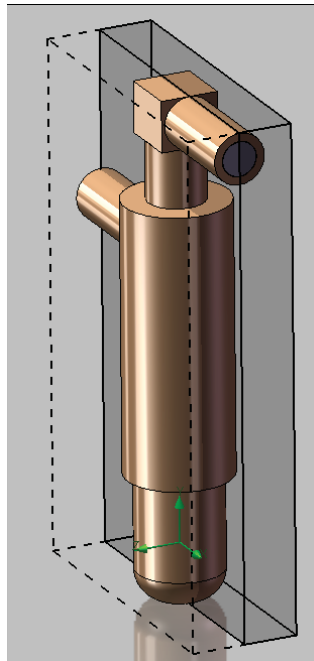
Figure 64: Computational Domain with Symmetry

Geometry was inspected to see if the internal domain was closed, the internal fluid volume was greater than zero, and that there were no invalid contacts (model point or line contacts) within the model. A fluid subdomain of 'water' was assigned to the internal chamber of the model. The solid material of 'copper' was assigned to the model itself. Boundary conditions were then applied to the model. These are shown in Table 29 and

Figure 65. Due to the change in diameter, the continuity equation was utilized to find the inlet velocity to keep the flow rate the same as Lai *et al*[33]. the continuity equation is:

$$\rho * A_1 * V_1 = \rho * A_2 * V_2 \tag{3-5}$$

Where:

A_x = cross-sectional area of pipe at position "x"

V_x = flow velocity at position "x"

ρ = density of fluid

For this velocity calculation, the density s assumed to be constant. The velocity at the inlet is calculated to be 6.637 m/s. Figure 66 shows the heat generation toggle over time. The heat generation is "On" at state 1 and "Off" at state 0.

Table 29: Boundary Conditions

| Boundary Surface Name	Type	Values
Water Inlet	Flow Openings – Inlet Velocity Flow	Velocity =6.637 m/s Temperature = 300 K
Water Outlet	Pressure Openings – Static Pressure	This selection acts similar to an outflow condition in ANSYS Fluent. No value needs entered.
Electrode Heated Surface	Heat Source – Surface Heat Source	5 x10^7 W/m^2 To toggle on and off as shown in Figure 66
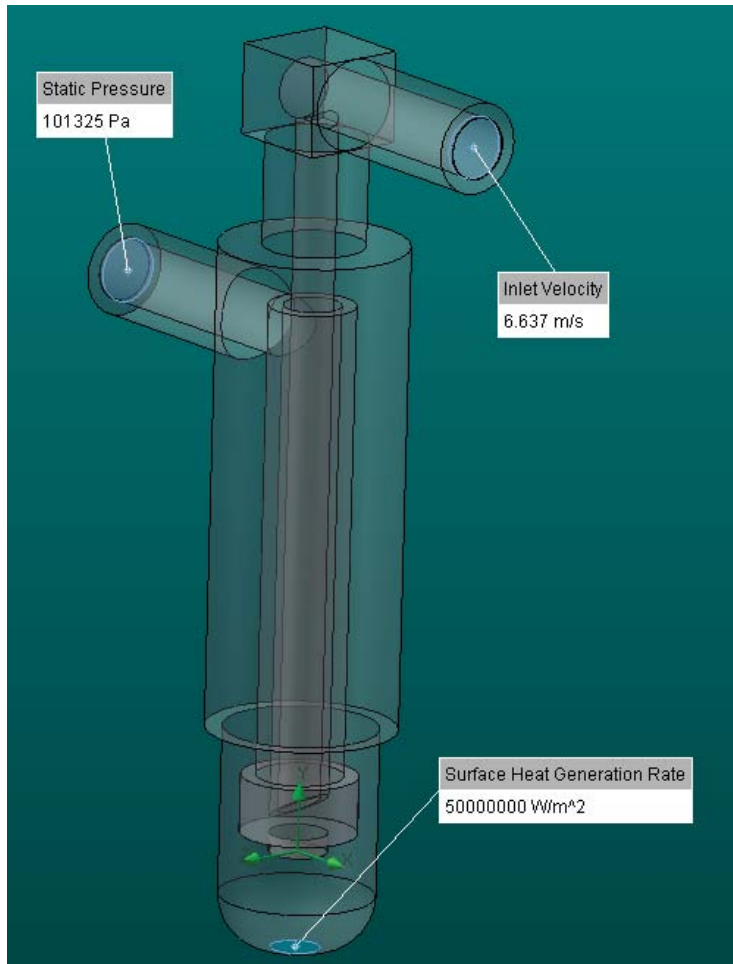
Figure 65: Model with Boundary Conditions
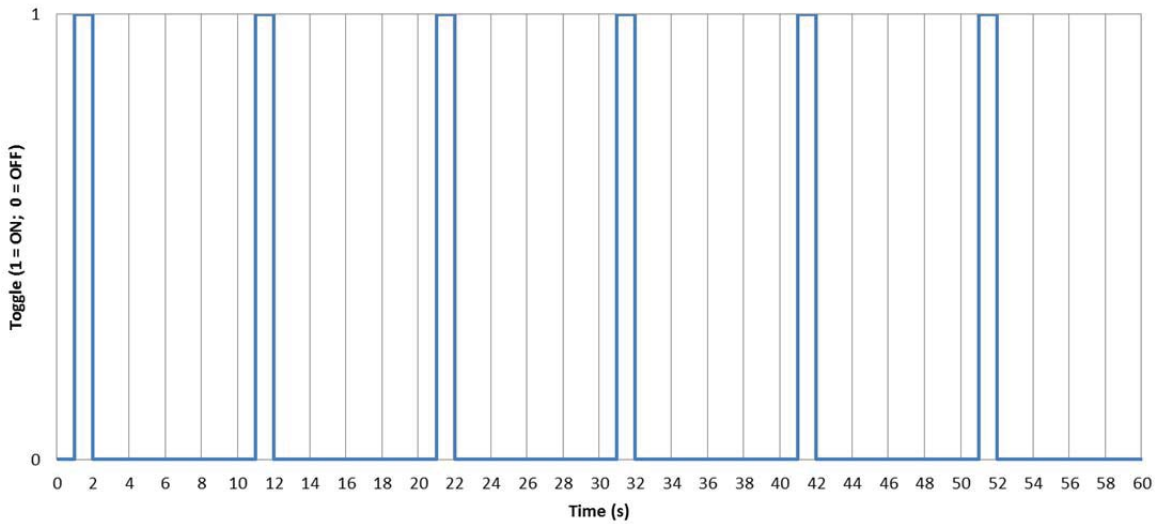
Figure 66: Surface Heat Generation Rate Toggle

SFS contains build-in convergence criteria. Engineering goals are physical parameters of interest that a user can display while the solver is running. These goals will also make the solver specifically converge these criteria along with its own built-in criteria. The goals selected for this simulation are shown in Table 30.

Table 30: Engineering Goals

Engineering Goal Name	Goal Type	Values to be Converged
Heat Flux	Global	Average Maximum
Heat Transfer Rate	Global	Maximum
Temperature (Solid)	Global	Average Maximum
Velocity	Global	Average Maximum
Temperature (Fluid)	Global	Average Maximum
Temperature	Surface (outlet lid)	Average Maximum
Velocity	Surface (outlet lid)	Average Maximum

SFS automatically computes an initial 'basic mesh' based on the geometry of the model, the minimum gap size, the minimum wall thickness, and the options selected ('Advanced narrow channel refinement' and/or 'Optimize thin wall resolution'). This is shown in Figure 67. For this model, the computational domain was split into 40 cells in the 'X' direction, 68 cells in the 'Y' direction, and 7 cells in the 'Z' direction.
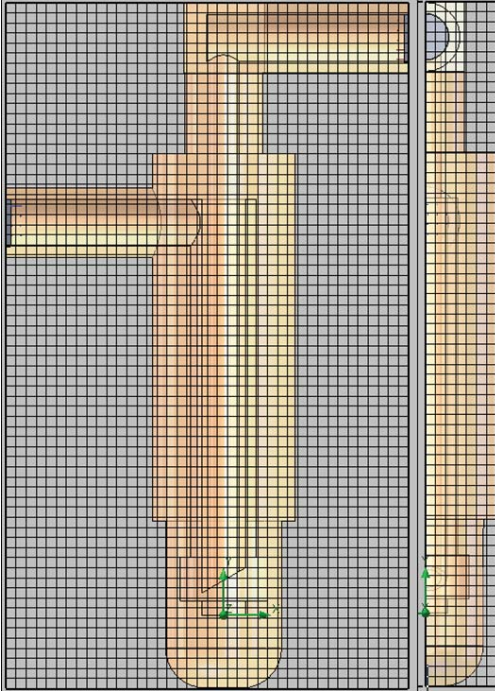
Figure 67: Basic SFS Mesh

Notice in Figure 67 that the mesh can have both a fluid and a solid in the same mesh element. This was an advantage to SFS compared to Fluent. The solver continued to refine the meshes as the study ran. This is shown in Figure 68 through Figure 70.

Figure 68: Resolved Cross-Sectional Mesh

Figure 69: Resolved Mesh Overall
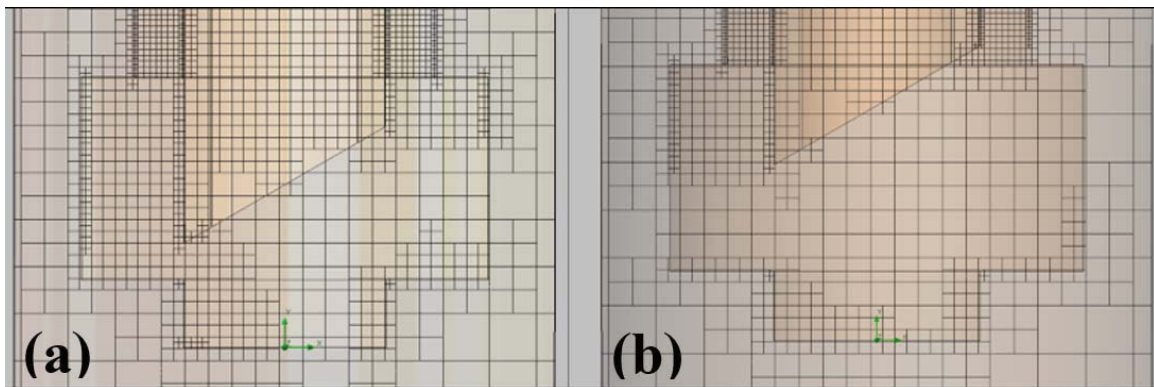
Figure 70: Resolved Mesh at Bottom of Water Chamber, (a) 1mm; (b) 3mm

Grid convergence was performed only on the region where the cooling water exited the

inner cooling water tube toward the electrode. To refine the mesh further in this location,

a new component was added to the initial model. This part was created in the shape and geometry of the lower electrode chamber. The mesh control part was added into the model assembly, shown in Figure 71.
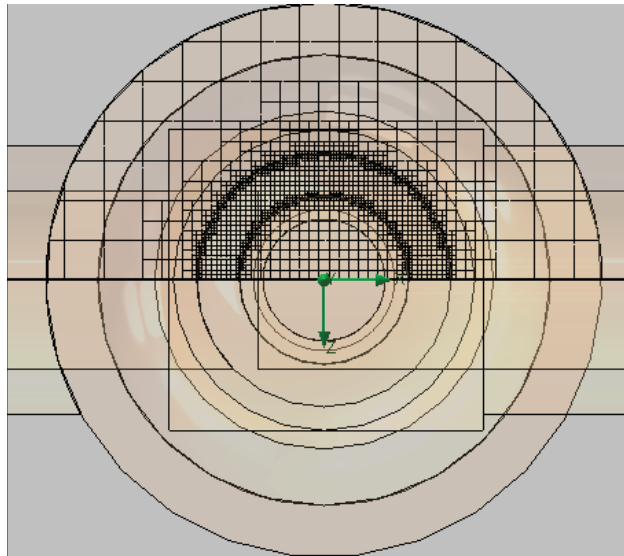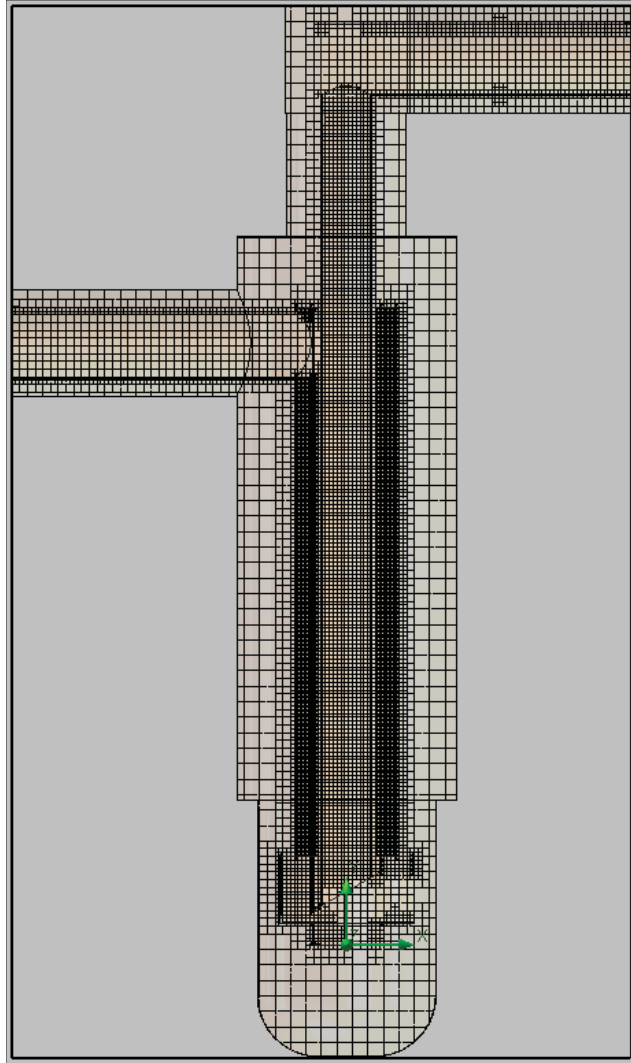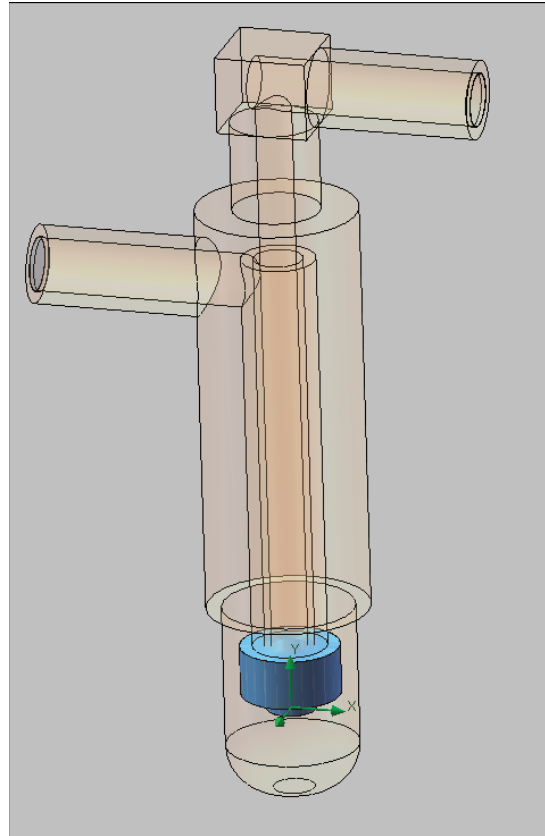

Figure 71: Mesh control Part (blue) in Assembly

In the component control feature, the mesh control part was 'disabled'. By disabling the component, the body would not be considered as part of the simulation model, but could have been used for local initial meshes. The initial located mesh was used to accurately resolve a feature of interest without the model's mesh splitting excessively. Next, the mesh control part was selected and an initial mesh was applied to the part. Automatic mesh controls were turned "off". All values selected in the medium and fine mesh for grid convergence are shown in Table 31. Figure 72 compares the meshes graphically.

Table 32 compares the mesh elements of the different refinements for the 1 mm model.

Table 33 compares the mesh elements of the different refinements for the 3 mm model.

Table 31: Mesh Setting Comparison

Mesh Setting	Course Mesh	Medium Mesh	Fine Mesh
Initial Mesh Automatic Setting	On	On	On
Initial Mesh Result Resolution Level	5	5	5
Initial Mesh Advanced Narrow Channel Refinement	On	On	On
Initial Mesh Refinement in Solid Region	Off	Off	Off
Local Initial Mesh Small Solid Features Refinement Level	N/A	1	2
Local Initial Mesh Curvature Refinement Level	N/A	1	2
Local Initial Mesh Curvature Refinement Criterion	N/A	0.505 rad	0.505 rad
Local Initial Mesh Tolerance Refinement Level	N/A	1	2
Local Initial Mesh Tolerance Refinement Criterion	N/A	2.053e-004 m	2.053e-004 m
Local Initial Mesh Refine Fluid Cells	N/A	On	On
Local Initial Mesh Level of Refining Fluid Cells:	N/A	2	3
Local Initial Mesh Refine Solid Cells	N/A	Off	On
Local Initial Mesh Refine Solid Cells	N/A	2	3
Local Initial Mesh Refine Partial Cells	N/A	On	On
Local Initial Mesh Level of Refining Partial Cells	N/A	2	3
Local Initial Mesh Advanced Narrow Channel Refinement	N/A	On	On
Local Initial Mesh Characteristic Number of Cells Across A Narrow Channel	N/A	15	15
Local Initial Mesh Narrow Channels Refinement Level	N/A	4	4
Local Initial Mesh the Minimum Height of Narrow Channels	N/A	Off	Off
Local Initial Mesh the Maximum Height of Narrow Channels	N/A	Off	Off

Table 32: Mesh Comparison, 1 mm Model

Mesh Setting	Course Mesh	Medium Mesh	Fine Mesh
Fluid Cells	71,453	122,540	152,319
Solid Cells	75,431	106,638	108,510
Partial Cells	33,195	47,800	48,675
Total Cells	**146,884**	**229,178**	**260,832**

Table 33: Mesh Comparison, 3 mm Model

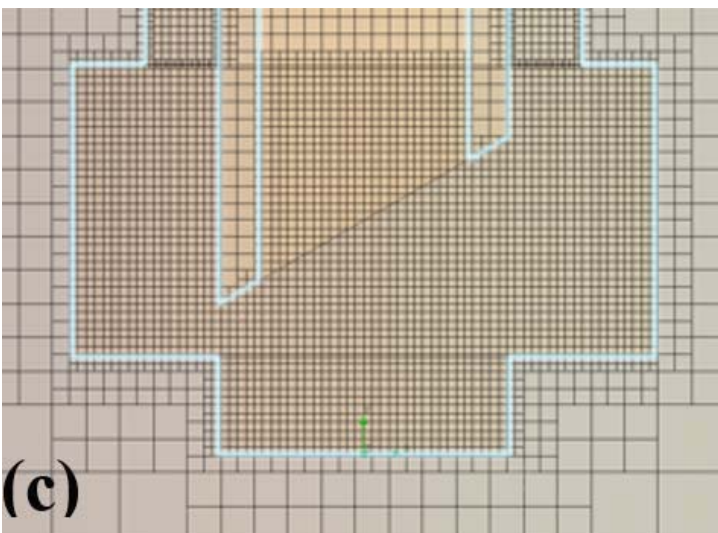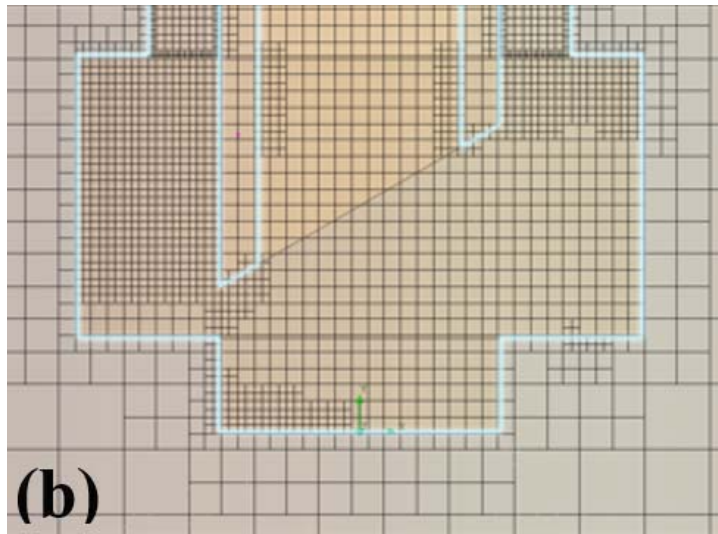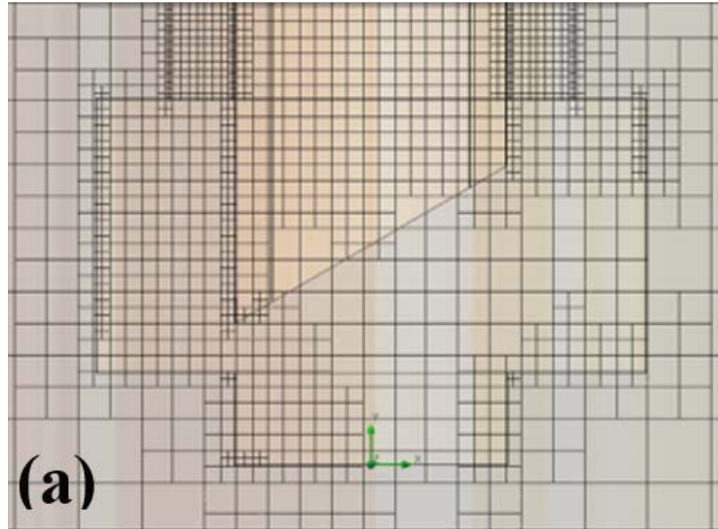| Mesh Setting	Course Mesh	Medium Mesh	Fine Mesh
Fluid Cells	63,929	105,774	153,540
Solid Cells	70,681	103,229	106,784
Partial Cells	30,540	45,799	47,203
Total Cells	**134,610**	**209,003**	**260,234**

Figure 72: Mesh Comparison, (a) Course, (b) Medium, and (c) Fine

From data analysis in Table 34 and Table 35, it was concluded that the time step of .25 s

and the course mesh proved to be an adequate model for convergence for the 1 mm

model. Table 36 and Table 37 verifies the 3 mm model also converges on the course

model at the .25 s time step. Therefore, the results presented are from the model with the

time step of .25 s and the course mesh unless otherwise specified.

Table 34: 1 mm Model Time Step Convergence (with Course Mesh)

Time Step (s)	Time to reach 350 K Maximum Water Temperature (s)	Percent Error with Respect to Maximum Temperature
dt = .25	1.75	Ref.
dt = .125	1.75	0.00%
dt = .0625	1.75	0.00%

Table 35: 1 mm Model Grid Convergence (with dt = .25s)

Mesh Refinement	Maximum Temperature of Solid (K)	Percent Error with Respect to Maximum Temperature
Course	672.536	Ref.
Medium	674.946	0.64%
Fine	674.311	0.47%

Table 36: 3 mm Model Time Step Convergence (with Course Mesh)

Time Step (s)	Maximum Temperature of Solid (K)	Percent Error with Respect to Maximum Temperature
dt = .25	1.75	Ref.
dt = .125	1.75	0.00%
dt = .0625	1.75	0.00%

Table 37: 3mm Model Grid Convergence (with dt = .25s)

Mesh Refinement	Time to reach 350 K Maximum Water Temperature (s)	Percent Error with Respect to Maximum Temperature
Course	673.325	Ref.
Medium	675.619	0.61%
Fine	674.611	0.34%

Table 38 displays the compared model data to the data obtained by Lai *et al*[33].

Table 38: Model Data to Lai *et al*[33] Data Comparison

Maximum Cooling Ratio	Project Models		Lai *et al* Models	
	1 mm	3 mm	1 mm	3 mm
Maximum Temperature of Solid (K)	672.536	673.325	702.000	706.800
Cooling ratio	2.242	2.244	2.340	2.356

The 1 mm cooling tube height model was better than the 3 mm cooling tube height model in both the present analysis and as seen in Lai *et al*[33]. However, the analysis model values varied from the Lai *et al*[33] values. This may be due to the possibility that this analysis assumed values not matching Lai *et al*[33] values. The weld cycle length and the time of the weld were not given in the Lai *et al*[33] model. From the analysis, the weld cycle time was 10 seconds, the weld time (heat generation) was one (1) second, and the electrode and the adapter reached a steady state temperature of 300 K before the next weld cycle began. Therefore, heat never built up in the electrode.

Another variation from the Lai *et al*[33] model was the use of parameterized material properties for both water and copper. Lai *et al*[33] used constant properties. Although the model material was more accurate with parameterized material properties, this added another variable to the analysis that could have possibly made the analysis' final values vary from the Lai *et al*[33] values.

Lai *et al*[33] could have run the simulation until it reached steady state and, at that time, calculated the cooling rate. The analysis model assumed that the cooling water was consistently entering the system at 300 K. Lai *et al*[33] could have assumed a closed loop water cooling system with a limited cooling rate. If the chiller could not keep up with the heat transfer rate, the water entering the system would gradually increase. This increase in electrode temperature was seen in the Lai *et al*[33] experiments.

The velocity profiles in the form of cut plots are similar in both the 1mm and 3mm models as shown in Figure 73 and Figure 74.
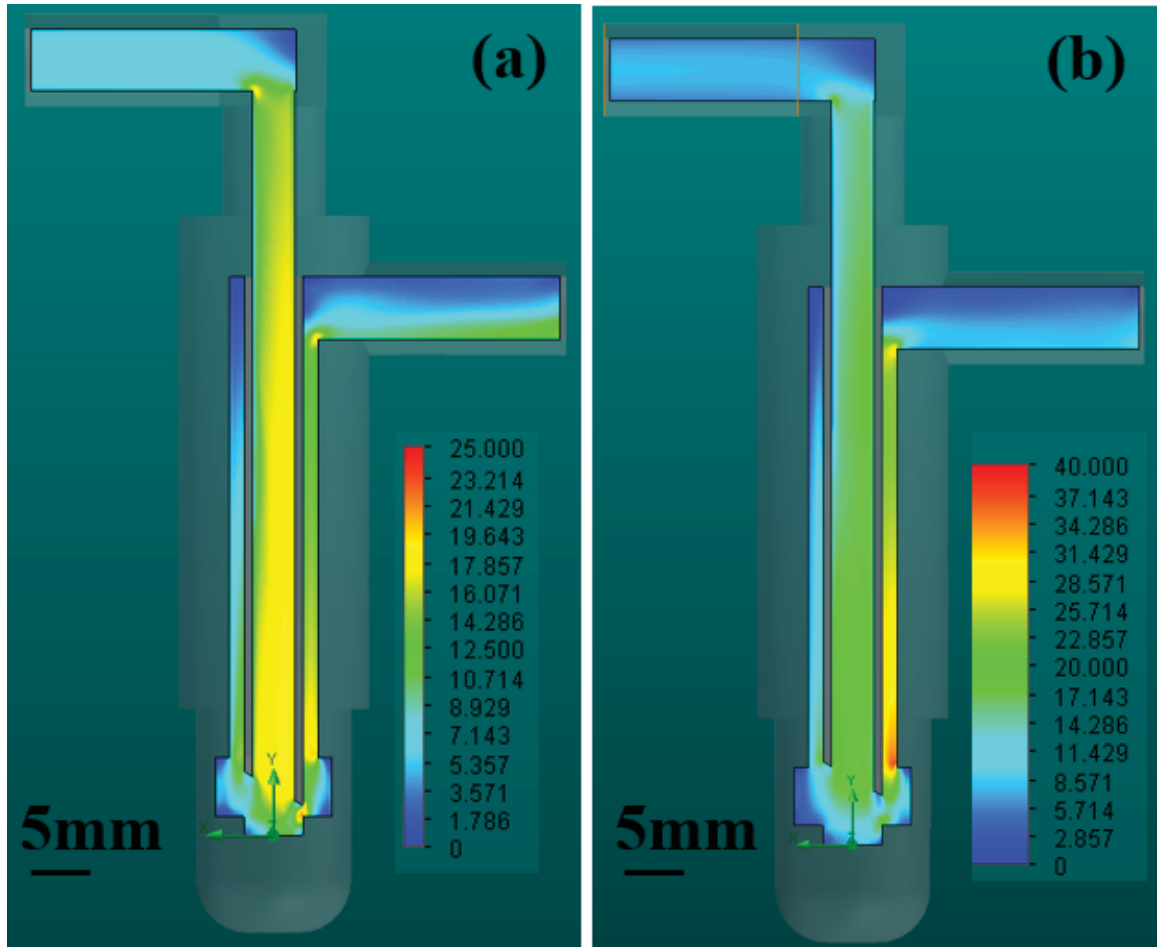

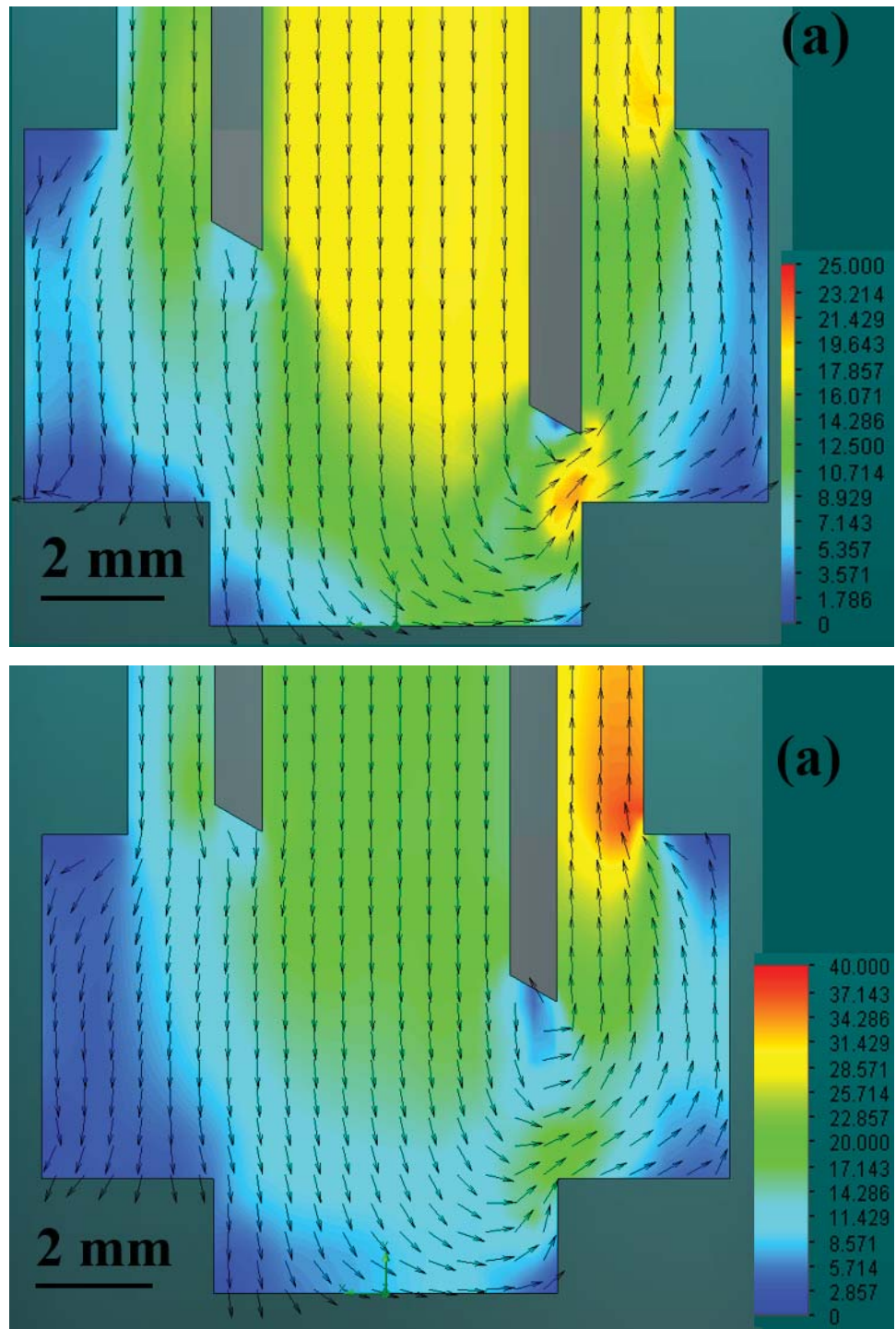Figure 73: Velocity Cut Plane at the Center of Model, (a) 1mm, and (b) 3mm

Figure 74: Velocity Cut Plane with Vectors, (a) 1 mm, and (b) 3 mm

The 1 mm model's maximum velocity occurred as the fluid flowed around the upper

portion of the internal cooling pipe. The 3 mm model's maximum velocity occurred at

the outlet of the internal cooling pipe. Figure 74 shows a local cut plot of the section of

interest that also shows the vector plot of the flow field. The arrow quantity, size, and spacing was determined by the user during the development of the cut plot. In this plot, it was noted that both models present a recirculating swirl below the higher portion of the internal cooling pipe. In both models, it was observed that water on the outside of the cooling pipe was flowing towards the bottom of the electrode instead of toward the electrode adapter outlet. This meant that as the water flowed upward, some of the water did not make it to the outlet and recirculated in the outer cooling path.

Figure 75 shows a more detailed velocity profile by applying nine cut plots in different planes of the 1mm model within one graphic. It can be noted that minimal velocity is seen in the outer cooling tube opposite the cooling water outlet.
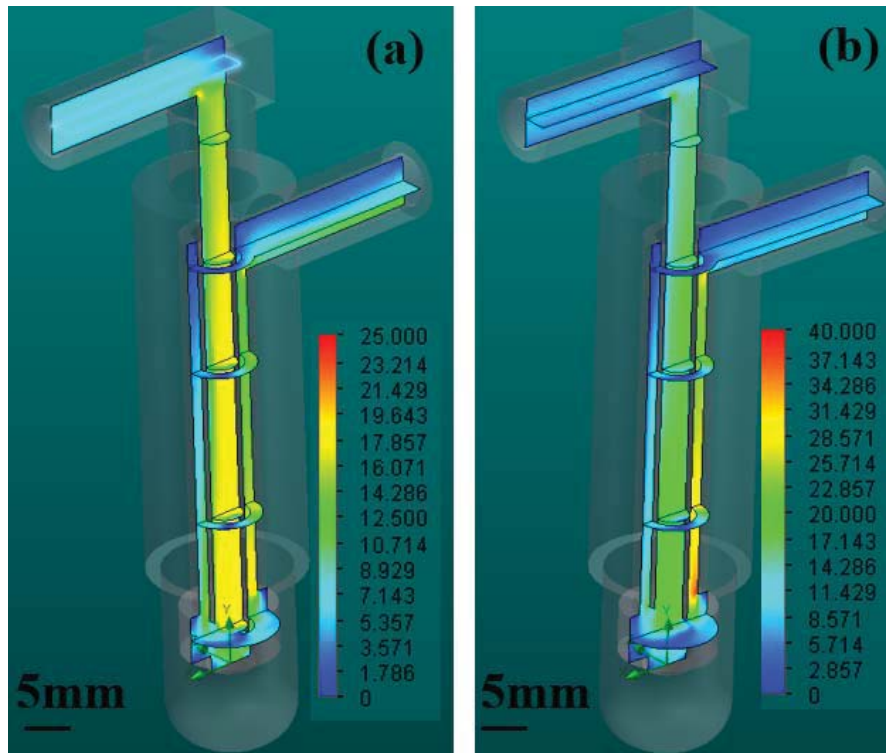

Figure 75: Velocity Cut Planes, (a) 1 mm, and (b) 3 mm

Figure 76 shows a flow trajectory result plot for the 1 mm model. The inlet of the model was selected as well as the quantity of flow paths to follow from that surface. The

velocity gradient was chosen to be shown on the flow trajectory paths. This is shown in the velocity vector field in Figure 74. Figure 76 shows the recirculation of the cooling water within the electrode adapter body.
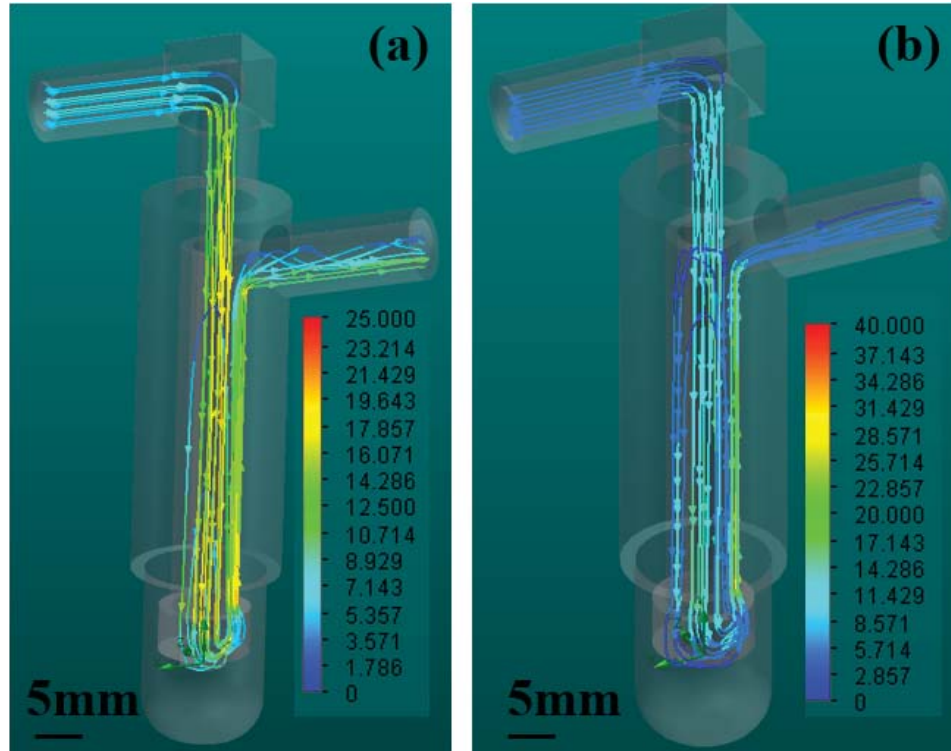

Figure 76: Velocity Flow Trajectories, (a) 1 mm, and (b) 3 mm

Figure 77 shows the maximum temperature of the cooling water and the electrode over the course of the first six (6) welds for the 1mm model. The maximum electrode temperature was 672.54 K and was reached at the end of the heat generated by the weld. The electrode then cooled down to the initial temperature of 300 K 7.50 s after the weld was completed. The water also followed a similar temperature pattern. The water reached a maximum temperature of 372.76 K at the end of the heat generated by the weld. The cooling water also went back to the initial temperature of 300 K in 7.50 s after the weld was completed. This cycle repeated itself every 10 s without change due to the model being able to reach its initial conditions before the next weld cycle commenced.

Figure 78 shows the temperature plot of the 3 mm model. The maximum fluid temperature is 373.77 K and the maximum solid temperature is 673.32 K.
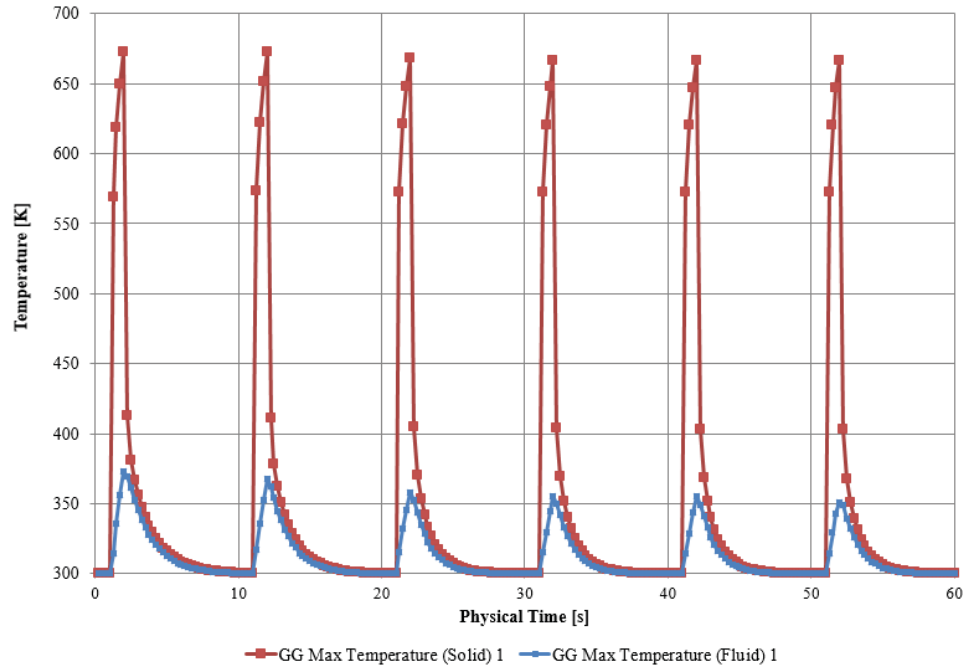

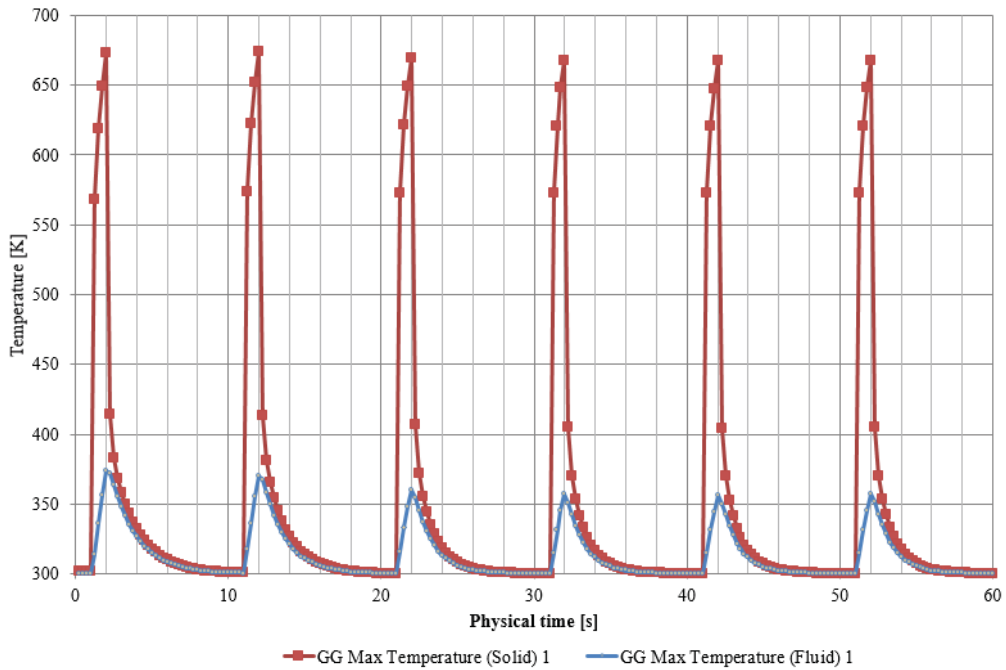Figure 77: Temperature vs Time (1 mm course grid, dt = .25 s)

Figure 78: Temperature vs Time (3 mm course grid, dt = .25 s)

Figure 79 illustrates how the temperature contours changed over time. At 1 s, the weld heat generation started for a duration of 1 s. At 2 s, the weld heat generation was completed and the electrode began to gradually cool.
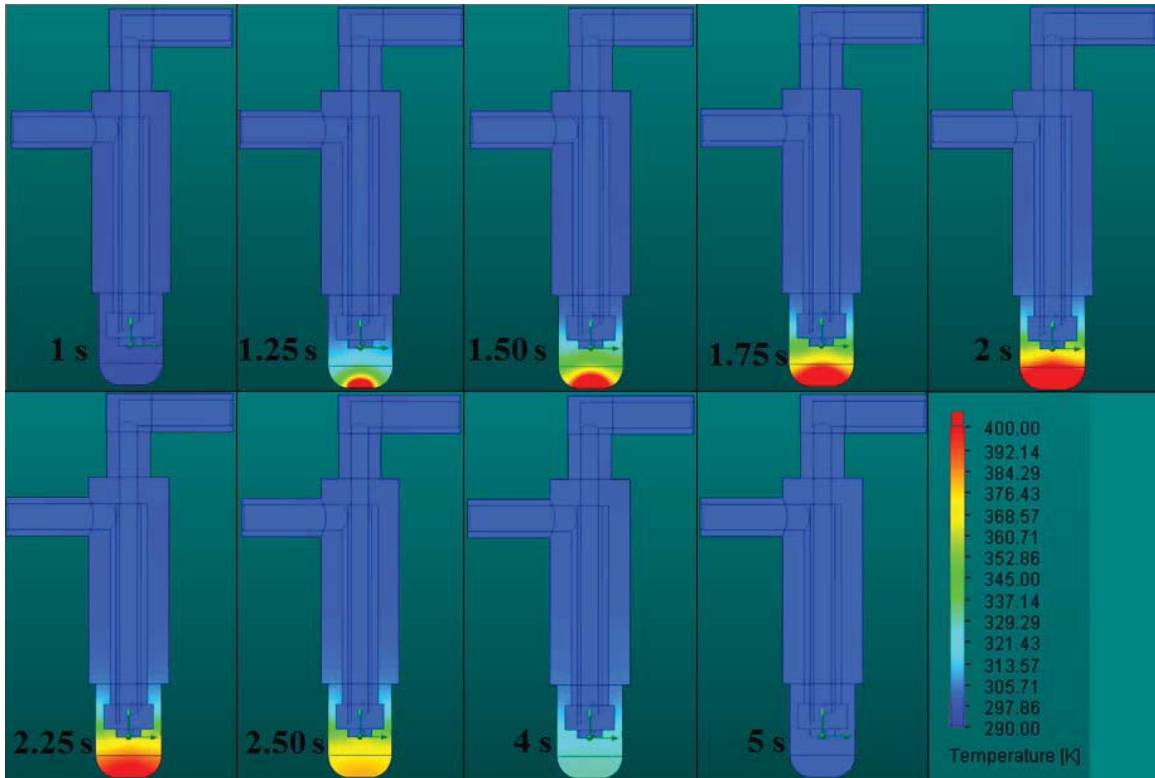
Figure 79: Temperature Cut Plot as it Changes Over Time (in seconds)

The observed heat transfer rate of the system is shown in Figure 80. The system considered the heat transfer from the solid to the water, then displayed it out of the system with a positive value. The negative downward spike represents the weld heat generation rate. Even though the heat generation rate was constant, the plot shows the change in heat transfer due to the cooling water transferring the energy away from the solid. When the simulation weld heat generation was complete, the graph switched to a positive number and slopes to zero. This displayed that as the model reached the steady state temperatures, that the heat transfer rate reached the value of zero. Although the heat

transfer rate reached the value of zero during each weld cycle, the maximum value varied through the transiently monitored time, shown in Figure 80 and Figure 81. This could possibly be the result of the time steps needing to be smaller for the heat transfer rate to converge properly.

The values for the 1 mm model for the cooling rate and the maximum temperature appear to be more optimized compared to the 3 mm model. However, this is not enough evidence to conclude that the 1 mm model is the "most" optimized model. Like a grid convergence test, more model geometries will need to be analyzed such as models that are smaller than the 1mm cooling pipe height and in between 1 mm and 3 mm to see if the smaller cooling rate of smaller maximum temperature values can be achieved through a different geometry.
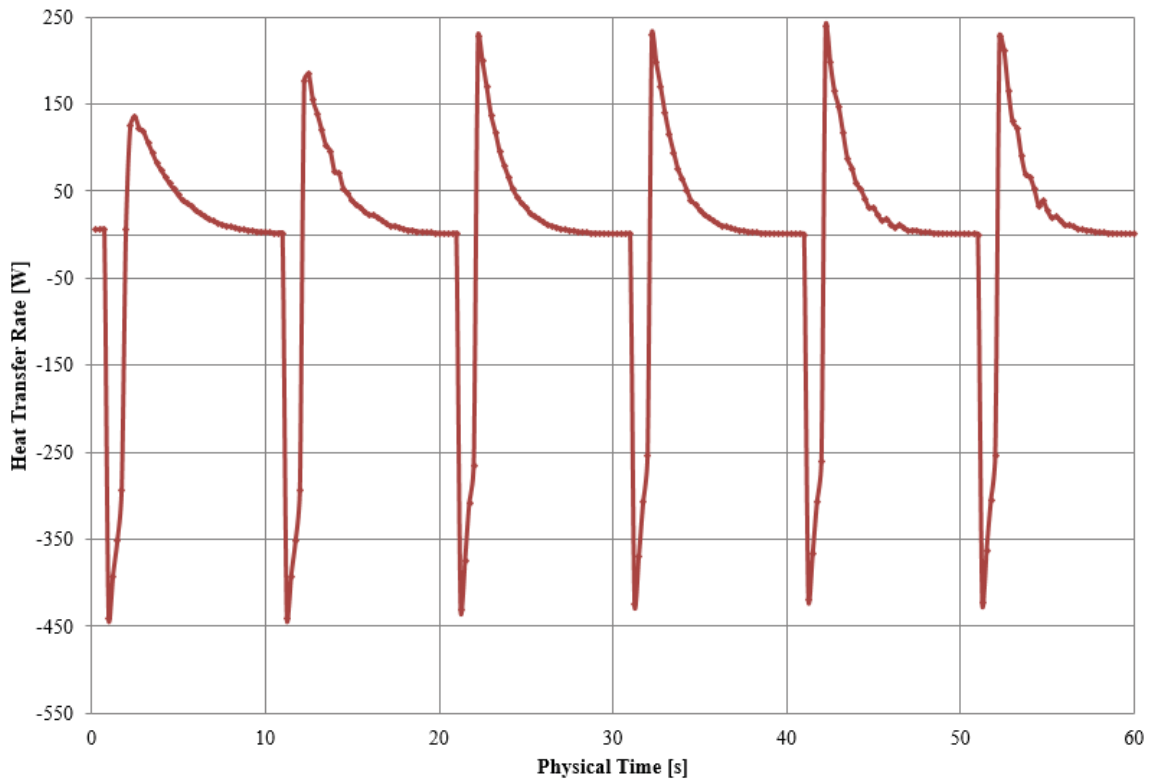
Figure 80: Heat Transfer Rate, (1 mm course grid, dt = .25 s)
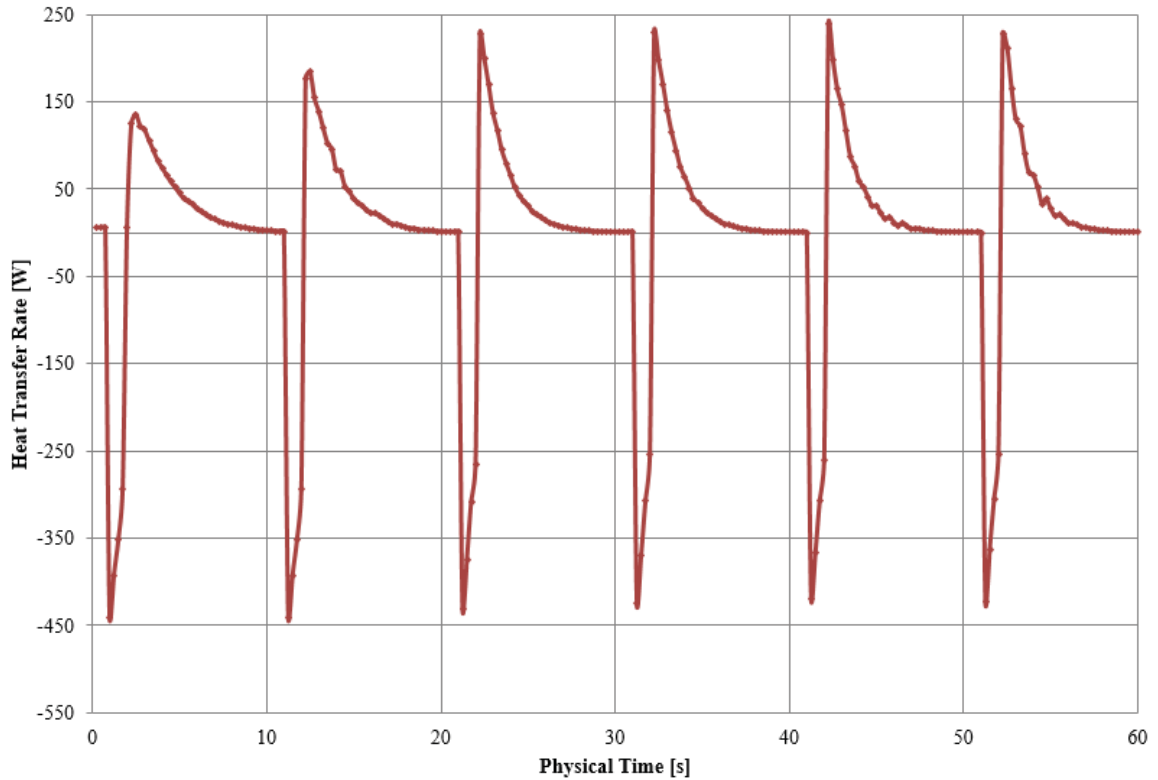
Figure 81: Heat Transfer Rate, (3 mm course grid, dt = .25 s)

Another point of contingency is that although the temperatures seem to converge in the simulation models, the heat transfer rates seemed to be close but not quite converged. To converge these values, models with smaller time steps should be performed and analyzed.

Adiabatic wall was selected because the analysis is only looking at the internal flow of the system. To expand the analysis further, an external flow may be utilized to examine the loss of heat from radiation and convection to the surrounding air.

4.0 Conclusions

Additive manufacturing copper parameters with a 200 W power laser were developed and utilized for this thesis and a numerical modeling of heat transfer process of an electrode/electrode adapter system was performed. The AM parts were found to be 66.5% density compared to bulk copper. When the AM parts were sintered, the density was increased to 68.9%. This implies increasing the laser power can increase the density of the AM parts. The strength and modulus of elasticity of the AM parts increased with sintering, as well. During this test, the AM parts that were created with optimized printing parameters were not viable for resistance welding due to the porosity and surface roughness. The porosity caused an increase in the power that was needed to perform the welds from the controlled systems that were tested. The resistance welds were inconsistent with the fully AM weld circuit (electrode adapter and electrode). A mixed weld circuit, with AM adapters and RWMA Class 2 electrodes, resulted in acceptable welds with only a 15% power increase.

More tests need to be completed with the varied secondary welding circuit. The welding that was achieved was done on a very small scale resistance welding machine with a minimal secondary circuit. Weld tests will need to be completed when increasing the length and number of AM parts.

By utilizing a stronger laser power, such as 1 kW, more dense parts with better surface quality could be created. This would lower the heat generated and resistance of the weld circuit. Water tests can be completed for the denser parts. If the denser AM parts are waterproof, printing water circuits within the electrodes and bus work can be accomplished. The efficiency of the flow and heat transferred will need to be analyzed.

Furthermore, the numerical analysis perform in this thesis can be verified through experimentation with a precise printing AM model.

The search for RWMA Class 2 powder will continue with the hope of obtaining this copper alloy powder within the next set of experiments. By using this powder, the printed electrodes will be stronger and should be able to resist deformation for longer periods of time.

The flow analysis completed on the electrode cooling optimization can be expanded. Changing the geometry of the back of the electrode and inlet tube and the effect on flow and heat transfer can also be investigated further. An external flow analysis can be completed to examine the heat loss to the surrounding air and workpieces.

5.0 References

[1] Alexandros Beiker Kair and Konstantinos Sofos, "Additive Manufacturing and Production of Metallic Parts in Automotive Industry: A Case Study on Technical, Economic and Environmental Sustainability Aspects," 2014, http://www.diva-portal.org/smash/record.jsf?pid=diva2:740682.

[2] "CE55020-VOLTZA-WELD-GUN-12.gif (GIF Image, 484 × 290 Pixels)," accessed December 17, 2016, http://www2.cntrline.com/images/CE50000/CE55000/CE55020-VOLTZA-WELD-GUN-12.gif.

[3] Resistance Welder Manufacturers' Association, *Resistance Welding Manual, Revised 4th Edition*, 4th edition (Philadelphia, Pa.: Resistance Welder Manufactures Assn, 2003).

[4] D D Gu et al., "Laser Additive Manufacturing of Metallic Components: Materials, Processes and Mechanisms," *International Materials Reviews* 57, no. 3 (May 2012): 133–64, doi:10.1179/1743280411Y.0000000014.

[5] Jialin Yang et al., "Top Surface Quality Research for Direct Metal Laser Fabrication," *Rapid Prototyping Journal* 18, no. 1 (2012): 4–15.

[6] Suman Das, "Physical Aspects of Process Control in Selective Laser Sintering of Metals," *Advanced Engineering Materials* 5, no. 10 (October 2003): 701–11.

[7] H.H. Zhu, L. Lu, and J.Y.H. Fuh, "Development and Characterisation of Direct Laser Sintering Cu-Based Metal Powder," *Journal of Materials Processing Technology* 140, no. 1–3 (September 2003): 314–17, doi:10.1016/S0924-0136(03)00755-6.

[8] "Characteristics and Properties of Copper and Copper Alloy P/M Materials," *Copper Development Association Inc. : Industrial: Powder Metallurgy - Characteristics and Properties*, accessed December 17, 2016, https://www.copper.org/resources/properties/129_6/characteristics_properties.html.

[9] H. H. Zhu, J. Y. H. Fuh, and L. Lu, "Microstructural Evolution in Direct Laser Sintering of Cu-Based Metal Powder," *Rapid Prototyping Journal* 11, no. 2 (2005): 74–81.

[10] Y. Tang et al., "Direct Laser Sintering of a Copper-Based Alloy for Creating Three-Dimensional Metal Parts," *Journal of Materials Processing Technology* 140, no. 1–3 (September 2003): 368–72, doi:10.1016/S0924-0136(03)00766-0.

[11] Yang et al., "Top Surface Quality Research for Direct Metal Laser Fabrication."

[12] David Becker and Konrad Wissenbach, "Components Made from Copper Powder Open up New Opportunities," accessed December 17, 2016, https://www.academics.com/science/components_made_from_copper_powder_open_up_new_opportunities_45010.html.

[13] D. Q. Zhang, Z. H. Liu, and C. K. Chua, *Investigation on Forming Process of Copper Alloys via Selective Laser Melting*, 2013, https://www.researchgate.net/publication/284910430_Investigation_on_forming_process_of_copper_alloys_via_Selective_Laser_Melting.

[14] P.A. Lykov, E.V. Safonov, and A.M. Akhmedianov, "Selective Laser Melting of Copper," *Materials Science Forum* 843 (February 2016): 284–88, doi:10.4028/www.scientific.net/MSF.843.284.

[15] "Asm Specialty Handbook: Copper and Copper Alloys (ASM Specialty Handbook) (ASM Specialty Handbook): J. R. Davis: 0000871707268: Amazon.com: Books," accessed December 17, 2016, https://www.amazon.com/Asm-Specialty-Handbook-Copper-Alloys/dp/0871707268/ref=sr_1_1?s=books&ie=UTF8&qid=1482010099&sr=1-1&keywords=9780871707260.

[16] Randall M. German, *Powder Metallurgy Science*, 2 Sub edition (Princeton, N.J: Metal Powder Industry, 1994).

[17] "Production and Properties of Copper and Copper Alloy Powders," *Copper Development Association Inc. : Industrial: Powder Metallurgy - Production and Properties*, accessed December 17, 2016, https://www.copper.org/resources/properties/129_6/production.html.

[18] "Copper and Copper Alloys," *Ecka Granules Metal Powder Technology*, accessed December 17, 2016, https://www.ecka-granules.com/products/copper-and-copper-alloys/.

[19] G. S. Upadhyaya, *Powder Metallurgy Technology* (Cambridge: Cambridge International Science Publishing, 1997).

[20] "Ultrafine Electrolytic Copper Powder for EMI Shielding with High Conductivity Silver Coating," *Powder Metallurgy Review*, December 10, 2013, http://www.pm-review.com/ultrafine-electrolytic-copper-powder-for-emi-shielding-with-high-conductivity-silver-coating/.

[21] "Data Sheet: Class II Chrome Copper (RWMA C18200)," SCS Catalog, *Southern Copper & Supply Company*, accessed December 17, 2016, http://www.southerncopper.com/customers/southerncopper/assets/documents/metals/scscat182cl2.pdf.

[22] "Copper- Spherical Copper Shot," *AcuPowder International, LLC.*, February 17, 2012, http://acupowder.com/library/library/documents/copperspherical-copper-shot-02-27-12.pdf.

[23] "Copper Ultra High Purity& Ultra Fine," *AcuPowder International, LLC.*, February 27, 2012, http://acupowder.com/library/library/documents/copper-ultra-high-purityultra-fine02-27-12.pdf.

[24] "Renishaw Additive Manufacturing System AM250 200W, 400W and Extended Z Axis: User Guide" (Renishaw Engineering Company, April 2011).

[25] "Standard Test Methods for Tension Testing of Metallic Materials," *ASTM International* E8/E8M-08 (n.d.): 14.

[26] Suhas V. Patankar, *Numerical Heat Transfer and Fluid Flow*, 1st ed. (McGraw-Hill Book Company, n.d.).

[27] Arthur J. McEvily and Jirapong Kasivitamnuay, *Metal Failures: Mechanisms, Analysis, Prevention*, 2 edition (Hoboken, New Jersey: Wiley-Interscience, 2013).

[28] David Bourell et al., "Powder Densification Maps in Selective Laser Sintering," *Advanced Engineering Materials* 4, no. 9 (September 2002): 663–69.

[29] "Copper, Cu; Annealed," accessed April 18, 2017, http://www.matweb.com/search/DataSheet.aspx?MatGUID=9aebe83845c04c1db5126fada6f76f7e&ckck=1.

[30] "WeldHelp | Issue: Stuck Weld | G.E. Schmidt," *G.E. Schmidt Inc.*, accessed March 22, 2017, http://www.geschmidt.com/weldhelp-issue-stuck-weld/.

[31] "FIGURE R-8.png (PNG Image, 830 × 407 Pixels)," *WeldCor: Encyclopedia of Terms*, accessed March 22, 2017, http://www.weldcor.ca/public/ckfinder/userfiles/files/FIGURE%20R-8.png.

[32] Roger B. Hirsch and Ronald Leibovitz, "Influence of Water Temp and Flow on Electrode Life," *Unitrol Electronics, Inc.*, accessed February 25, 2016, <http://www.unitrol-electronics.com/assets/docs/tech-papers/electrode.pdf>.

[33] X. M. Lai et al., "Optimal Design of Electrode Cooling System for Resistance Spot Welding with the Response Surface Method," *The International Journal of Advanced Manufacturing Technology* 41, no. 3–4 (March 2009): 226–33, doi:10.1007/s00170-008-1478-5.